

# Development and Application of Mixed Quantum-Classical Non-adiabatic Molecular Dynamics Techniques for Charge Transport in Organic Semiconductors

Matt Ellis

A dissertation submitted in partial fulfillment  
of the requirements for the degree of  
Doctor of Philosophy  
of  
University College London.

Department of Physics and Astronomy  
University College London

September 8, 2021

I, Matt Ellis, confirm that the work presented in this thesis is my own. Where information has been derived from other sources, I confirm that this has been indicated in the work.

# Abstract

This work will be split into two parts. The first will be concerned with the implementation of a novel nonadiabatic molecular dynamics technique, derived as the semi-classical limit of exact factorisation, named Coupled-Trajectory Mixed Quantum-Classical Molecular Dynamics (CTMQC). I will investigate its current formulation within the literature, highlight some current pitfalls —and suggest ways to alleviate them— and present results of my implementation. I will also give results of the integration of this technique within the fragment-orbital based framework (FOB). This is designed to allow the fast calculation of electronic couplings through formulating the equations in a diabatic basis. Initially, the CTMQC algorithm will be applied to the 1D Tully toy models and later to an Ethylene dimer. We will see that, although the Tully model results are very promising, instabilities in the calculation of key quantities makes the current algorithm unusable for molecular systems.

The second part will be concerned with a well-tested, semi-classical technique, based on Tully’s fewest switches surface hopping (FOB-SH). I will apply this to nanoscale systems of pentacene; will investigate the effect a variable quench time in a melt-quench scheme has on the crystallinity of these pentacene systems; and discuss how the resulting nanostructure affects charge transport dynamics. Finally, I will also discuss my implementation of two methods to calculate electrostatic interactions within FOB-SH. I will show how an addition-subtraction scheme and the damped shifted forces method (an approximation to full Ewald) can be used to optimise the calculations and test these methods against full Ewald electrostatics.

# Impact Statement

Many processes critical to life and essential technologies such as photosynthesis, vision and charge transport, are nonadiabatic. That is, a system in which electronic states can change energy level nonradiatively. However, these processes often occur at very short timescales (fs-ns) and/or at very small lengthscales (nm- $\mu$ m). Therefore, they have until quite recently, been difficult to study experimentally. To compound matters, the systems of interest are often quantum mechanical in nature, making large systems (beyond nm or ns) expensive to study computationally/theoretically. This often makes comparison of computational results to experiment difficult and it is only with carefully chosen approximations to accepted theory (such as Schrödinger's equation) that these systems can be modelled. Perhaps the most crucial approximation is the semi-classical approximation, i.e. treating as much of the system with classical mechanics as is reasonable. This is often achieved by treating the nuclear degrees of freedom as classical point particles and the electronic degrees of freedom quantum mechanically. In this work, I will investigate two techniques that make use of this approximation: a popular nonadiabatic molecular dynamics technique, Tully's fewest switches surface hopping (FSSH); and a lesser known newcomer to the field, coupled-trajectory mixed quantum-classical molecular dynamics (CTMQC).

This work is, to my knowledge, the first to present the pitfalls of the CTMQC technique, and partially address them. I will show tests of my implementation, verifying that it works, before presenting the cause of the problems. This is important as CTMQC shows some extremely promising results with simple model systems, especially when it comes to the correct account of quantum coherence -a shortcoming that has troubled users of

the more conventional FSSH. I will also present an implementation of CTMQC within the extremely efficient fragment orbital based framework. This framework has been used previously with surface hopping to simulate systems of thousands of molecules -helping to bridge the gap between experimentally accessible length/timescales and computationally accessible ones. This is vital to computational models, which should be validated against experiment.

In addition to aiding in the development of theory, this work will apply a technique named fragment orbital based surface hopping (FOB-SH) to model charge transport in systems of varying levels of amorphicity/crystallinity. It is in practise extremely difficult to produce highly pure, organic, single crystals that lack defects. This is especially true in the mass production of consumer electronics. For this reason, it is important to be able to model systems with high levels of disorder, to help guide experiment and the production of new (organic semiconductor) technologies. This work shows that the FOB-SH method can be accurately applied to these systems and retrieve experimentally comparable results spanning several orders of magnitude.

Finally, a vital property in the simulation of many materials -electrostatic interactions- is investigated. In particular, the implementation of electrostatic calculations within FOB-SH. Currently, these are inefficiently implemented making it infeasible to apply them to systems larger than tens of molecules. I will present two implementations of electrostatics within FOB-SH that will allow the simulation of systems of hundreds to thousands of organic molecules. This will pave the way for new classes of materials to be studied nonadiabatically with FOB-SH.

# Acknowledgements

I'd like to start by thanking all the members of the Blumberger group for their support, I know without them I wouldn't have completed the PhD. I would especially like to thank Prof Antoine Carof for holding my hand through the first several months, and Dr Samuele Giannini for the rest! Chris Ahart, Dr Xiuyun Jiang, Dr Orestis Ziogos, Dr Xiaojing Wu, Jan Elsner, Prof Soumya Ghosh, Dr Patrick Gutlein, Dr Hui Yang, Dr Lijljana Stojanovic, Dr Roohollah Hafizi, Dr Wei-Tao Peng, Daniel Holub and Prof Zdenek Futera also all deserve a special mention. I, of course, would especially like to thank my supervisor Jochen Blumberger for all his guidance and many useful discussions throughout my PhD.

I would also like to thank all the friends and family who have supported me. Though, special thanks should go to: my parents, grandparents and brother; my partner's family —especially for tolerating living with me for several months during lockdown!; Victor and Rhiannon.

Most of all, I would like to acknowledge my partner Liam for all his help and support throughout the PhD, and I would like to dedicate this thesis to him.

# Contents

1	Introduction	22
1.1	Charge Transport in Organic Semiconductors	22
1.1.1	Organic Semiconductors	22
1.2	Semi-classical Nonadiabatic Molecular Dynamics	23
1.2.1	Ehrenfest Dynamics	24
1.2.2	Surface hopping	27
1.2.3	FOB-SH	30
1.3	Exact Factorisation and its Semi-Classical Limit	32
1.4	Approximations leading to CTMQC	35
1.4.1	Classical Nuclei	35
1.4.2	Neglect the ENCO in the TDPES	35
1.4.3	Derivative of the Adiabatic Coefficients	35
1.4.4	Gaussian Nuclear Wavepackets	36
1.4.5	Separating the Effects of Decoherence and NACVs	36
1.5	The CTMQC equations	37
1.5.1	Adiabatic Basis	37
1.5.2	Calculating the Quantum Momentum	38
2	CTMQC applied to the Tully Models	41
2.1	Testing the Ehrenfest Implementation	43
2.1.1	Norm Conservation	44
2.1.2	Energy Conservation	44
2.1.3	Comparisons To Literature	46

	Contents	8
2.2	Testing the CTMQC implementation . . . . .	51
2.2.1	Conservation of the norm . . . . .	51
2.2.2	Mathematical Tests . . . . .	55
2.2.3	Energy Conservation . . . . .	57
2.2.4	Comparisons to literature . . . . .	57
2.3	Construction of the quantum momentum . . . . .	61
2.3.1	Constant Values of $\sigma$ . . . . .	61
2.3.2	Dynamic $\sigma_v^{(I)}(t)$ calculation . . . . .	63
2.4	Conclusion . . . . .	64
3	CTMQC applied to molecular systems	66
3.1	Basis Transformation . . . . .	67
3.1.1	Coefficients . . . . .	68
3.1.2	Forces . . . . .	70
3.2	Testing the diabatic propagator . . . . .	70
3.3	Simulating Molecular Systems . . . . .	71
3.4	Conclusions . . . . .	74
4	Charge transfer in amorphous systems	77
4.1	Creating Amorphous Pentacene . . . . .	79
4.2	Structure of the quenched simulations . . . . .	80
4.2.1	Final Structure Snapshots . . . . .	80
4.2.2	Molecular Packing . . . . .	81
4.2.3	Mass Density . . . . .	83
4.2.4	Angular Distribution . . . . .	84
4.2.5	Radial Distribution Function . . . . .	85
4.2.6	Crystallinity . . . . .	86
4.3	Charge Transfer Properties . . . . .	88
4.3.1	Global Couplings . . . . .	88
4.3.2	Coupling Networks . . . . .	89
4.4	Surface Hopping Methodology . . . . .	92

	Contents	9
4.4.1	Surface Hopping Setup . . . . .	93
4.4.2	Inverse Participation Ratio . . . . .	94
4.4.3	Hole Mobilities . . . . .	97
4.4.4	Surface Hopping Results . . . . .	98
4.5	Conclusions . . . . .	100
5	Extending surface hopping	102
5.1	Implementation details: addition subtraction method . . . . .	103
5.1.1	Ewald Equations and the additional subtraction scheme . . . . .	106
5.1.2	Self-energy addition subtraction scheme . . . . .	107
5.1.3	Real space addition subtraction . . . . .	108
5.1.4	Bonded corrections addition subtraction . . . . .	109
5.1.5	Reciprocal space addition subtraction . . . . .	109
5.2	Timing the electrostatics implementation . . . . .	111
5.2.1	Testing the electrostatics implementation . . . . .	112
5.2.2	DSF . . . . .	113
5.3	Testing DSF . . . . .	114
5.3.1	Classical MD . . . . .	114
5.3.2	Surface Hopping . . . . .	116
5.4	Timing DSF . . . . .	119
5.5	Conclusions . . . . .	120
6	General Conclusions and Outlook	122
Appendices		125
A	Tully Model Paramters	125
A.1	Model 1 -Single Avoided Crossing . . . . .	125
A.2	Model 2 -Dual Avoided Crossing . . . . .	126
A.3	Model 3 -Extended Coupling . . . . .	126
A.4	Model 4 -Dual Arch . . . . .	127
B	Wigner Distribution Derivation	128

Contents	10
C $\mathbf{R}_{lk,v}$ Alternatives	130
C.1 $\mathbf{R}_{lk,v}$ Extrapolation . . . . .	130
C.2 Alternative Quantum Momentum Intercept . . . . .	130
D Rabi Oscillation	132
E Norm Conservation in CTMQC and Ehrenfest	134
F Dynamic $\sigma$ Calculation	136
G Basis Transformation	137
G.1 Forces . . . . .	138
H Adiabatic State Initialisation	140
I Center of Mass Restraints	142
J Active Systems	143
J.1 0ns and 1ns Systems . . . . .	143
J.2 100ns System . . . . .	144
J.3 10ns System . . . . .	145
K Additional Pentacene Mobility Information	147
L Addition-Subtraction Forces	148
L.1 Real Space . . . . .	148
M Colophon	149
Bibliography	150

# List of Figures

1.1	An example of a typical Ehrenfest simulation near an avoided crossing. The black line represents the adiabatic potential energy surface due to the effective potential energy surface, which is a population-weighted average of the ground and excited state (red and blue lines respectively). The black dashed line shows an example of a path taken by an atom travelling in this system. . . . .	25
1.2	An example of a typical surface hopping simulation near an avoided crossing. The black line represents the effective potential energy surface the nuclei (black dot) travel on. This is a discontinuous combination of ground (red line) and excited (blue line) states. The current PES the nuclei are travelling on is denoted the ‘active’ state. . . . .	27
1.3	A demonstration of how the TDPES can cause the splitting of the nuclear wavepacket in non-adiabatic regions. The red line represents the TDPES and the blue is the nuclear density. Figure adapted from Agostini, 15 <sup>1</sup> . . .	34
2.1	Adiabatic potential energy surfaces (orange and blue) and element 1, 2 of the nonadiabatic coupling vector (black) for the four model systems. For parameters see appendix A. . . . .	42
2.2	The norm conservation averaged over all replicas for Ehrenfest simulations with various electronic timesteps for each Tully model using a initial high momenta. . . . .	44
2.3	Energy conservation values for various nuclear timesteps for the high momentum case of each Tully model using Ehrenfest dynamics. . . . .	45

2.4	A comparison of my implementation of Ehrenfest (for 4 model Hamiltonians) and results from the literature for the low momenta cases. The black dashed lines show my data (ground state adiabatic populations), the orange dashed lines are data from Agostini <sup>2</sup> and the blue solid lines are from Gossel <sup>3</sup> . The figures are labelled with their model number, whether the initial momentum was high or low and whether the populations or coherence indicator was plotted. . . . .	47
2.5	A comparison of my implementation of Ehrenfest (for 4 model Hamiltonians) and results from the literature for the high momenta cases. The black dashed lines show my data (ground state adiabatic populations), the orange dashed lines are data from Agostini <sup>2</sup> and the blue solid lines are from Gossel <sup>3</sup> . The figures are labelled with their model number, whether the initial momentum was high or low and whether the populations or coherence indicator was plotted. . . . .	48
2.6	Comparison of transmission probabilities through the region of high nonadiabatic coupling on the ground state. Tully model one is shown in the top-left, Tully model two is shown in the top-right and Tully model three is shown in the bottom-left. . . . .	50
2.7	The norm conservation when using standard CTMQC as outlined in the literature for each of the Tully models. These simulations were ran with a high initial momentum. The red markers show data points and vertical bars show error bars associated with each point. . . . .	52
2.8	As the denominator of the $\mathbf{R}_{lk,v}$ term approaches zero (bottom panel) the full $\mathbf{R}_{lk,v}$ term (2 <sup>nd</sup> to bottom panel) can approach infinity which propagates through the $\mathcal{Q}_{lk,v}^{(I)}$ term (2 <sup>nd</sup> to top panel) causing discontinuities and norm drift in the populations (top panel). The grey vertical bar denotes the region the denominator approaches 0. The thin solid red lines in the top panel show the norm drift for individual replicas. . . . .	53

2.9 Norm conservation in CTMQC after applying a divergence correction to the $\mathbf{R}_{lk,v}$ term. RI0 refers to method 3, Extrap DC refers to method two and Ehren DC refers to method 1. No DC Corr shows the population norm without any corrections applied. . . . .	54
2.10 The conserved quantity given in equation (2.6) (y-axis). Each color represents data outputted by a simulation using a different model (specified in the legend). Each time-series is plotted with a translucent color meaning each model's data can be seen at once. . . . .	56
2.11 Energy drift in the 4 Tully models using the full CTMQC equations. Error bars are from multiple simulations carried out with different random sampling of the initial positions and momenta. . . . .	58
2.12 A comparison of my implementation of full CTMQC (for 4 model Hamiltonians) and results from the literature for the low momentum cases. The black dashed lines show my CTMQC data (ground state adiabatic populations), the orange dashed lines are data from Agostini <sup>2</sup> and the blue solid lines are from Gossel <sup>3</sup> . The solid green line shows data from exact quantum mechanical simulations given in Gossel. The figures are labelled with their model number, whether the initial momentum was high or low and whether the populations or coherence indicator was plotted. . . . .	59
2.13 A comparison of my implementation of full CTMQC (for 4 model Hamiltonians) and results from the literature for the high momentum cases. The black dashed lines show my CTMQC data (ground state adiabatic populations), the orange dashed lines are data from Agostini <sup>2</sup> and the blue solid lines are from Gossel <sup>3</sup> . The solid green line shows data from exact quantum mechanical simulations given in Gossel. The figures are labelled with their model number, whether the initial momentum was high or low and whether the populations or coherence indicator was plotted. . . . .	60

2.14	4 high momenta cases of the Tully models with a various constant $\sigma$ values used in the calculation of the quantum momentum. Thin solid lines show results from my simulations. The thick, green, dashed line shows data from exact quantum dynamics simulations taken from Gossel <sup>3</sup> which should be taken as a reference. . . . .	62
2.15	Four high momentum cases of the Tully models with a dynamic calculation of sigma using various values for const. . . . .	63
3.1	The four Tully models simulated using propagating the equations within a diabatic and adiabatic basis. The green line shows results from the diabatic propagator and the red line shows results from the adiabatic propagator. Model three shows an exact agreement between the adiabatic and diabatic propagators hence only one line is seen. . . . .	71
3.2	An example Ethylene dimer used to test the CTMQC implementation. The right panel shows the positions of just one replica. The left panel shows the positions of all replicas with the replica shown on the right highlighted in red. . . . .	72
3.3	The norm of the adiabatic expansion coefficients. Thin red lines show the norm for each trajectory and the thick green line shows the average over all trajectories. . . . .	73
4.1	An example of the herringbone packing typically found in Pentacene crystals	78
4.2	The melt-quench scheme used to create amorphous pentacene systems. Blue boxes indicate steps using an NPT ensemble, orange boxes indicate use of a NVT ensemble. . . . .	79
4.3	The final snapshot of each quenching simulation visualised in VMD <sup>4</sup> and rendered with Tachyon <sup>5</sup> . Snapshots are ordered by quenching time i.e. a) is the 0ns quench, b) is the 1ns quench and so on. . . . .	81

4.4	The 100ns quenched structure with different clusters shown with different colours. A bird's eye view of the green cluster has been shown on the left to demonstrate the herringbone packing within each cluster/layer. The far-right image labelled 'Crystal' is a snapshot of a crystal plane after a short MD equilibration. . . . .	82
4.5	A slice from the 0ns quenched structure with two selected clusters displaying herringbone-like packing. . . . .	82
4.6	A time series of the density of the quenched structures. The black line shows the experimental mass density of crystal pentacene. . . . .	83
4.7	The angular distribution for the four different quench times is shown above. The brown and purple lines are from a perfect crystal before and after a short MD run. The others are after the various melt-quench simulations. On the right is a schematic showing which angles are referenced in each plot.	84
4.8	The carbon-carbon radial distribution function for four different quenching times and a crystal before and after 50ps of MD. The quenches (0, 1, 10 and 100ns) are shown in blue, orange, green and red respectively. The crystal data are shown in purple and brown. . . . .	85
4.9	The quench time vs crystallinity given by equation 4.1. Black circles show raw data and the dashed black line is a line of best fit using the equation $C = m \log_{10}(t) + C_0$ . . . . .	87
4.10	The global coupling distribution for each of the quenched structures (in blue, orange, green and red) and one structure after a 10ns quench without using electrostatics (purple line). The black dashed lines represent the maximum coupling within a perfect pentacene crystal. . . . .	88



- 4.12 Mechanism of hole transport in bulk pentacene phases. The transport scenario for amorphous, nanocrystalline and single-crystalline pentacene are shown in the bottom, middle and top row, respectively. Pentacene molecules are shown in grey stick representation and the crystallinity of the phases is indicated on the scale to the right. Isosurfaces of the charge carrier wavefunction,  $\Psi(t)$  (Eq. 1.6), are depicted in red and blue colors for three different times along a FOB-SH trajectory as indicated. The red and blue colours depict positive and negative phases of the wavefunction. The initial positions and extensions of the hole polaron are shown in the snapshots to the left (circles in pink), the transitions to the new positions are shown in the snapshots in the middle, and the hole polaron in the new position is shown in the snapshots to the right (circles in blue). Notice the different extent of hole carrier delocalisation for the different phases. . . . . 95
- 4.13 Hole mobilities and inverse participation ratio (IPR) for the pentacene phases studied. In (A), computed hole mobilities and IPR from FOB-SH simulation are shown for bulk pentacene phases as a function of the crystallinity of the sample (blue and green circles, respectively). The local mobilities and IPR for different regions of the sample are shown in small circles and the averages are shown in large circles. In (B), computed mobilities for bulk pentacene phases and 2D pentacene layers (hollow circles) are compared to experimental results (filled circles). The bulk pentacene phases were classified as ‘amorphous’, ‘polycrystalline’ and single-crystalline. The mean value for each category is given by a horizontal line. Error bars for computed values indicate the spread in local mobility. 1,2: ref. <sup>7</sup>, 3: ref. <sup>8</sup>, 4,5: ref. <sup>9</sup>, 6: this work,  $Cr = 0\%$ , 7,8: ref. <sup>10</sup>, 9,10,11: ref. <sup>11</sup>, 12: ref. <sup>12</sup>, 13,14,15: ref. <sup>13</sup>, 16: this work,  $Cr = 30\%$ , 17: this work,  $Cr = 60\%$ , 18: this work,  $Cr = 80\%$ , 19: ref. <sup>14</sup>, 20: this work, 2D pentacene, 1L, 21: ref. <sup>14</sup>, 22: this work, 2D pentacene, 2L, 23,24: ref. <sup>15</sup>, 25: ref. <sup>16</sup>, 26: ref. <sup>17</sup>, 27: this work,  $Cr = 100\%$ . Additional information on the device measurements and gate dielectrics used can be found in appendix K, Table K.1. . . . . 98

5.1	A demonstration of the procedure to calculate diagonal elements of the Hamiltonian (site-energies). Red (blue) shapes represent a molecule in its charged (neutral) state. A horizontal line of these shapes represent the full system with all molecules; where a single molecule is in its charged state. The arrow denotes which matrix element this saved as. . . . .	103
5.2	The time taken to calculate just the electrostatic interactions within CP2K for a nine thousand atom system using various methods. PME is particle mesh Ewald, SPME is smooth-PME, Ewald is the standard ewald method. The dashed line shows the time taken for a single FOB-SH step. . . . .	104
5.3	A depiction of the decomposition of the forces and energies within FOB-SH. First the all neutral VDW forces/energies are computed (blue ovals). Second the intra-molecular forces for each charged (neutral) molecule, represented by a red (blue) rectangle. The site-energy/force is then computed as a summation of all molecules in their neutral state with a molecule in its neutral state subtracted and the same molecule in its charged state added.	105
5.4	Time taken to run surface hopping and electrostatics for various lengths of one dimensional ethylene chain (left) and eight hundred molecule pentacene plane (right). Darker colors show data from the recalculation method for the electrostatics and less saturated colors to the right show data from the addition subtraction scheme. Green bars show the time taken to calculate real space interactions, red is reciprocal, yellow is the bonded corrections and blue shows all other parts of the surface hopping code. In the right pane reciprocal interactions are omitted as they took too long to run. . . .	111
5.5	A comparison of forces and energies calculated with multiple classical MD simulations (x-axis) and the addition-subtraction method with Ewald electrostatics. The left pane shows the magnitude of the outputted forces and the right the outputted potential energies. Black dots show values from each atom and timestep. The red dashed line shows $y = x$ and serves as a guide for the eye. . . . .	112

5.6 Comparison of Ewald and DSF forces and energies. The x-axis shows results from Ewald simulations and the y-axis shows results from DSF simulations. The left pane shows the force magnitude with black dots representing values from all atoms at all timesteps. The right pane shows potential energies from each timestep. The red line shows the line $y=x$ and is a guide for the eye. . . . .	115
5.7 Comparison of DSF forces and energies using multiple topology files (x axis) and classical MD and using the addition-subtraction scheme within SH (y axis). The left pane shows the force magnitude with black dots representing values from all atoms at all timesteps. The right pane shows potential energies from each timestep. The red line shows the line $y=x$ and serves as a guide for the eye. . . . .	117
5.8 A comparison of energies and forces as calculated by full Ewald and DSF electrostatics. . . . .	118
5.9 Timing data on the DSF implementation compared to Ewald electrostatics and FOB-SH without any electrostatics. The blue curve shows Ewald timing data, the orange is DSF and green is without any electrostatics. . .	119
C.1 A crude demonstration of the principle behind the smoothing procedure in switching between intercepts. The black line shows an intercept begin to diverge and the alternative intercept is shown in purple. As the step is incremented the amount of the alternative intercept that makes up the effective intercept is increased until only 1 intercept is used. . . . .	131
D.1 Rabi oscillation occurring within a Ethylene trimer system. Dotted lines were calculated using equation (D.2), solid lines were calculated using the RK4 propagator within the CTMQC section of the CP2K code. The norm is shown on the top as a cyan line and the x axis shows the timestep in seconds. . . . .	133
I.1 The restraint set up for 1 molecule. Each coloured zig-zag shows the atoms that are restrained. . . . .	142

J.1	Panel a) shows a system chosen to run surface hopping on, molecules in gray are fixed in place blue molecules show the active region. Panel b) shows every substructure chosen in the 0ns quenched structure. . . . .	143
J.2	The 100ns quenched structure clustered by layer. Each different colour represents a different cluster, labelled with the numbers around the edge of the structure. . . . .	144
J.3	The clusters chosen to run surface hopping simulations on. The coloured clusters each represent a different structure on which surface hopping was ran. . . . .	145
K.1	Experimental and computed charge mobilities for amorphous, polycrystalline and single-crystalline pentacene. . . . .	147

# List of Tables

4.1 Properties of pentacene in different bulk structures and in ultrathin (2D) films. . . . .	91
---	----

# Chapter 1

## Introduction

### 1.1 Charge Transport in Organic Semiconductors

#### 1.1.1 Organic Semiconductors

Conductive polymers were first discovered in 1977 by Shirakawa et al<sup>18,19</sup> for which they were awarded the Nobel prize in Chemistry. Since then, these materials have become widespread in many technologies, such as in organic photovoltaic cells<sup>20</sup>, organic field-effect transistors (OFET)<sup>21</sup> and organic light-emitting diodes (OLEDs)<sup>22</sup>. While the other two technologies lag behind their inorganic counterparts, uptake of OLED screens is becoming ubiquitous -especially in the smartphone and television market due to their flexibility, better colour representation and lower energy consumption than standard back-lit LCD displays. OLEDs have also found uses in lighting with their efficiency rivalling that of fluorescent tubes<sup>23,24</sup>. Although industry has made large strides in fabricating and using these materials the exact nature of the charge transport is still poorly understood. Traditional theories (such as hopping and band transport) aren't applicable to many relevant materials<sup>25–29</sup> as charge transfer dynamics lies in an intermediate region where the charge carrier forms a polaron, a deformation of the atomic positions caused by the presence of a charge carrier, which is neither fully localised or delocalised. In organic semiconductors, typical values of the localisation of the polaron are between two → twenty molecules. This is due to crystals typically being formed of organic molecules weakly held together by Van der Waals (VDW) forces rather than strong covalent bonds. This allows molecules to fluctuate about their lattice sites and introduces larger quantities

of (dynamic) disorder than is present in inorganic crystals.

There are a number of theoretical techniques currently used in the field to evaluate the performance of organic semiconductors, though all come with their own caveats. For example, transient localisation theory (TLT)<sup>28,30,31</sup>, while efficient and accurate, cannot be used in non-periodic systems or those with large amounts of static disorder. Another technique, multi-configurational time-dependent Hartree (MCTDH)<sup>32,33</sup>, is considered the gold standard for wavepacket propagation and has been used extensively in numerous studies (e.g. refs 34-36). However, due to the treatment of the full system (including nuclei) quantum mechanically, MCTDH is relatively expensive and can only be applied to a small molecular systems. In this work I will be studying electron-nuclear propagation methods that rely on the treatment of the nuclear degrees of freedom classically and the electronic ones quantum mechanically. This approximation is termed the semi-classical approximation and allows the efficient simulation of mesoscopic systems.

There are a number of semi-classical, mixed quantum-classical (MQC), techniques used in the field. The most common are fewest switches surface hopping (FSSH)<sup>34</sup> and mean-field dynamics (also called Ehrenfest dynamics)<sup>35</sup>. In addition to these, in this work I will be exploring a relative newcomer to the (nonadiabatic) semi-classical simulation arsenal, namely coupled-trajectory mixed quantum-classical molecular dynamics (CTMQC). I will be focussed on the extension of these algorithms and their application to organic semiconducting systems, containing a hundreds of molecules.

## 1.2 Semi-classical Nonadiabatic Molecular Dynamics

Semi-classical techniques all treat nuclear and electronic degrees of freedom independently and propagate nuclei with Newton's equations using standard molecular dynamics<sup>36</sup>. Here the forces are calculated with a parameterised forcefield and positions and velocities are often updated with the velocity Verlet technique. The forcefield outlines the shape of the potential energy surface (PES) the nuclei evolve on. The electronic subsystem is propagated using a variety of techniques that solve the time-dependent Schrödinger equa-

tion. There are numerous techniques for calculating electronic properties used in propagation, though the most common are density functional theory (DFT) and model Hamiltonian based methods. However, in nonadiabatic processes (such as in charge transfer<sup>37</sup> or photoexcitation<sup>38–40</sup>) the nuclear and electronic subsystems are not independent. That is, the specific nuclear geometry depends on the electron density and vice-versa. The resulting interaction between these two subsystems is the way each of the semi-classical techniques differ. In this regime the Born-Oppenheimer approximation (BOA) cannot be applied<sup>41</sup>. This approximation used for almost a century,<sup>42</sup> hinges on the fact that nuclei are much more massive than electrons and are approximately stationary with respect to electron motion<sup>43</sup>. This results in nuclear evolution that is governed by a single, adiabatic, potential energy surface. Nonadiabatic molecular dynamics methods, such as the aforementioned surface hopping and mean-field techniques, facilitates the bypassing of this limitation and can be used to simulate molecular dynamics with electronic transitions. Although the BOA has been used for almost a century, considerable discussion was underway regarding the account of electronic transitions between energy levels since the late 1920’s<sup>44–47</sup>.

### 1.2.1 Ehrenfest Dynamics

The oldest, and most intuitive, NAMD method is Ehrenfest dynamics<sup>35</sup>. In this technique the nuclei evolve on a single, mean potential energy surface (PES). The shape of this PES comes from an average of the adiabatic energies weighted by the population of each adiabatic state (population-weighted average). Hence the electronic subsystem can influence the nuclear dynamics through the PES. This method of propagation is displayed for a simple 1D, one atom, two state system in figure 1.1. In this figure we initialise the adiabatic population in the ground (red) state. As the atom (black dot) progress through the reaction coordinates it feels forces equal to the negative gradient of the population-weighted average PES (dotted black line).

The Ehrenfest equations can be rigorously derived from the time-dependent Schrödinger

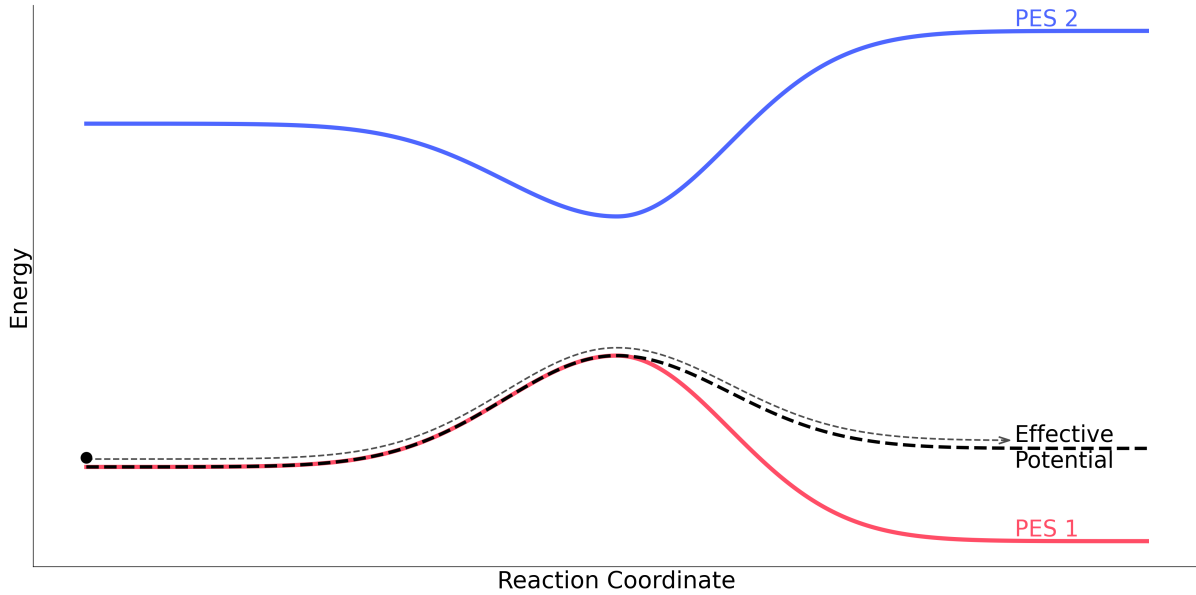


Figure 1.1: An example of a typical Ehrenfest simulation near an avoided crossing. The black line represents the adiabatic potential energy surface due to the effective potential energy surface, which is a population-weighted average of the ground and excited state (red and blue lines respectively). The black dashed line shows an example of a path taken by an atom travelling in this system.

equation by expanding the full electronic wavefunction as a linear combination of adiabatic states as in equation (1.1).

$$\Psi(\mathbf{r}, \mathbf{R}, t) = \sum_m^{N_{st}} C_m(\mathbf{R}, t) \psi_m(\mathbf{r}, t) \quad (1.1)$$

Where the full electronic wavefunction  $\Psi(\mathbf{r}, \mathbf{R}, t)$  is expanded as a sum of adiabatic expansion coefficients  $C_m$  multiplied by an adiabatic basis function  $\psi_m$ . In the software considered in this thesis, the adiabatic basis functions are never calculated. This is because the propagation is carried out in the diabatic basis. All adiabatic quantities (such as the adiabatic expansion coefficients) can be calculated by through quantities transformed from the diabatic to the adiabatic basis. This transformation is carried out with the transformation matrix –constructed from the eigenvectors of the electronic Hamiltonian. The norm of the adiabatic expansion coefficients gives the probability of finding the

wavefunction in state  $m$ .

$$\mathbf{F}_v^{Ehren} = -\sum_m^{N_{st}} |C_m|^2 \nabla_v E_m - \sum_{m \neq n}^{N_{st}} C_m^* C_n (E_n - E_m) \mathbf{d}_{mn,v}^{ad} \quad (1.2)$$

In equation (1.2) the force,  $\mathbf{F}$ , for each atom,  $v$ , is the sum of the adiabatic population,  $|C_m|^2$ , on each state,  $m$ , multiplied by the gradient of the adiabatic energy of state  $\nabla_v E_m$  plus the sum over pairs of adiabatic states,  $m$  and  $n$ , of the adiabatic expansion coefficients,  $C_{m(n)}$  multiplied by the energy difference  $E_n - E_m$  multiplied by the nonadiabatic coupling vector  $\mathbf{d}_{mn,v}^{ad}$  on atom  $v$ , in the adiabatic basis. The adiabatic energies are calculated as the eigenvalues of the Hamiltonian. In equation(1.2) above the first term shows the negative gradient of the population-weighted average potential energy surface. The second term gives a coupling force due to pairs of states and is non-zero only if there is a mixing of states (i.e. population on more than a single adiabatic state).

The equation for the propagation of the adiabatic expansion coefficients is given in equation (1.3).

$$i\hbar \dot{C}_m = C_m E_m - i\hbar \sum_n^{N_{st}} C_n \sum_v \mathbf{v}_v \cdot \mathbf{d}_{mn,v}^{ad} \quad (1.3)$$

We can see in this equation any mixing of electronic population between states is initially stimulated by the dot between the nonadiabatic coupling vector and the nuclear velocity,  $\sum_v \mathbf{v}_v \cdot \mathbf{d}_{nm,v}^{ad}$ . In figure 1.1 the coupling would be highest near the middle of the figure, where the two PES come the closest to each other, so populations would only start mixing when the nuclei reached this point. This, and the fact that the Hamiltonian (and therefore adiabatic energies) is a function of nuclear positions, is the method of feedback from the nuclear to the electronic subsystem.

Although the Ehrenfest method has been applied with success in many systems<sup>48–50</sup> it has a number of key shortcomings. Namely, its inability to capture the branching of the nuclear wavefunction (as propagation occurs on only a single PES) and its poor account of the decoherence of the electronic and nuclear subsystem after an avoided crossing. Ehrenfest also violates detailed balance and prevents the thermodynamic equilibration of

the system by populating all adiabatic states evenly<sup>41,51</sup>. In the limit of infinite states this results in infinite electronic temperature<sup>52</sup>. For this reason many people choose to use fewest switches surface hopping. Both surface hopping and Ehrenfest conserve vital quantities such as the norm of the electronic populations and total energy (kinetic + potential).

### 1.2.2 Surface hopping

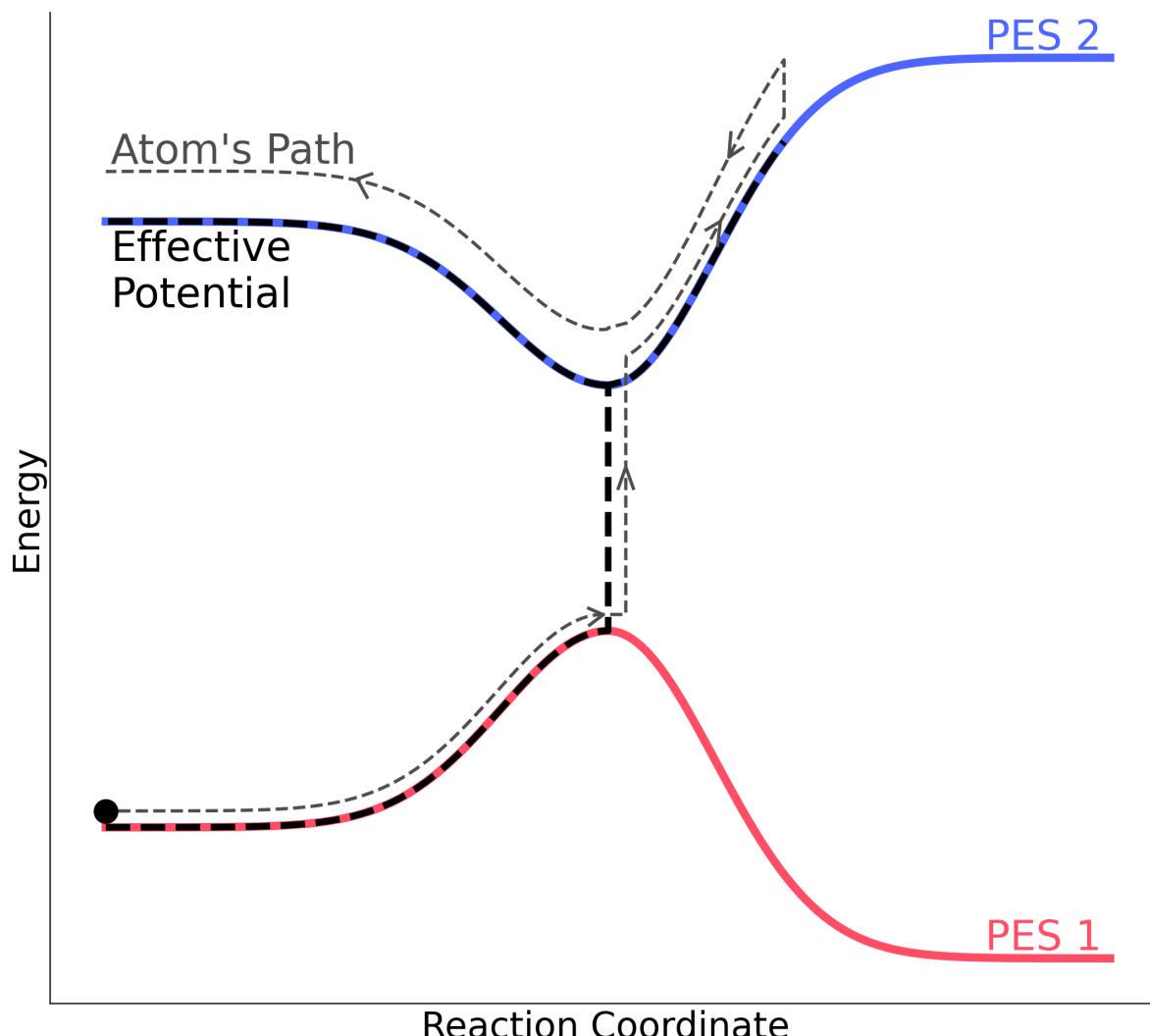


Figure 1.2: An example of a typical surface hopping simulation near an avoided crossing. The black line represents the effective potential energy surface the nuclei (black dot) travel on. This is a discontinuous combination of ground (red line) and excited (blue line) states. The current PES the nuclei are travelling on is denoted the ‘active’ state.

Surface hopping was devised to circumvent the limitations of mean-field NAMD. To do this a swarm of trajectories is initialised and allowed to propagate independently throughout the system. These trajectories represent the nuclear wavepacket and can have varied paths depending on the topology of the system. As in Ehrenfest, the electronic wavefunction is decomposed into a linear combination of adiabatic states. However, unlike Ehrenfest, the force experienced by the nuclei is only the negative spatial derivative of the PES of the ‘active state’. Initially this active state is selected by the user -to resemble to conditions of the system of interest. However, for all proceeding steps it is determined by a series of discrete hops between states. These hops are determined by the ‘hopping probability’, which is proportional to the strength of couplings between states, the energy difference between the active state and the new state, the nuclear velocities and the adiabatic coefficients. It is important to note that the adiabatic coefficients are a different quantity to the active state. These are propagated via the Schrödinger equation and give the probability of finding the charge carrier on a particular state for a given configuration. The average over trajectories of the active states (termed the surface population) should be equal to the adiabatic population. If this holds the propagation is said to be ‘internally consistent’. During each hop the potential energy instantly changes and a correction is applied to the kinetic energy, via a rescaling of the nuclear velocities (along the direction of the non-adiabatic coupling vector –NACV), to conserve total energy. This is demonstrated for a single trajectory in figure 1.2. In this cartoon, the active state is initially the ground (red) state. As the atom travels towards the avoided crossing (region of high non-adiabatic coupling), the likelihood of a hop increases. A random number is used to decide whether the hop occurs. A hop is shown towards the centre of figure 1.2. After the atom has hopped to the upper surface it experiences forces equivalent to the negative gradient of the PES. In this situation it results in the atom begin reflected at the avoided crossing. Some trajectories will hop here and some won’t (depending on the coupling strength) resulting in a branching of the nuclear wavepacket. This is in contrast to Ehrenfest, where all trajectories travel along the same PES, meaning the nuclear wavepacket cannot branch.

The propagation of the adiabatic expansion coefficients is the same as for Ehrenfest

and is given in equation (1.3). This results in two forms of adiabatic populations, the surface population (the fraction of trajectories on each PES) and the adiabatic population (the population of the adiabatic expansion coefficients). These two populations should agree and when they do the system is said to obey internal consistency. The forces are given by the negative gradient of the potential energy surface the trajectory is travelling on. This is given in equation (1.4)

$$\mathbf{F}_v = -\nabla_v E_i \quad (1.4)$$

Where the force on atom  $v$  is equal to the gradient (with respect to atom  $v$ ) of potential energy surface  $i$ .

Although surface hopping fixes many concerns from Ehrenfest dynamics there are still caveats to be aware of. The original ‘fewest switches surface hopping’ proposed by John Tully suffered from bad overcoherence of the nuclear and electronic subsystems. That is the electronic and nuclear motion was coupled long after the region of high non-adiabatic coupling (crossing region). There have been attempts to fix this by introducing a decoherence time, after which the adiabatic population is forced to occupy a single state (either instantly or exponentially damped). However, the parameterisation of this time isn’t trivial and many methods have been proposed. A decoherence method where non active adiabatic populations are exponentially damped and the active state is adjusted to conserve the norm is used in this work. The damping time is based on Heisenberg uncertainty principle and the energy difference between the active state and the inactive states. Full details of this method are given in refs<sup>53,54</sup>.

Further deficiencies of trajectory surface hopping are the fact that the hops are instant which can lead to discontinuities in the total energy. The standard methods to compensate for this is re-scaling velocities along the direction of the NACV (as mentioned previously). Due to the nuclear timestep being finite trivial crossings can be missed while propagating the system. This is because when adiabatic states become very close to each other (or even totally degenerate) the nonadiabatic coupling can form a

large, sharp peak with respect to the reaction coordinate. If the nuclear timestep is too large this large peak can be completely missed leading to several artifacts. There have been various solutions proposed that are referenced in ref<sup>54,55</sup>. In this work, I will use the self-consistent surface hopping correction introduced by Wang and Prezhdo<sup>56</sup>. A final shortcoming of surface hopping is that it has not been derived from first principles and cannot be guaranteed to work generally. Though, in practice, surface hopping has been widely adopted and tested on a variety of systems and its suitability for use in these has been reported and many problems have been addressed<sup>55</sup>.

A flavour of surface hopping that has proved remarkably effective at simulating, large, organic, semi-conducting, systems is fragment orbital-based surface hopping (FOB-SH)<sup>57</sup>. This technique combines Tully's fewest switches surface hopping, the corrections mentioned above, and fast coupling calculations through the analytic overlap method (AOM)<sup>58</sup> to simulate systems of hundreds to thousands of organic molecules. This method has been discussed in numerous publications<sup>26,53,54,57,59–63</sup> so I will provide only a brief outline here.

### 1.2.3 FOB-SH

Dynamics within the system are dictated by a simplified 1-particle Hamiltonian (given in equation (1.5)).

$$H = \sum_k \epsilon_k |\phi_k\rangle\langle\phi_k| + \sum_{k \neq l} H_{kl} |\phi_k\rangle\langle\phi_l| \quad (1.5)$$

where  $\phi_k = \phi_k(\mathbf{r}, \mathbf{R}(t))$  is the HOMO/LUMO of molecule  $k$ ;  $\mathbf{r}$  is the position of the hole/electron;  $\mathbf{R}(t)$  are the time-dependent nuclear coordinates;  $\epsilon_k = \epsilon_k(\mathbf{R}(t))$  is the site energy, that is, the potential energy of the state with the hole/electron located at site  $k$ ; and  $H_{kl} = H_{kl}(\mathbf{R}(t))$  is the electronic coupling between  $\phi_k$  and  $\phi_l$ . All Hamiltonian matrix elements, i.e. site energies and couplings, depend on the nuclear coordinates which, in turn, depend on time,  $\mathbf{R} = \mathbf{R}(t)$  as determined by the nuclear dynamics.

The Hamiltonian is an electronic tight-binding one and its elements are efficiently calculated through two main approximations. Firstly, the diagonal elements are calculated via a classical force-field, where for each element the respective molecule is parameterised in its charged state and all others in their neutral state. Secondly, the off-diagonal elements are calculated via the analytic overlap method (AOM)<sup>58</sup>. This relies on 2 assumptions: (i) there is a linear relationship between the off-diagonal  $H_{kl}$  elements and the overlap between projected fragment-orbitals into Slater-type orbitals and (ii) there is an analytic expression for the overlap matrix,  $S_{kl}$ . Full details can be found in the surrounding literature, e.g: refs 57 and 58.

The term ‘fragment-orbital’ refers to the fact that the band state of the crystal is, to a good approximation, represented by a linear combination of HOMO/LUMO states on single molecules. Other states are excluded in the interest of efficiency. That is, it is assumed only the frontier, HOMO/LUMO, energy levels are involved in charge transfer. This approximation is motivated by the fact that the gap between HOMO and HOMO-1 energy levels is often much larger than typical electronic couplings. In a recent work the median energy separation between these two states was found to be 0.66eV, while the median electronic coupling was 0.14eV<sup>64</sup>.

In the FOB-SH approach the charge carrier is described by a time-dependent 1-particle wavefunction,  $\Psi(t)$ , expanded in the same basis that is used to represent the Hamiltonian equation (1.5),

$$|\Psi(t)\rangle = \sum_{l=1}^M u_l(t) |\phi_l(\mathbf{R}(t))\rangle \quad (1.6)$$

where  $u_l$  are the expansion coefficients. Insertion of Equation (1.6) in the time-dependent Schrödinger equation gives the time-evolution of the hole/electron wavefunction in the valence/conduction band,

$$i\hbar\dot{u}_k(t) = \sum_{l=1}^M u_l(t) (H_{kl}(\mathbf{R}(t)) - i\hbar\hbar d_{kl}(\mathbf{R}(t))), \quad (1.7)$$

where  $d_{kl} = \langle \phi_k | \dot{\phi}_l \rangle$  are the non-adiabatic coupling elements (NACE). This quantity is the non-adiabatic coupling elements in the psuedo-diabatic basis. This means it is small but not zero. In practice, these NACEs are often omitted in the propagation, though if required they can be calculated via a finite difference method. Though details are given in this work, FOB-SH is the culmination of multiple PhD theses and journal articles and it would be impractical to provide every detail in this work. Instead, I refer the reader to previous works<sup>65,66</sup>.

The nuclear degrees of freedom are propagated on one of the potential energy surfaces (PES) obtained by diagonalizing the Hamiltonian Equation(1.5) and denoted as  $E_a$  (“ $a$ ” for “active surface”). While nuclear motion couples to the motion of the charge carrier via the dependences on  $\mathbf{R}(t)$  in Equation (1.7), feedback from the charge carrier to the nuclear motion is accounted for by transitions of the nuclear dynamics (“hops”) from the PES of the active eigenstate  $a$  to the PES of another eigenstate  $j$  using Tully’s surface hopping probability.<sup>34</sup> The FOB-SH calculations are carried out, as described previously, for single crystalline pentacene<sup>67</sup> using a decoherence correction, removal of decoherence-induced spurious long-range charge transfer, trivial crossing detection and a multiple time step algorithm. Importantly, as shown in previous work<sup>58</sup>, the electronic Hamiltonian Equation(1.5) reproduces the DFT valence band structure of single crystalline pentacene<sup>67</sup> very well.

In addition to FOB-SH, CTMQC will be studied in detail in this thesis. This is a relative newcomer on the MQC scene and is the semi-classical limit of the exact factorisation of the time-dependent Schrödinger equation.

### 1.3 Exact Factorisation and its Semi-Classical Limit

Exact factorisation<sup>68</sup> involves separating the total molecular wavefunction into a nuclear component and electronic component, where the electronic component is parametrically dependent on the nuclear coordinates,  $\mathbf{R}$ . This is shown below in eq (1.8) where  $\chi$  is the nuclear wavefunction and  $\Phi$  is the electronic one.

$$\Psi(\mathbf{R}, \mathbf{r}, t) = \Phi_{\mathbf{R}}(\mathbf{r}, t)\chi(\mathbf{R}, t) \quad (1.8)$$

In the above equation (and throughout this report) I will denote nuclear coordinates and electronic coordinates  $\mathbf{R}$  and  $\mathbf{r}$  respectively. The nuclear and electronic wavefunctions then obey separate, but coupled, time-dependent Schrödinger equations for spatial and temporal evolution. In this report, I will be focussing on the semi-classical limit of these equations, named Coupled-Trajectory Mixed Quantum-Classical Molecular Dynamics (CTMQC), and give results of my implementation of this within the FOB framework.

The two Schrödinger equations for the evolution of the electronic and nuclear wavefunctions in the exact factorisation<sup>68</sup> are given below:

$$i\hbar \frac{\partial}{\partial t} \Phi_{\mathbf{R}}(\mathbf{r}, t) = (\hat{H}_{BO} + \hat{U}_{en}[\Phi_{\mathbf{R}}, \chi] - \epsilon(\mathbf{R}, t)) \Phi_{\mathbf{R}}(\mathbf{r}, t) \quad (1.9)$$

$$i\hbar \frac{\partial}{\partial t} \chi(\mathbf{R}, t) = \left( \sum_{v=1}^{N_n} \frac{[-i\hbar \nabla_v + \mathbf{A}_v(\mathbf{R}, t)]^2}{2M_v} + \epsilon(\mathbf{R}, t) \right) \chi(\mathbf{R}, t) \quad (1.10)$$

Where  $\hat{H}_{BO}$  is the Born-Oppenheimer Hamiltonian, that is  $\hat{T}_e + \hat{W}_{ee} + \hat{W}_{nn} + \hat{V}_{en}$ . Where  $\hat{T}_e$  is the electronic kinetic energy operator,  $\hat{W}_{ee/nn}$  is the electron-electron/nuclear-nuclear interaction and  $V_{en}$  is the electronic-nuclear potential.

The  $\hat{U}_{en}$  is an electronic-nuclear coupling operator (ENCO). This is defined as

$$\hat{U}_{en}[\Phi_{\mathbf{R}}, \chi] = \sum_{v=1}^{N_{nuc}} \frac{1}{M_v} \left[ \frac{[-i\hbar \nabla_v - \mathbf{A}_v(\mathbf{R}, t)]^2}{2} + \left( \frac{-i\hbar \nabla_v \chi}{\chi} + \mathbf{A}_v(\mathbf{R}, t) \right) \left( -i\hbar \nabla_v - \mathbf{A}_v(\mathbf{R}, t) \right) \right] \quad (1.11)$$

Where the  $\mathbf{A}_v$  is a time-dependent vector potential (TDVP), given by  $\langle \Phi_{\mathbf{R}}(t) | -i\hbar \nabla_v \Phi_{\mathbf{R}} \rangle_{\mathbf{r}}$  (where the subscript  $\mathbf{r}$  denotes an integration over electronic coordinates) and  $M_v$  is the mass of nucleus  $v$ . Finally  $\epsilon(\mathbf{R}, t)$  is a time-dependent scalar potential energy surface (TDPES), given by  $\langle \Phi_{\mathbf{R}}(t) | \hat{H}_{BO} + \hat{U}_{en}^{coup} - i\hbar \frac{\partial}{\partial t} | \Phi_{\mathbf{R}}(t) \rangle_{\mathbf{r}}$ .

The effects of the TDPES, TDVP and the ENCO have been investigated in multiple works<sup>1,69–72</sup>. The TDPES and TDVP are both responsible for the evolution of the system<sup>69</sup>. The TDPES provides exact classical forces on the nuclei. In fact, an alterna-

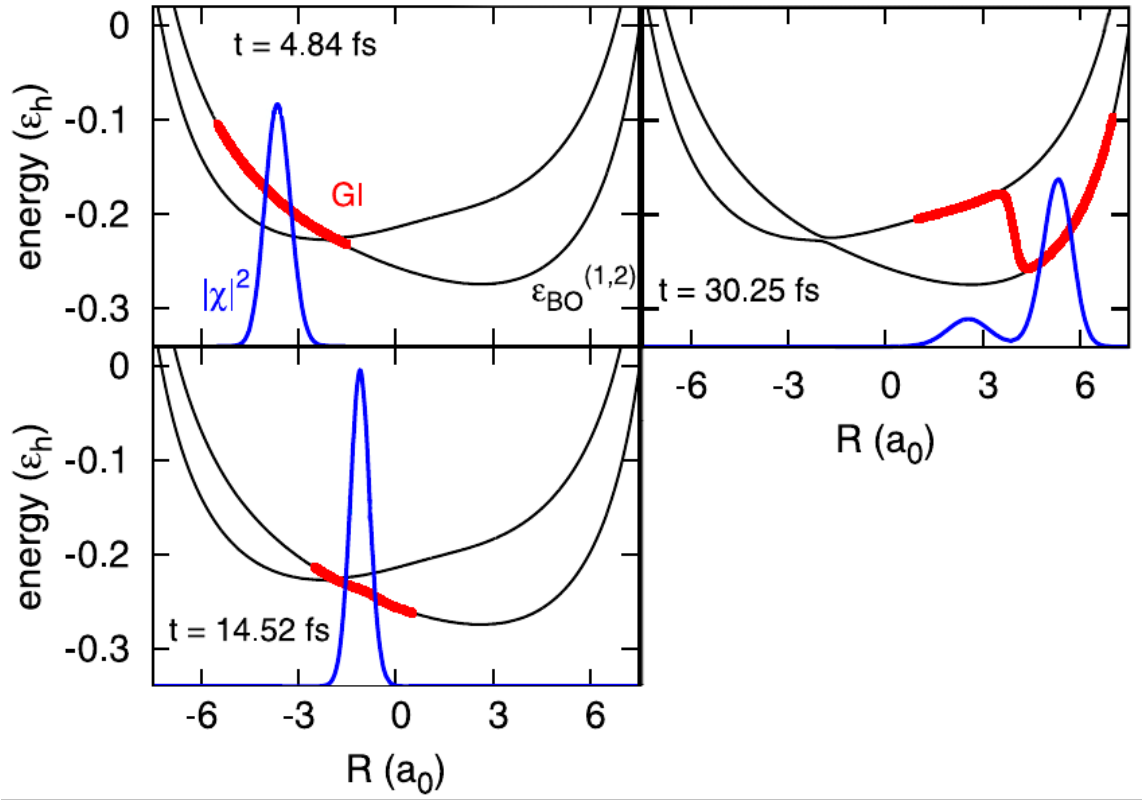


Figure 1.3: A demonstration of how the TDPES can cause the splitting of the nuclear wavepacket in non-adiabatic regions. The red line represents the TDPES and the blue is the nuclear density. Figure adapted from Agostini, 15<sup>1</sup>

tive independent-trajectory semi-classical scheme has been investigated using these exact forces<sup>1</sup>. This found the TDPES is responsible for the splitting of the nuclear wavepacket in regions of high non-adiabaticity by taking the shape of a step function between the two adiabatic potentials. This is demonstrated in figure 1.3, which was adapted from an image in Agostini, 15<sup>69</sup>. We can see that as the simulation progresses the initial nuclear density (blue curve) becomes split when the TDPES (red curve) forms a sharp step. This occurs just after the avoided crossing region. The two ends of the nuclear density then feel different forces from the two potential energy surfaces and evolve separately. Finally the electronic-nuclear coupling operator (ENCO) is responsible for other non-adiabatic effects in the system such as electronic nonadiabatic transitions and decoherence<sup>69</sup>.

## 1.4 Approximations leading to CTMQC

Starting from the exact factorisation equations, five approximations have been made to derive the CTMQC equations. These are discussed in detail in Ref.<sup>2</sup>. In the interest of completeness I have summarised them below.

### 1.4.1 Classical Nuclei

Techniques that include nuclear quantum effects (NQEs), such as multiple spawning<sup>73</sup>, ring-polymer surface hopping<sup>74</sup> and nonadiabatic Bohmian dynamics<sup>75,76</sup> although extremely accurate, cannot be applied to hundreds or thousands of molecules, due to their high computational cost. Further, for charge transfer in systems studied in this paper NQEs are negligible, especially at room temperature. For this reason the classical limit of the nuclear Schrödinger equation (1.10) is taken when deriving the CTMQC equations.

### 1.4.2 Neglect the ENCO in the TDPES

The electron-nuclei coupling operator is omitted in the expression for the time-dependent potential energy surface. This is justified as the first term ( $[-i\hbar\nabla_v - \mathbf{A}_v(\mathbf{R}, t)]^2$ ) contains a second order derivative which is expensive to calculate and has a negligible effect compared to the second term in the ENCO<sup>77</sup>. However, the rest of the ENCO is equal to zero when averaged over  $\Phi_{\mathbf{R}}(\mathbf{r}, t)$  so it does not contribute to the TDPES.

### 1.4.3 Derivative of the Adiabatic Coefficients

The derivative of the adiabatic coefficients appears in the electronic evolution equations. However, we can re-write the derivative of the adiabatic coefficients in terms of their modulus and phase:

$$\nabla_v C_l^{(I)}(t) = \left[ \underbrace{\frac{\nabla_v |C_l^{(I)}(t)|}{|C_l^{(I)}(t)|}}_{\text{(Term 1)}} + \underbrace{\frac{i}{\hbar} \nabla_v \gamma_l^{(I)}(t)}_{\text{(Term 2)}} \right] C_l^{(I)}(t) \quad (1.12)$$

It has been found that the first term is negligible compared to the second<sup>1,70,71</sup> so it doesn't need to be calculated and we can remove it. It was also assumed that the NACVs are localised in space meaning that, after some algebra, the spatial derivative of the

adiabatic coefficient can be written as:

$$\nabla_v C_l^{(I)}(t) = \frac{i}{\hbar} \nabla_v \gamma_l^{(I)}(t) C_l^{(I)}(t) = -\frac{i}{\hbar} \int^t dt' \nabla_v E_l^{(I)} C_l^{(I)}(t') = -\frac{i}{\hbar} \mathbf{f}_l^{(I)} C_l^{(I)}(t) \quad (1.13)$$

Where  $E_l^{(I)}$  is the energy of the  $l^{th}$  adiabatic potential energy surface for trajectory I,  $C_l^{(I)}$  is the adiabatic expansion coefficient for state  $l$  and trajectory I. The  $\mathbf{f}_l^{(I)}$  is the time-integrated adiabatic force (adiabatic impulse).

#### 1.4.4 Gaussian Nuclear Wavepackets

In order to calculate the quantum momentum –the new term in CTMQC– knowledge of the nuclear distribution is needed. However, as we treat the nuclei as point particles we need to re-construct the nuclear density from the atomic positions. This is done by smoothing out the atomic positions by placing a Gaussian of width  $\sigma$  centered on each atomic position and combining these gaussians to produce the final nuclear density. This introduces an empirical parameter ( $\sigma$ ) which will be discussed later in this thesis. It should be noted, the nuclei are still propagated classically, the width parameter is only used in the calculation of the quantum momentum.

#### 1.4.5 Separating the Effects of Decoherence and NACVs

So as to not introduce any population transfer (due to the quantum momentum) when the NACV is zero a fifth approximation has been introduced. Namely the quantum momentum depends on pairs of states,  $l, k$ . This enables the separation of the ‘competing’ effects of the NACV and the Quantum Momentum.

## 1.5 The CTMQC equations

### 1.5.1 Adiabatic Basis

The equations for the propagation of the classical nuclei and the expansion coefficients in the CTMQC framework in the adiabatic basis are given below:

$$\dot{\mathbf{P}}_{\mathbf{v}}^{(I)} = - \underbrace{\sum_k |C_k^{(I)}|^2 \nabla_{\mathbf{v}} E_k^{(I)} - \sum_{k,l} C_l^{(I)} C_k^{*(I)} (E_k^{(I)} - E_l^{(I)}) \mathbf{d}_{\mathbf{v},lk}^{(I)}}_{\text{Ehrenfest}} - \underbrace{\sum_{l,k} |C_l^{(I)}|^2 \left( \sum_{\mathbf{v}'=1}^{N_n} \frac{2}{\hbar M_{\mathbf{v}'}} \mathcal{Q}_{lk,\mathbf{v}'}^{(I)} \cdot \mathbf{f}_{l,\mathbf{v}'}^{(I)} \right) \left[ |C_k^{(I)}|^2 \mathbf{f}_{k,\mathbf{v}}^{(I)} - \mathbf{f}_{l,\mathbf{v}}^{(I)} \right]}_{\text{Quantum Momentum}} \quad (1.14)$$

$$\dot{C}_l^{(I)} = - \underbrace{\frac{i}{\hbar} E_l^{(I)} C_l - \sum_k C_k^{(I)} d_{lk}^{ad(I)}}_{\text{Ehrenfest}} - \underbrace{\sum_{\mathbf{v}=1}^{N_n} \sum_k \frac{\mathcal{Q}_{lk,\mathbf{v}}^{(I)}}{\hbar M_{\mathbf{v}}} \cdot \left[ \mathbf{f}_{k,\mathbf{v}}^{(I)} - \mathbf{f}_{l,\mathbf{v}}^{(I)} \right] |C_k^{(I)}|^2 C_l^{(I)}}_{\text{Quantum Momentum}} \quad (1.15)$$

Where the  $E_k$  term is the potential energy on the  $k^{th}$  potential energy surface.  $C_l$  is the adiabatic expansion coefficient corresponding to the  $l^{th}$  state. The sum over  $k$  and  $l$  indicates a sum over all states, the  $(I)$  superscript is a trajectory index and the  $\mathbf{v}$  is an atom index.  $M_{\mathbf{v}}$  is the nuclear mass and  $d_{lk}^{ad(I)}$  represents the non-adiabatic coupling element (in the adiabatic basis) between adiabatic states  $l$  and  $k$ . The two new terms in this scheme not seen in other NAMD methods are the  $\mathcal{Q}_{lk,\mathbf{v}}^{(I)}$  and the  $\mathbf{f}_{k,\mathbf{v}}^{(I)}$ . These are the quantum momentum and the adiabatic impulse. The adiabatic impulse term is defined in equation (1.13) this keeps a record of the previous forces on each adiabatic state in the system. The quantum momentum term couples the trajectories together (making this a coupled-trajectory scheme). This coupling occurs as the quantum momentum is calculated from the nuclear density, i.e.  $|\chi|^2$ , and the nuclear density is reconstructed from the position of each trajectory. More details are given in 1.5.2. Together the history dependent force and quantum momentum are responsible for the decoherence in the ‘Quantum Momentum’ parts of the above equations<sup>3</sup>. Notably, although these equations

have been derived from the exact factorisation equations separately from Ehrenfest they do contain the Ehrenfest equations within them (marked ‘Ehrenfest’). This scheme can therefore be seen as an Ehrenfest scheme with a correction that captures branching of the nuclear wavefunction and decoherence within it.

We can also see in equation (1.15) if we are in a pure adiabatic state i.e. all population on a single adiabatic state, there is no contribution from the quantum momentum part of the equations. In this scenario the evolution equations become simply Ehrenfest equations. For example, if all the population is localised on a single adiabatic state then the term  $|C_k^{(I)}|^2 C_l$  is only non-zero when  $l = k$ . However, when  $l = k$ , the term  $[\mathbf{f}_{k,v}^{(I)} - \mathbf{f}_{l,v}^{(I)}]$  is zero as  $\mathbf{f}_{k,v}^{(I)} = \mathbf{f}_{l,v}^{(I)}$ . Therefore, the quantum momentum term can be seen to only kick in when there is a mixing of adiabatic states. In the adiabatic formulation of these equations it is the adiabatic NACV  $\mathbf{d}_{lk,v}^{ad,(I)}$  that is responsible for the initial mixing of the populations from pure adiabatic states.

### 1.5.2 Calculating the Quantum Momentum

The technique for calculating the quantum momentum term is outlined in detail in the SI of min, 17<sup>78</sup>. The original equations given in Agostini, 16<sup>2</sup> present a quantum momentum term without state indices ( $l, k$ ). This, due to approximations made in the derivation of CTMQC, results in population transfer even when the non-adiabatic couplings between states are zero. Therefore, Agostini et al enforced this condition with the pair-wise state dependence on the quantum momentum. The quantum momentum is defined in equation (1.16) as:

$$\mathcal{Q}_v^{(I)} = \frac{-\hbar \nabla_v |\chi^{(I)}|}{|\chi^{(I)}|} \frac{-\hbar \nabla_v |\chi^{(I)}|^2}{2|\chi^{(I)}|^2} \quad (1.16)$$

In order to reconstruct the nuclear density, Gaussian distributions are used as in equation (1.17) below:

$$|\chi^{(I)}(t)|^2 = \frac{1}{N_{tr}} \sum_{J=1}^{N_{tr}} \prod_{v=1}^{N_n} g_{\sigma_v^{(J)}(t)} \left( \mathbf{R}_v^{(I)}(t) - \mathbf{R}_v^{(J)}(t) \right) \quad (1.17)$$

Where,  $N_{tr}$  is the number of trajectories,  $N_n$  is the number of atoms,  $\sigma_v^{(J)}(t)$  is a time-dependent width parameter for each Gaussian  $g$  and  $\mathbf{R}_v^{(J)}$  represents the atomic position

of atom  $v$  on trajectory  $J$ .

This results in a linear expression for the quantum momentum. The full details of the derivation are given in the supplementary information of Min, 17<sup>78</sup>. The resulting linear expression for the quantum momentum is given below:

$$\mathcal{Q}_{lk,v}^{(I)} = \alpha_v^{(I)} \mathbf{R}_v^{(I)} - \mathbf{R}_{lk,v} \quad (1.18)$$

Where  $\mathbf{R}_v^{(I)}$  are the nuclear coordinates on trajectory I on atom  $v$ . The  $\alpha_v^{(I)}$  term is a weighted average over trajectories of the product of the Gaussian's assigned to each atomic coordinate, i.e:

$$\alpha_v^{(I)} = \sum_J^{N_{tr}} \frac{\hbar \prod_{v'} g_{\sigma_{v'}^{(J)}(t)} \left( \mathbf{R}_{v'}^{(I)}(t) - \mathbf{R}_{v'}^{(J)}(t) \right)}{2\sigma_v^{(J)}(t)^2 \sum_K^{N_{tr}} \prod_{v'} g_{\sigma_{v'}^{(K)}(t)} \left( \mathbf{R}_{v'}^{(I)}(t) - \mathbf{R}_{v'}^{(K)}(t) \right)} \quad (1.19)$$

Note that  $\alpha_v^{(I)}$  is not dimensionless here, the quantum momentum intercept term ( $\mathbf{R}_{lk,v}$ ) has different units to the nuclear positions ( $\mathbf{R}_v^{(I)}$ ). This can be seen in equation (1.20). Along with the  $\mathbf{R}_{lk,v}$  term the  $\alpha_v^{(I)}$  performs the job of coupling the trajectories together. The  $\mathbf{R}_{lk,v}$  term also given in the SI of Min, 17<sup>78</sup> is defined for each Cartesian dimension as:

$$R_{lk,v} = \sum_I^{N_{tr}} R_v^{(I)}(t) \alpha_v^{(I)}(t) \frac{|C_k^{(I)}(t)|^2 |C_l^{(I)}(t)|^2 (f_{k,v}^{(I)}(t) - f_{l,v}^{(I)}(t))}{\sum_J |C_k^{(J)}(t)|^2 |C_l^{(J)}(t)|^2 (f_{k,v}^{(J)}(t) - f_{l,v}^{(J)}(t))} \quad (1.20)$$

Where the bold notation for vectors has been replaced by normal font. This means that this equation applies to each Cartesian dimension independently. Further, in this expression  $R_{lk,v}$  is symmetric,  $R_{lk} = R_{kl}$  meaning that  $Q_{lk} = Q_{kl}$ . It is also undefined on the diagonals as the denominator is 0, diagonal values are therefore set to 0. At first sight, the  $R_{lk}$  term seems to be another weighted average. However, this isn't quite the case as the denominator can be negative. This causes equation (1.20) to be very sensitive to errors in the calculation of the denominator of this fraction. Any inaccuracies can lead to the denominator approaching zero faster than the numerator causing large spikes in the quantum momentum term. This will be discussed in greater detail in the following

chapters.

## Chapter 2

# CTMQC applied to the Tully Models

The Tully models, first proposed by John Tully in 1990<sup>79</sup>, are a collection of simple one dimensional model systems. They were designed to be simple enough to obtain accurate quantum results to benchmark new nonadiabatic molecular dynamics (NAMD) methods against. Originally there were three, one dimensional, single atom models. However, in this work an extra model has been introduced with parameters taken from Gossel<sup>3</sup>. This is to allow a full comparison of my implementation of CTMQC with the literature. In this chapter my implementation of CTMQC will be tested using these model systems and by comparing my results with those in the literature.

In each of the Tully models the (diabatic) Hamiltonian is a function of nuclear positions,  $\mathbf{R}$  and is a  $2 \times 2$  matrix that takes the form:

$$\hat{H} = \frac{\hat{P}^2}{2M} + \begin{pmatrix} H_{11}(\mathbf{R}) & H_{12}(\mathbf{R}) \\ H_{21}(\mathbf{R}) & H_{22}(\mathbf{R}) \end{pmatrix} \quad (2.1)$$

The nuclear mass has been set to 2000 a.u.. This was set to be very close to the proton's mass of 1836 a.u. so we can expect significant quantum effects that classical theory couldn't replicate. The values of the Hamiltonian matrix elements are set to produce systems that resemble common features in a typical nonadiabatic simulation such as avoided crossings and regions of extended coupling. The parameters used in each systems' Hamiltonian where taken from Gossel<sup>3</sup> in order to compare the 2 implementations. These can be found in appendix A.

In order to propagate dynamics in the adiabatic basis we need to calculate various quantities from the Hamiltonian at each timestep. These are, for Ehrenfest, the (adiabatic) nonadiabatic coupling vector ( $\mathbf{d}_{lk}^{(I)}$ ) and the adiabatic energies ( $E_l^{(I)}$ ). In the full CTMQC simulations we must also calculate the adiabatic impulse term  $\mathbf{f}_l^{(I)}$  from the Hamiltonian. The adiabatic energies are the eigenvalues of the Hamiltonian. The adiabatic NACV can be calculated via a finite difference method and equation (2.2) below.

$$\mathbf{d}_{lk}^{(I)} = \langle \psi_l^{(I)} | \nabla \psi_k^{(I)} \rangle \quad (2.2)$$

where  $\psi_l^{(I)}$  is the adiabatic electronic basis function for adiabatic state  $l$ . This is given by the eigenvector of the Hamiltonian, on replica  $I$ , corresponding to state  $l$ . Illustrations of these two properties can be found below in fig 2.1 for each of the four models systems.

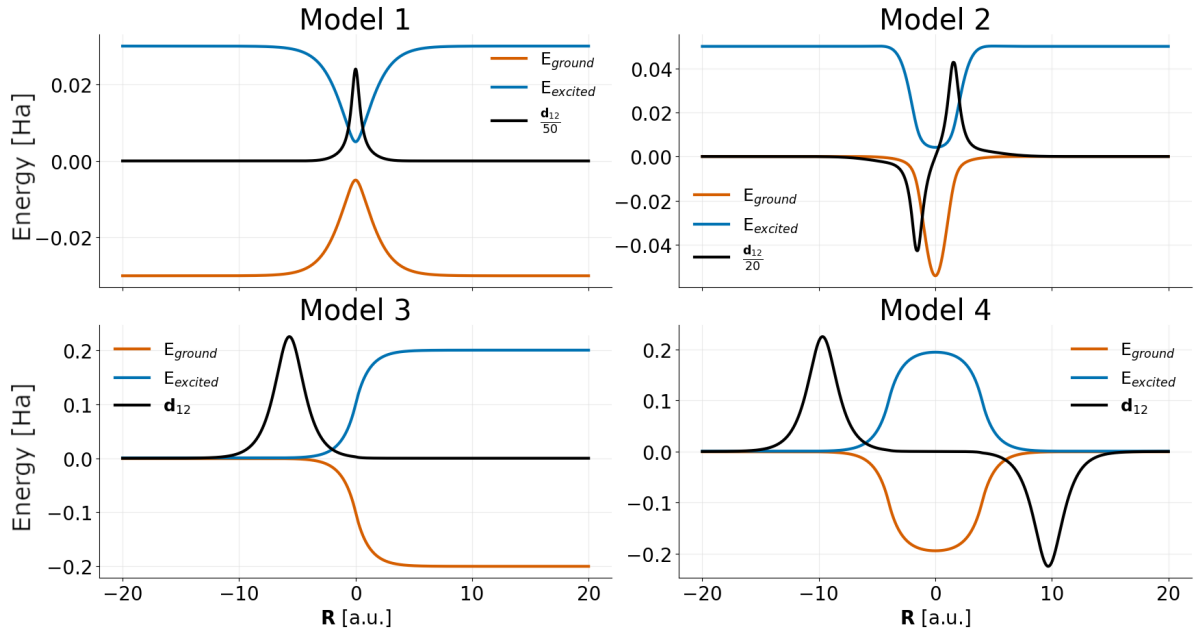


Figure 2.1: Adiabatic potential energy surfaces (orange and blue) and element 1, 2 of the non-adiabatic coupling vector (black) for the four model systems. For parameters see appendix A.

In order to initialise the simulations coordinates and velocities were sampled from the Wigner phase-space distribution of a gaussian nuclear wavepackets given by equation (2.3). A derivation of this can be found in appendix B. The nuclear positions/velocities were then propagated using a velocity verlet algorithm and the adiabatic expansion coefficients were propagated using a 4<sup>th</sup> order Runge-Kutta method.

$$\chi(R, 0) = \frac{1}{(\pi\mu^2)^{\frac{1}{4}}} e^{-\frac{(R-R_0)^2}{2\mu^2} + ik_0(R-R_0)} \quad (2.3)$$

The adiabatic coefficients were initialised purely on the ground state and the initial width of the nuclear wavepacket was set to  $\mu = \sqrt{2}$  Bohr. This was chosen to replicate values found in the literature<sup>3</sup>. Two values of initial momenta  $k_0$  were chosen for each model, one low value and another higher one. Full details of all input parameters can be found in appendix A. I have implemented a serial version of CTMQC acting on Tully's toy model systems and real molecular systems using couplings derived from the analytic overlap method<sup>58</sup> within the software package CP2K<sup>80</sup> and for Tully's model systems as standalone python code. These are accessible publicly via github repositories at: [github.com/95ellismle](https://github.com/95ellismle). This work will only focus on results from the CP2K implementation as we will later see this code extended and applied to systems of real Ethylene molecules.

## 2.1 Testing the Ehrenfest Implementation

The motivation behind implementing CTMQC for the Tully models was to serve as a verifiable base for later extensions, such as integrating CTMQC within the fragment-orbital based (FOB)<sup>81</sup> framework which will be discussed in a later chapter 4.4. Using such simple systems will also help to clarify how each new parameter works and make testing and debugging easier. As well as many numerical tests on individual terms in the equations, I have implemented some physical tests on the overall system dynamics. In this section, I will outline the key tests I have performed on the Ehrenfest propagation and will include the full details of the full CTMQC propagation in the following section.

In all the simulations when the Tully models are referenced they will refer to those

parameters given in appendix A. Reference to a high momentum Tully model simulation is a reference to that model with initial momenta being sampled from the Wigner distribution of the higher of the two initial momenta given in appendix A.

### 2.1.1 Norm Conservation

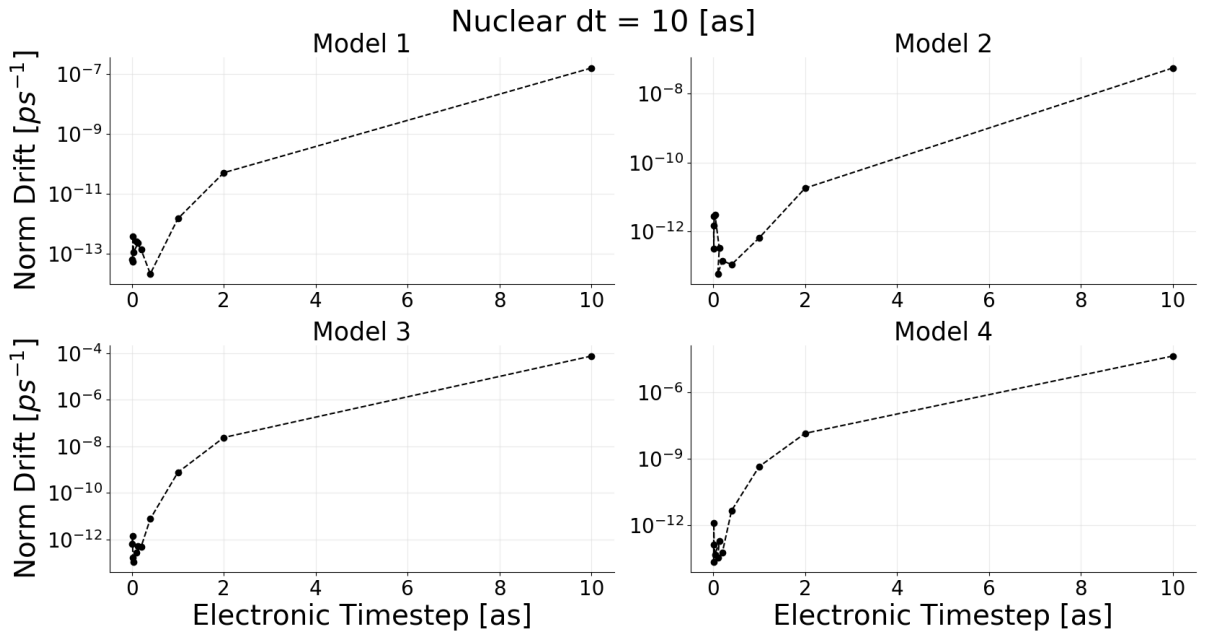


Figure 2.2: The norm conservation averaged over all replicas for Ehrenfest simulations with various electronic timesteps for each Tully model using a initial high momenta.

In appendix E, it is shown that the norm of the adiabatic expansion coefficients should be conserved throughout the simulation. To test the conservation of the norm of the expansion coefficients Ehrenfest simulations were run with various electronic timesteps (with a constant nuclear timestep) for each of the four high momentum Tully models. The high momentum Tully models were chosen as they are expected to provide a worst case scenario of the norm conservation, due to populations changing more quickly leading to reduced sampling. As can be seen in figure 2.2, the norm of the wavefunction is conserved within numerical error ( $10^{-12}$ ) when using a sufficiently small timestep in every Tully model.

### 2.1.2 Energy Conservation

Energy conservation is a very important property in most molecular dynamics simulations. In Ehrenfest or mean-field molecular dynamics nuclei are propagated on a population-

weighted mean potential energy surface, e.g.  $\sum_k |C_k^{(I)}(t)|^2 E_k = E_{eff}(t)$ <sup>82</sup>. Kinetic energy of the classical nuclei is given by the standard formula, i.e.  $\frac{1}{2}mv^2$ . We can therefore write down the conserved quantity as defined below in equation (2.4):

$$\frac{dE}{dt} = \frac{d}{dt} \left[ \frac{1}{2}mv^2 + \sum_k |C_k^{(I)}(t)|^2 E_k \right] = 0 \quad (2.4)$$

As in the norm conservation checks in section E, parameters from the high momentum cases were taken as initial conditions for simulations with various nuclear timesteps, this time holding the electronic timestep constant. The high momenta cases were chosen to show the worst case energy conservations. A linear line of best fit was then fitted to the data and the drift in the total energy (given in (2.4)) was calculated from its gradient. The results of these simulations are given in figure 2.3. In figure 2.3, we

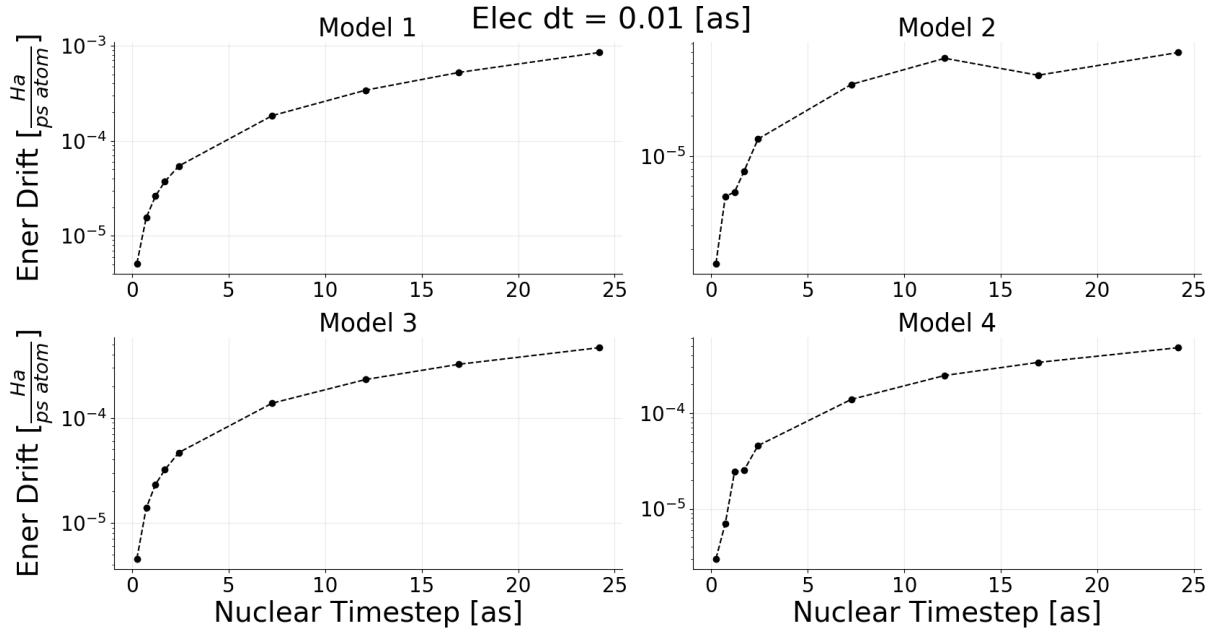


Figure 2.3: Energy conservation values for various nuclear timesteps for the high momentum case of each Tully model using Ehrenfest dynamics.

see the expected results that as the nuclear timestep is decreased the drift in the total energy also decreases. This is due to increased sampling of atomic movements leading to more continuous forces being calculated. This trend validates the implementation and shows that in the limit of infinitely small timestep (and infinite computer precision) perfect energy conservation would be achieved. However, fairly small nuclear timesteps are

required to achieve reasonable energy conservations. This is because the system contains only one atom with a mass comparable to that of Hydrogen. If one needed improved energy conservation a higher order integrator than the velocity verlet used here may also improve results slightly.

### 2.1.3 Comparisons To Literature

#### 2.1.3.1 Gossel and Agostini

There have been two papers published applying CTMQC and Ehrenfest to the Tully models<sup>2,3</sup> and both contain results for the 4 Tully models shown in fig 2.1. The results contain data on the (ground state) adiabatic populations and a coherence indicator (shown in equation (2.5)) for eight different simulations (a low and high initial momentum simulation of Models 1, 2, 3 and 4). However, models one and four in Agostini<sup>2</sup> used a different initial momentum so these have been omitted from the results in figures 2.4 and 2.5. The adiabatic populations give the probability of finding the wavefunction on a particular adiabatic state and their values can range from  $0 \rightarrow 1$ . A value of 1 means that the wavefunction is completely localised on one adiabatic state and there is a certainty of finding it there, a value of zero means that the wavefunction has zero probability of being found in that adiabatic state. The coherence indicator gives an indication of how much ‘mixing’ has occurred between adiabatic states and can have a value from  $0 \rightarrow 0.25$ . A value of 0 means that the adiabatic population has completely localised on just 1 state. A value of 0.25 means that the population is equally split between the 2 states.

$$|\rho_{12}(t)|^2 = \frac{1}{N_{tr}} \sum_{I=1}^{N_{tr}} |C_1^{(I)}(t)|^2 |C_2^{(I)}(t)|^2 \quad (2.5)$$

In order to compare to results in the literature the same setup had to be used. In this case this meant sampling individual replicas’ initial conditions (positions and momenta) from a Wigner distribution with a mean position and momentum given in appendix A. The wavefunction was initialised purely on the ground state and the same integrator was used for the nuclear and electronic propagation (velocity verlet and RK4 respectively).

My results as well as the relevant data taken from Agostini and Gossel<sup>2,3</sup> are shown

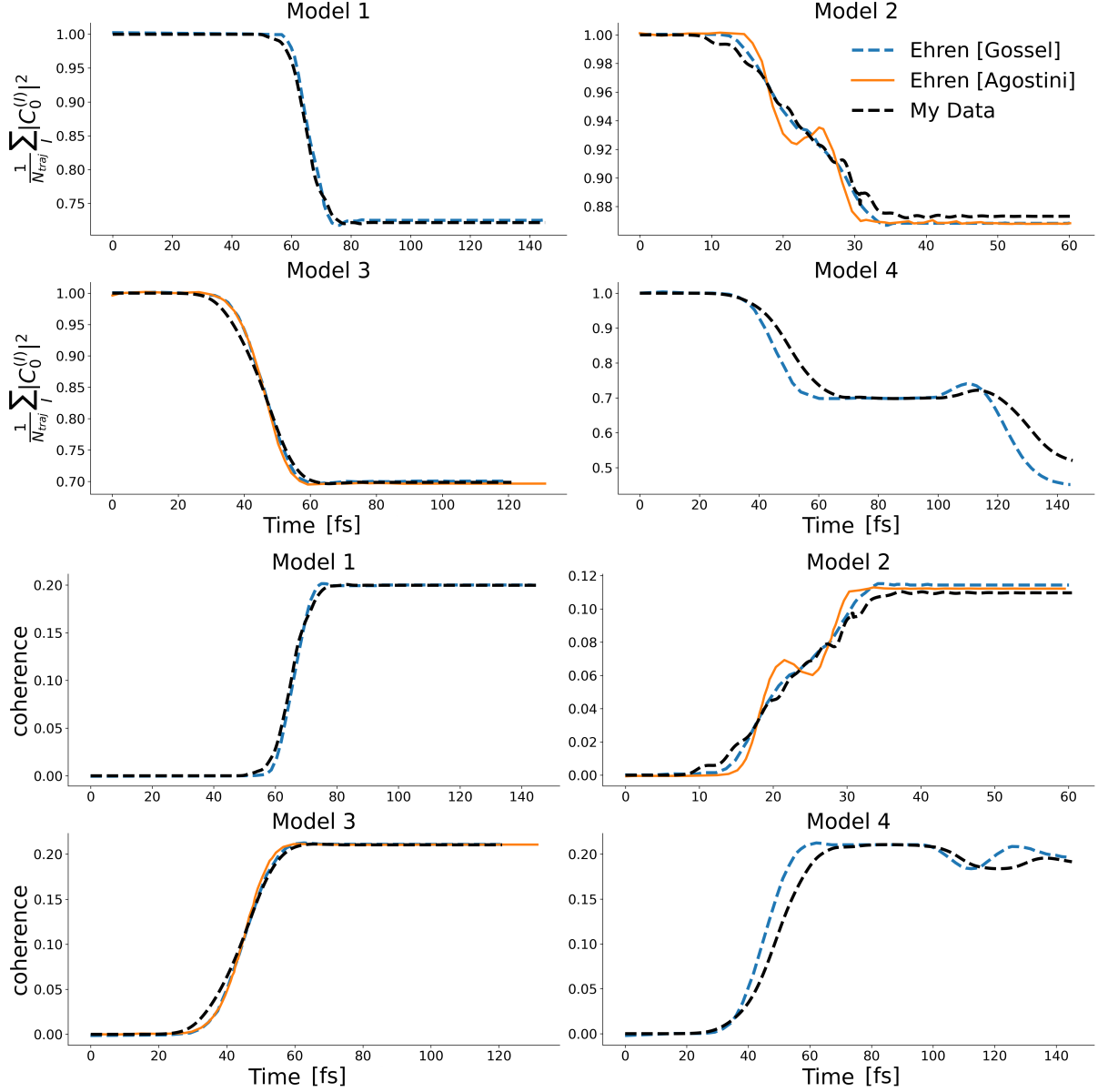


Figure 2.4: A comparison of my implementation of Ehrenfest (for 4 model Hamiltonians) and results from the literature for the low momenta cases. The black dashed lines show my data (ground state adiabatic populations), the orange dashed lines are data from Agostini<sup>2</sup> and the blue solid lines are from Gossel<sup>3</sup>. The figures are labelled with their model number, whether the initial momentum was high or low and whether the populations or coherence indicator was plotted.

in figures 2.4 (low momentum) and 2.5 (high momentum) for Ehrenfest dynamics. This is equivalent to full CTMQC dynamics where the quantum momentum term is set to 0. Hence, we can test most parts of the code (i.e. Runge-Kutta propagation, velocity

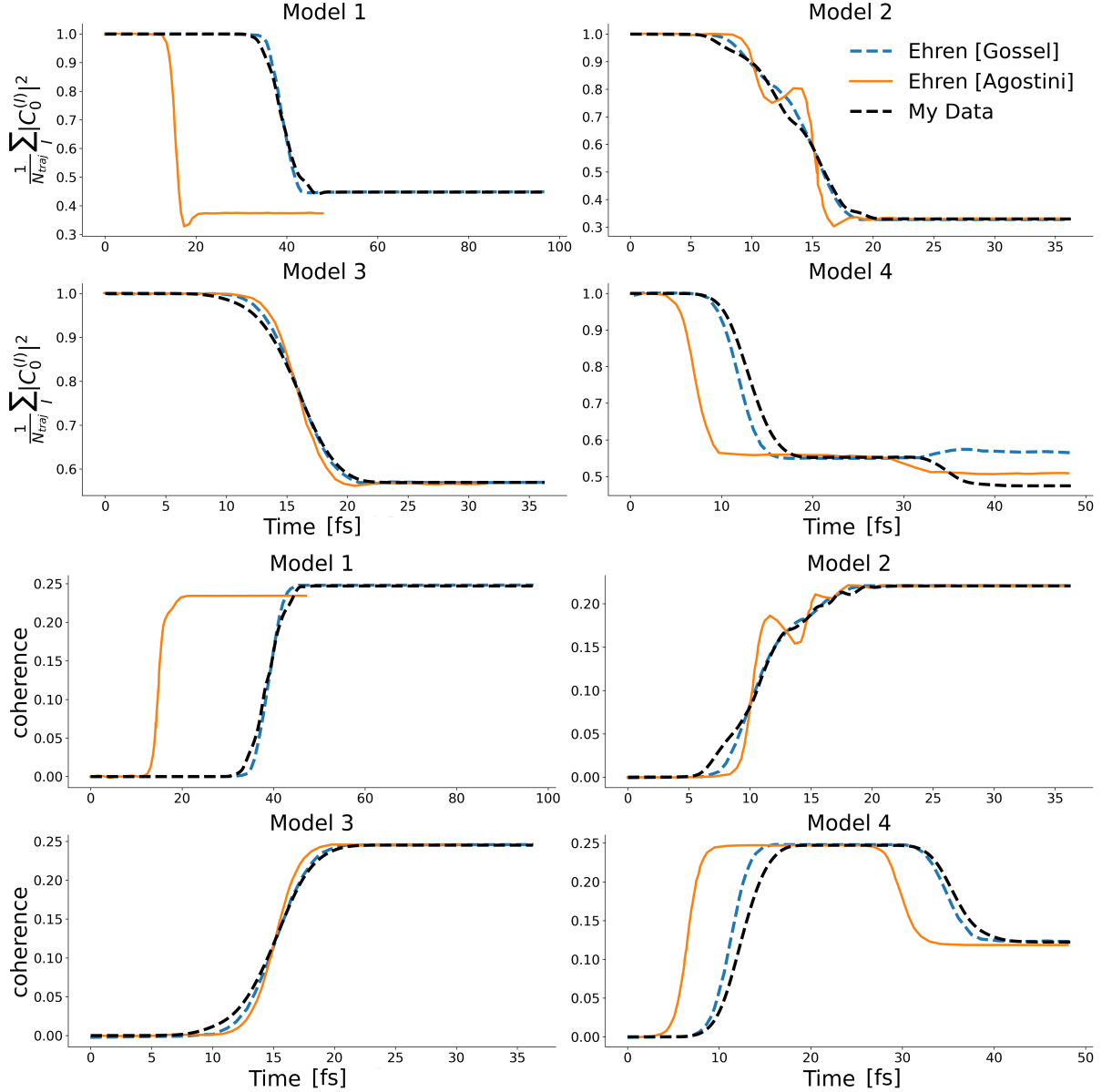


Figure 2.5: A comparison of my implementation of Ehrenfest (for 4 model Hamiltonians) and results from the literature for the high momenta cases. The black dashed lines show my data (ground state adiabatic populations), the orange dashed lines are data from Agostini<sup>2</sup> and the blue solid lines are from Gossel<sup>3</sup>. The figures are labelled with their model number, whether the initial momentum was high or low and whether the populations or coherence indicator was plotted.

verlet, inputs, force calculations etc...) while ignoring the new quantum momentum and accumulated adiabatic force terms.

The results in figures 2.4 and 2.5 show that both the adiabatic populations and co-

herence indicator give exactly the same results as in the literature, within reasonable error. That is my simulated data sits almost exactly on top of the literature results. Small discrepancies, especially at crossing points, come mainly from slightly different random sampling of the initial positions. The error in the model 4 adiabatic populations is on the same scale as the error in the 2 literature results. This is probably because the energy levels become almost degenerate at the end of this simulation and the adiabatic populations become very sensitive to initial conditions. Any deviations of results come from either a slightly different initial sampling of positions or small errors in extracting data from the graphs in each of the papers. For example, in the case of the high initial momentum simulation of model four all three results show some differences though the trend is very similar. This is true also in the Model 2 results where the Agostini populations show some transient oscillations before settling onto the same equilibrium population. This may be due to a smaller spread of positions being used in the initial sample leading to similar oscillations that aren't smoothed out in the averaging over all replicas. There are also a couple of models that start at a slightly different initial mean position in Agostini<sup>2</sup> thus they hit the nonadiabatic crossing region sooner. These are model one and four for the high momentum case.

Although not all results are exactly the same, I believe the populations agree well enough within a reasonable error to serve as a confirmation of my implementation.

### 2.1.3.2 Subotnik

As a final confirmation of my implementation and an investigation of the underlying physics, results were compared to those published by Subotnik<sup>83</sup> for Ehrenfest simulations carried out on the three original Tully Models. In this work, the author presented the probabilities of the population being found transmitted through the region of nonadiabatic coupling on the ground or excited state and the probability of being reflected on the ground or upper state. In the results below, I will show comparisons of just the transmission probability onto the ground state. That is, the population that travels on the ground state beyond the region of high nonadiabatic coupling. Other probabilities will not be shown in the interest of brevity, though they agree with the published results

as well as the ground state transmission in figure 2.6. As can be seen in figure 2.6 my

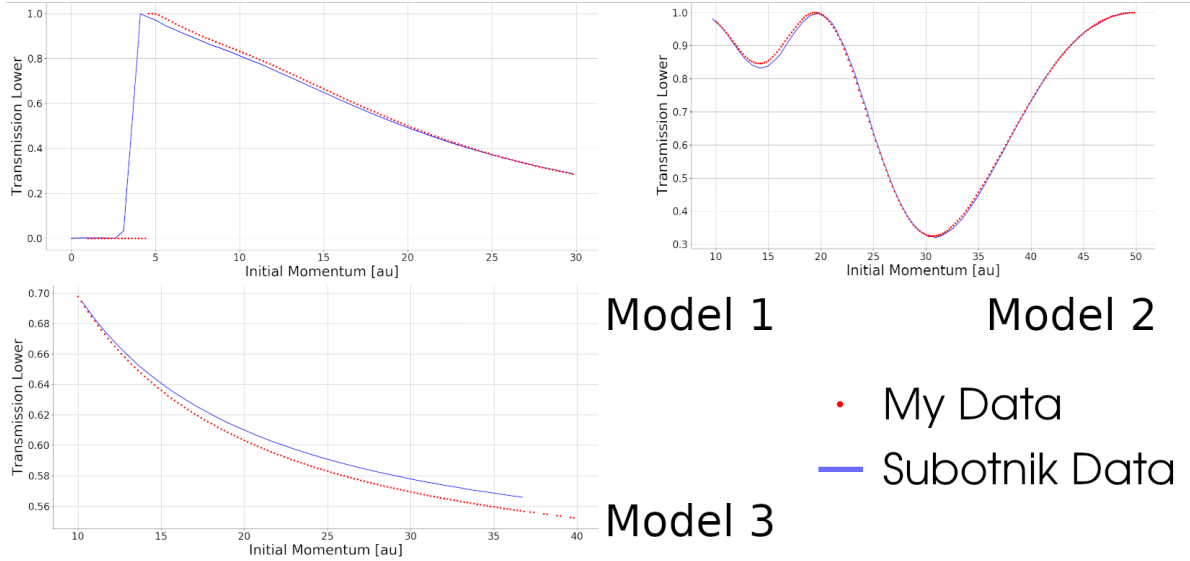


Figure 2.6: Comparison of transmission probabilities through the region of high nonadiabatic coupling on the ground state. Tully model one is shown in the top-left, Tully model two is shown in the top-right and Tully model three is shown in the bottom-left.

implementation of the Ehrenfest simulation code for the Tully models agrees very well with those in Subotnik<sup>83</sup>. The small deviation (less than 1% maximum disagreement) within each model is due to errors in retrieving data from images in original paper and possibly slightly different analysis methods. In model 1 (top-left pane) we see there is zero ground state population transmission below an initial momentum of around 3-4 au. This is due to the fact that the nuclei do not have enough kinetic energy to make it over the potential hill (see figure 2.1) and never reach an area of high nonadiabatic coupling. The sharp cutoff is due to the classical treatment of the nuclei. In the original Subotnik<sup>83</sup> paper exact results were given showing the slower decay to zero transmission with respect to initial momentum. Beyond this initial activation momentum, increases to initial momentum results in lower ground state transmissions. This is because the system has more kinetic energy allowing a higher proportion of the wavefunction to be transmitted on the excited state.

In model two we observe Stückelberg oscillations as the atom is forced through an avoided crossing twice. During the first pass through the avoided crossing some popu-

lation transfer onto the excited state occurs. In the next passage through the avoided crossing the wavefunction, now split over two energy levels and travelling coherently, can interfere with itself. The type of interference is dependent on the velocity of the particle passing through the avoided crossings and varies in an oscillatory fashion as seen in figure 2.6.

In model 3, as the particle approaches  $\mathbf{R} = 0$  it passes through a region of strong coupling, with a very small energy gap between energy levels. As the two energy levels diverge at  $\mathbf{R} = 0$  the nonadiabatic coupling dies down to zero and the population remains trapped on the energy level it was on at  $\mathbf{R} = 0$ . Increases in initial momentum of the particle increases the likelihood that we see the particle transmit on the excited state.

These tests serve as a confirmation of the implementation of the Ehrenfest propagator. The full CTMQC equations can be implemented using the majority of the Ehrenfest infrastructure with extensions to account for the quantum momentum terms.

## 2.2 Testing the CTMQC implementation

### 2.2.1 Conservation of the norm

In figure 2.7 only Model 3 shows a similar trend as in Ehrenfest for the norm conservation -i.e. a decreasing electronic timestep gives a rapidly decreasing norm drift. In models one and two we see that the norm drift doesn't get much better as we decrease the timestep and there are large error bars associated with each data point. In model four this is less pronounced but is still clearly affected. This is due to an instability in the current formalism of the quantum momentum term ( $\mathcal{Q}_{lk,v}^{(I)}$ ).

The calculation of the quantum momentum is discussed in detail in Min, 17<sup>78</sup> and outlined in the introduction to the thesis in section 1.5.2. As mentioned in that section, the denominator in the expression for  $\mathbf{R}_{lk,v}$  may be positive or negative and when it switches between each it can approach zero very closely. If this denominator approaches zero more quickly than the numerator then we can see large divergence in the  $\mathbf{R}_{lk,v}$  term

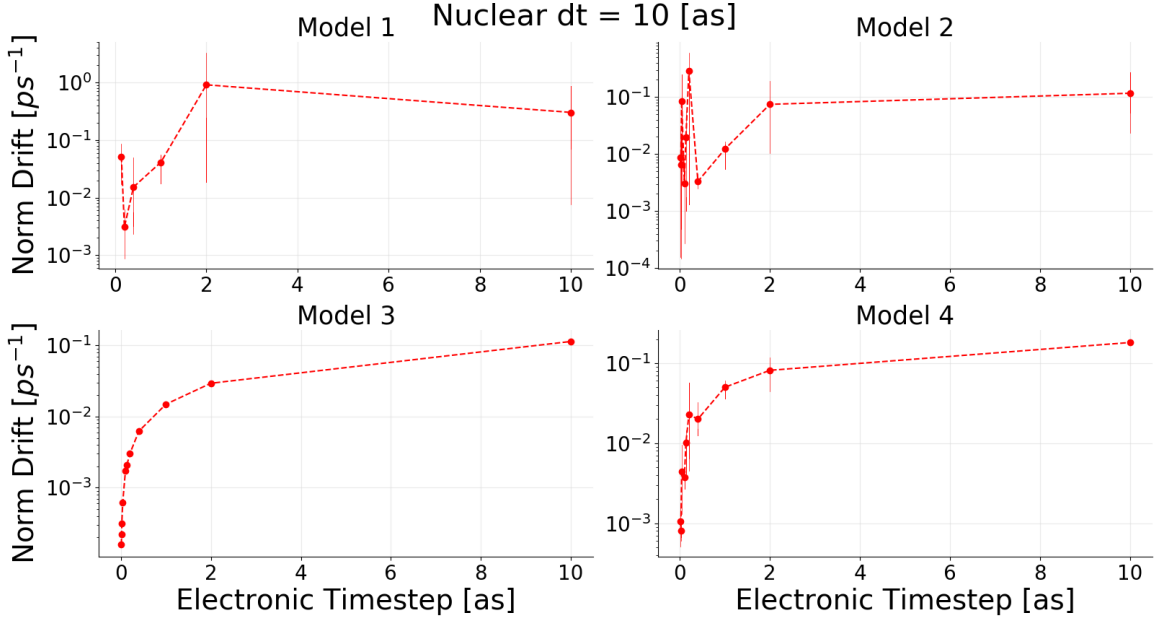


Figure 2.7: The norm conservation when using standard CTMQC as outlined in the literature for each of the Tully models. These simulations were ran with a high initial momentum. The red markers show data points and vertical bars show error bars associated with each point.

which can lead to large norm drifts. This is highlighted in figure 2.8.

### 2.2.1.1 Quantum Momentum Instabilities

In figure 2.8, as the denominator of quantum momentum intercept (the bottom panel) approaches zero the  $\mathbf{R}_{lk,v}$  term may spike causing a discontinuity in the populations (through the quantum momentum). The reason this only occurs in Models 1, 2 and four is due to the fact that the difference in the adiabatic momenta terms ( $\mathbf{f}_{l,v}^{(I)} - \mathbf{f}_{k,v}^{(I)}$ ) doesn't cross zero in Model 3 as the time-derivative of the adiabatic energies is always either positive or negative.

In order to correct for this divergence I have investigated a number of alterations to the calculation of the quantum momentum. These depend on the detection of the spikes/divergences in the  $\mathbf{R}_{lk,v}$  term and then the appropriate treatment of them. A divergence is recorded if two conditions are met. First is a simple threshold on the time-derivative of the intercept term, i.e.  $|\frac{d}{dt}\mathbf{R}_{lk,v}| > \text{thresh}$ . The second condition is a threshold on the intercept denominator i.e.  $|\mathbf{R}_{\text{denom},lk,v}| < \text{thresh}$ . For example, if the

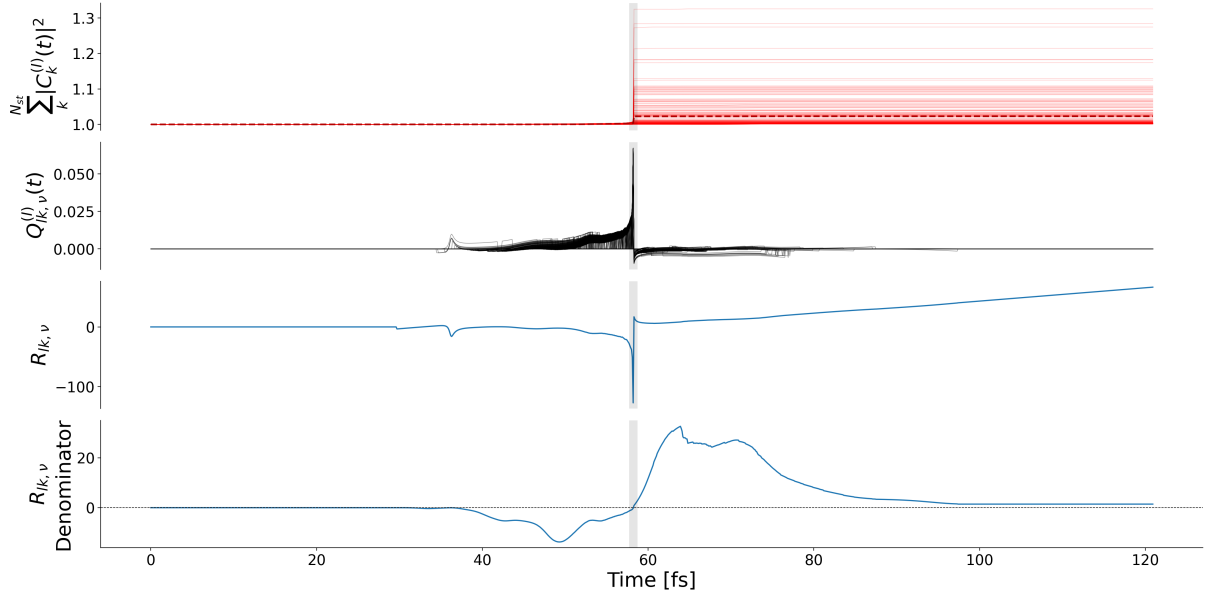


Figure 2.8: As the denominator of the  $\mathbf{R}_{lk,v}$  term approaches zero (bottom panel) the full  $\mathbf{R}_{lk,v}$  term (2<sup>nd</sup> to bottom panel) can approach infinity which propagates through the  $\mathcal{Q}_{lk,v}^{(I)}$  term (2<sup>nd</sup> to top panel) causing discontinuities and norm drift in the populations (top panel). The grey vertical bar denotes the region the denominator approaches 0. The thin solid red lines in the top panel show the norm drift for individual replicas.

absolute time-derivative of the  $\mathbf{R}_{lk,v}$  term is larger than a value (say 5) and the bottom of the fraction in equation (1.20) is within 0.01 of 0 then we assume the  $\mathbf{R}_{lk,v}$  term is diverging and the simulation code then uses a different method of propagating the electronic coefficients. The alternative propagation methods that have been investigated are:

1. Use Ehrenfest Dynamics (set e.g.  $\mathcal{Q}_{lk,v}$  term to 0).
2. Extrapolate the value of  $\mathbf{R}_{lk,v}$  from values before the divergence (see appendix C.1).
3. Switch to using the alternative intercept  $\mathbf{R}_{0,v}^{(I)}$  (see appendix C.2).

Of these three methods, method three was the most successful in reducing the norm drift in the Tully Models as can be seen in figure 2.9.

In figure 2.9 we see the norm drift results after the 3  $\mathbf{R}_{lk,v}$  correction methods have been applied. The red curve shows the original data (as in figure 2.7) with its large divergences in the norm drift. The green curve shows the alternative intercept method, the blue curve shows the effect of switching to Ehrenfest during the  $\mathcal{Q}_{lk,v}^{(I)}$  spikes and the black

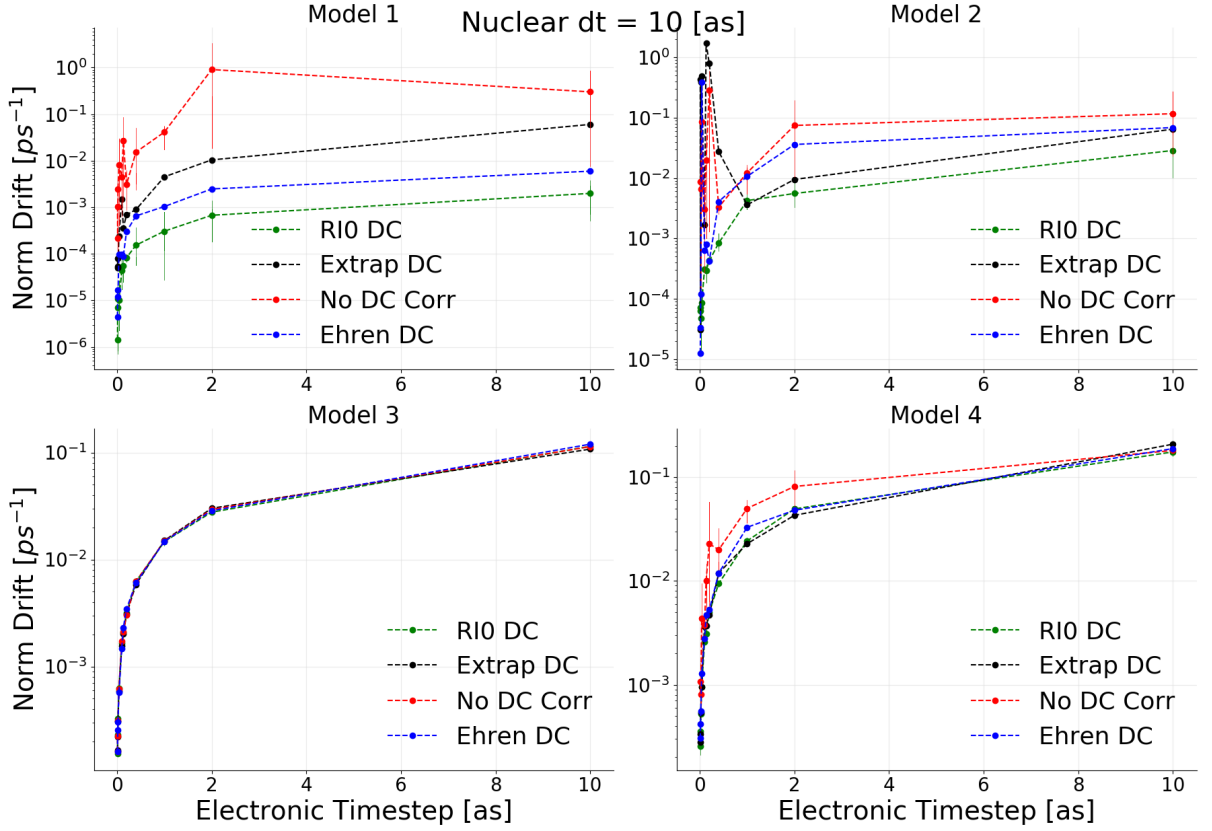


Figure 2.9: Norm conservation in CTMQC after applying a divergence correction to the  $\mathbf{R}_{lk,v}$  term. RI0 refers to method 3, Extrap DC refers to method two and Ehren DC refers to method 1. No DC Corr shows the population norm without any corrections applied.

shows a method that involved extrapolating the  $\mathbf{R}_{lk,v}$  value from data before the spike began. We can see clearly all three methods improve the norm drift, though using the alternative intercept seems to help the most. Model 3 is not affected as we do not see these divergences in the  $\mathbf{R}_{lk,v}$  due to the denominator in this particular model never crossing from positive to negative (through zero). It is important to note that in each of the models with the divergence correction applied all models exhibit the expected trend of decreasing the time-step improves norm conservation. However, norm conservation in all four models is still significantly higher ( $\sim 7\text{-}8$  orders of magnitude) higher than that of Ehrenfest. This is due to the product of the adiabatic populations,  $|C_l^{(I)}|^2 |C_k^{(I)}|^2$ , being used in the calculation of the quantum momentum. These can be a more quickly varying quantity than just the adiabatic populations alone -thus require a smaller timestep to adequately sample in a continuous way.

### 2.2.2 Mathematical Tests

Multiple tests of the implementation of the quantities in the equations have been implemented in the code to ensure correct outputs. A checklist of any mathematical tests is given below:

- Checking the (anti-)symmetry of the (NACV) Hamiltonian when constructed
- Comparing the adiabatic impulse term to post-production time-integrated adiabatic energies (using trapezium rule<sup>84</sup>)
- Checking special case solutions when all replicas are initialised at the same position such as:
  - $\mathcal{Q}_{lk,v}^{(I)} = 0$
  - CTMQC = Ehrenfest
- Checking special cases for when  $\sigma$  is replica independent (i.e.  $\sigma^{(I)} = \sigma_0$ ):
  - $\sigma = \frac{\hbar}{2\sigma_0^2}$
  - $\mathbf{R}_{lk,v} = \mathbf{R}_v^{(I)} \frac{\hbar}{2\sigma_0^2}$  (Assuming the positions,  $\mathbf{R}_v^{(I)}$  are also replica independent)
- If all adiabatic population is localised on a single state ( $|C_l^{(I)}|^2 = [1, 0, 0, \dots, 0]$ ) then we get Ehrenfest dynamics on that replica.
- Solving the static Schrödinger equation gives Rabi oscillations<sup>85</sup>. See appendix D.

I have also provided two more substantial mathematical tests for the code below in the following sections.

#### 2.2.2.1 Time Derivative of Replica-Sum of Adiabatic Populations

In the SI of Min, 17<sup>78</sup> a conservation equation (S27) is given. This is repeated below in equation (2.6)

$$\sum_I \mathcal{Q}_{lk,v}^{(I)}(t) \left( f_{k,v}^{(I)} - f_{l,v}^{(I)} \right) |C_k^{(I)}(t)|^2 |C_l^{(I)}(t)|^2 = 0 \quad \forall l, k, v \quad (2.6)$$

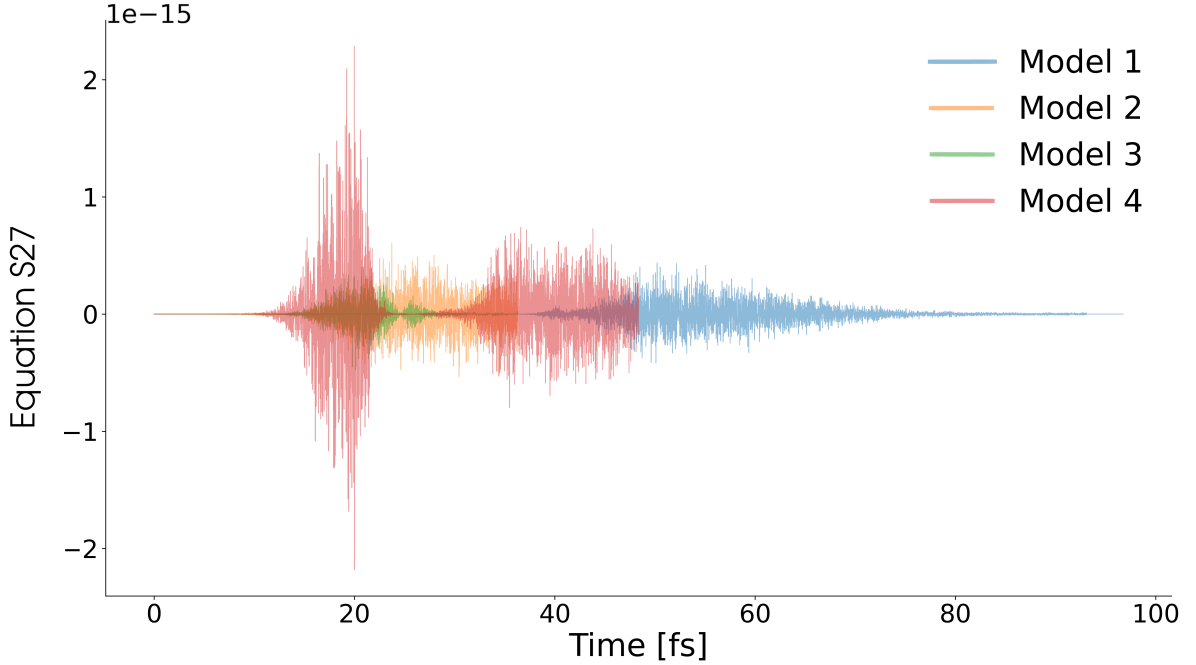


Figure 2.10: The conserved quantity given in equation (2.6) (y-axis). Each color represents data outputted by a simulation using a different model (specified in the legend). Each time-series is plotted with a translucent color meaning each model's data can be seen at once.

An example time-series of this quantity is given in figure 2.10 for each Tully model. The data for the calculations come from simulations of each of the Tully models using the parameters given in appendix A. No smoothing was used for the  $\mathbf{R}_{lk,v}^{(I)}$  term. It can be seen in this figure that the conservation quantity hovers around zero for each model with a maximum deviation of  $10^{-15}$  m<sub>e</sub>Ha.

### 2.2.2.2 Numerical Check of the Propagation Matrix

As the equations are currently formulated another numerical test validating the quantum momentum part of the propagation equations for the coefficients can be used. The CTMQC equation for the propagation of the adiabatic expansion coefficients is given in equation (1.15). The quantum momentum part of this equation is given below in equation (2.7).

$$\mathbb{X}_{qm,ll}^{(I)} = \sum_{v=1}^{N_n} \sum_k \frac{\mathcal{Q}_{lk,v}^{(I)}}{\hbar M_v} \cdot [\mathbf{f}_{k,v}^{(I)} - \mathbf{f}_{l,v}^{(I)}] |C_k^{(I)}|^2 \quad (2.7)$$

Where  $\mathbb{X}_{qm,ll}^{(I)}$  is the diagonal matrix that, when multiplied with the adiabatic expansion coefficients, gives the quantum momentum contribution to the propagation of the expansion coefficients.

We can test the construction of this matrix within the code by multiplying by the adiabatic populations and summing as shown in equation (2.8). It can be shown, assuming perfect norm conservation, that this should equal exactly 0. This is due to the symmetry of the  $|C_l^{(I)}|^2|C_k^{(I)}|^2$  and the quantum momentum matrix. This is checked for every timestep during propagation.

$$\sum_l \mathbb{X}_{qm,ll}^{(I)} |C_l^{(I)}|^2 = 0 \quad (2.8)$$

### 2.2.3 Energy Conservation

In Agostini<sup>2</sup> it is stated that the approximate potential energy is given by the same equation as in Ehrenfest, i.e. equation (2.4) a population weighted average of the potential energy surfaces. The 4 high momentum Tully models were simulated with various nuclear timesteps and a straight line of best fit was fitted to the total energy term.

As can be seen in figure 2.11 the energy conservation in CTMQC does not improve with a decreasing nuclear timestep. In fact in the energy conservation worsens with decreasing nuclear timestep in some models such as model 4. Additionally, in models two and four the errorbar increases as the timestep decreases. This is caused by an increased likelihood of coming across a divergence in the quantum momentum that can't be properly corrected, due to more steps being simulated. In model 3, the error bar stays the fairly consistent, and the energy conservation doesn't change with respect to the timestep. In this model there are no quantum momentum divergences which means the poor energy conservation is caused by something else. The potential energy as given in Agostini<sup>2</sup> is an approximation and to achieve energy conservation comparable to Ehrenfest this may need amending.

### 2.2.4 Comparisons to literature

As in section 2.1.3.1 we can compare the CTMQC results to those published before in Gossel<sup>3</sup> and Agostini<sup>2</sup>. These results are given in figures 2.12 and 2.13. This time, unlike

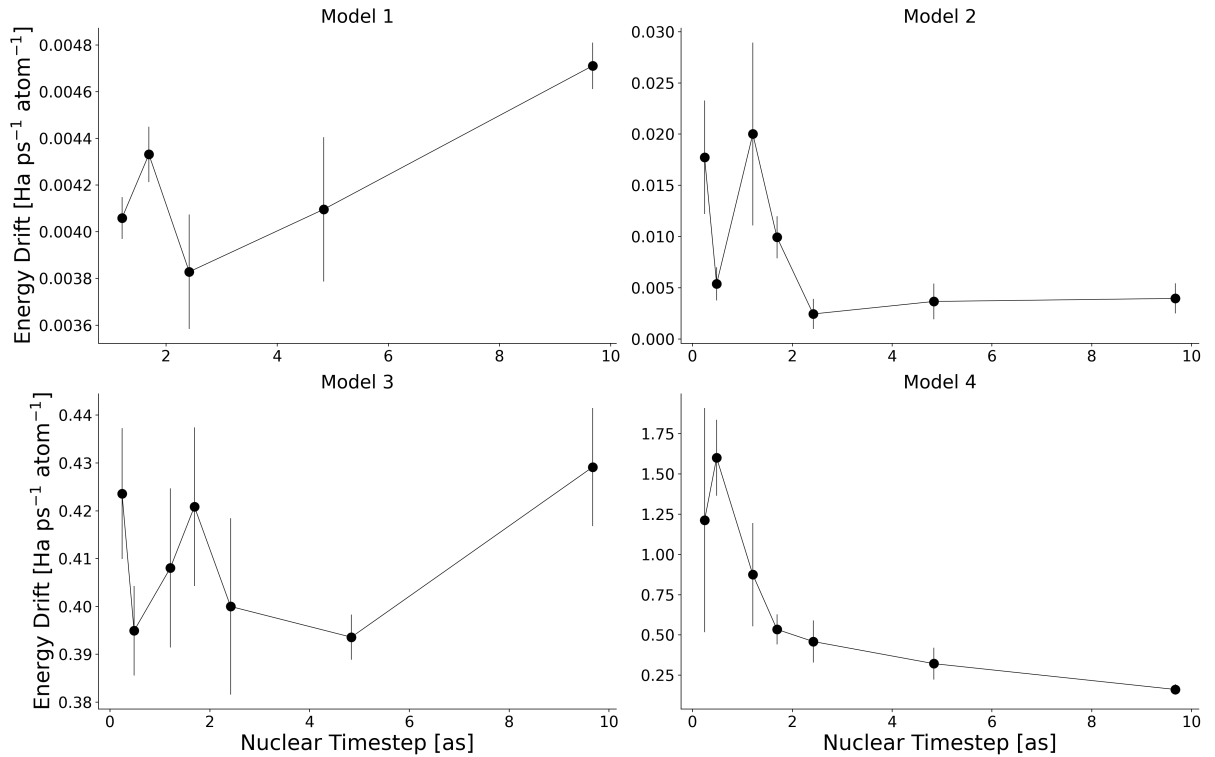


Figure 2.11: Energy drift in the 4 Tully models using the full CTMQC equations. Error bars are from multiple simulations carried out with different random sampling of the initial positions and momenta.

in the Ehrenfest code, we see some discrepancies between the three results which cannot solely be explained as small errors from different sampling of initial positions or from errors in extracting data from graphs in the papers. We can see that the errors mainly appear in the coherence indicator, looking at the bottom row in figures 2.12 and 2.13 it appears that both the Agostini and Gossel results match mine (dashed black line) very closely. The largest difference is seen in model 4, high momentum where the Gossel data and mine follow a similar trend and the Agostini data follows the exact curve more closely. The reason for this is a difference in the way the adiabatic momenta terms are handled. In the Gossel paper, a method to reset the adiabatic momenta to zero for each replica when the adiabatic populations collapse onto a pure adiabatic state (within a tolerance) is used. If this resetting is turned off then the populations in model four follow the Agostini results exactly. While resetting the adiabatic momenta worsens the calculation of the adiabatic populations in the model four simulations, it improves the convergence of the coherence indicator in the model 2 simulations. I will show later how

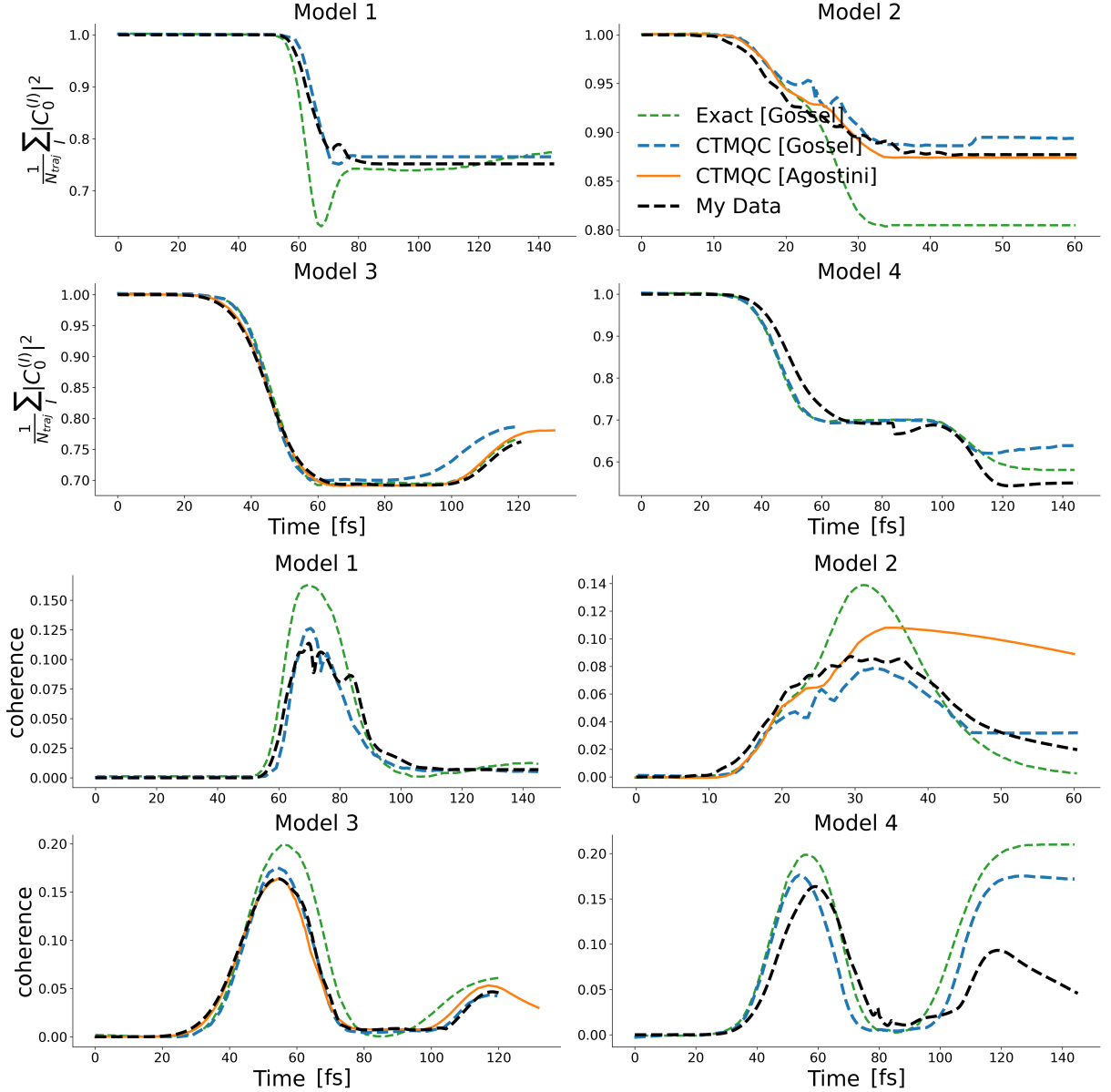


Figure 2.12: A comparison of my implementation of full CTMQC (for 4 model Hamiltonians) and results from the literature for the low momentum cases. The black dashed lines show my CTMQC data (ground state adiabatic populations), the orange dashed lines are data from Agostini<sup>2</sup> and the blue solid lines are from Gossel<sup>3</sup>. The solid green line shows data from exact quantum mechanical simulations given in Gossel. The figures are labelled with their model number, whether the initial momentum was high or low and whether the populations or coherence indicator was plotted.

using a method to dynamically alter the gaussian width parameter, used to calculate the quantum momentum, can improve the model four results markedly. Other deviations in results for the populations are due to a slightly different sampling of initial positions, a different handling of divergences in the quantum momentum term and constructing the

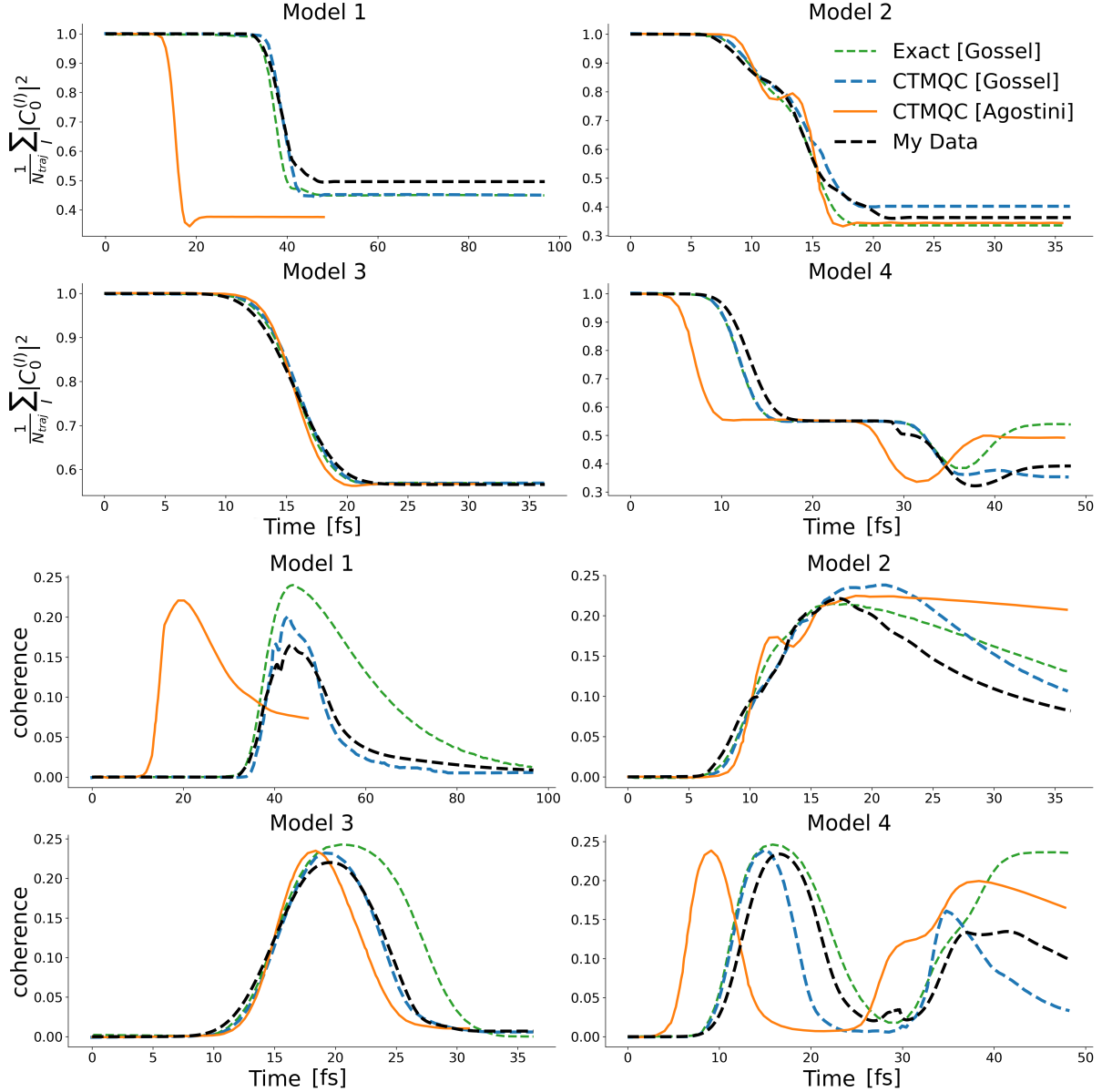


Figure 2.13: A comparison of my implementation of full CTMQC (for 4 model Hamiltonians) and results from the literature for the high momentum cases. The black dashed lines show my CTMQC data (ground state adiabatic populations), the orange dashed lines are data from Agostini<sup>2</sup> and the blue solid lines are from Gossel<sup>3</sup>. The solid green line shows data from exact quantum mechanical simulations given in Gossel. The figures are labelled with their model number, whether the initial momentum was high or low and whether the populations or coherence indicator was plotted.

$\mathcal{Q}_{lk,v}^{(I)}$  term with a different width parameter ( $\sigma$ ), which isn't specified in each of the paper the results have been taken from. The differences in my results and those given in the literature are on the same scale as the differences already presented in the literature and they are not large enough to invalidate my implementation. The discrepancies present

between the results in the papers presented here are probably caused by the same small algorithmic differences causing minor discrepancies in my results. The fact many of the literature results agree exactly with my implementation can be taken as a confirmation that my implementation is working well.

## 2.3 Construction of the quantum momentum

In order to calculate the quantum momentum the nuclear density must be constructed from the nuclear positions. However, the nuclei are treated classically, i.e. as point particles. To approximate the nuclear density from atomic positions a normal distribution is placed with the mean at the position of each particle with a width of  $\sigma$  and combined. This method is outlined in the supplementary information in Min, 17<sup>78</sup> and introduces a new parameter which must be tuned in order to reproduce sensible results. If the width is too small the resulting nuclear density is too noisy and the quantum momentum values unreliable. If the width is too large the nuclear density is very smooth with little variation and the quantum momentum values become very small. Seeing as the quantum momentum is one of the most important factors affecting coherence between electronic states the careful selection of the  $\sigma$  parameter is important. This issue is not very well addressed in the literature. In this section I will show results of calculation carried out with various constant values of  $\sigma$  as well as a method for a dynamic calculation of  $\sigma_v^{(I)}(t)$  on the fly. In figures 2.12 and 2.13 a constant value of 0.35 was used in order to best reproduce the results in Gossel<sup>3</sup>.

### 2.3.1 Constant Values of $\sigma$

The simplest option for the calculation of  $\mathcal{D}_{lk,v}^{(I)}$  is to keep the gaussian width parameter,  $\sigma$ , constant throughout the simulation. This also allows us to investigate the role of  $\sigma$  within the simulations and to determine its influence on the dynamics. To this end various simulations were carried out on the 4 Tully models with the high initial momentum. In each simulation parameters were all the same apart from the value of  $\sigma$  which took a value of either: 0.1, 0.2, 0.3, 0.5, 0.6, 0.75, 1 or 2 Bohr. The results for these simulations are shown in figure 2.14. In this figure, we see that as the  $\sigma$  parameter is increased the levels of decoherence also increases. This means for larger  $\sigma$  values electronic populations remain

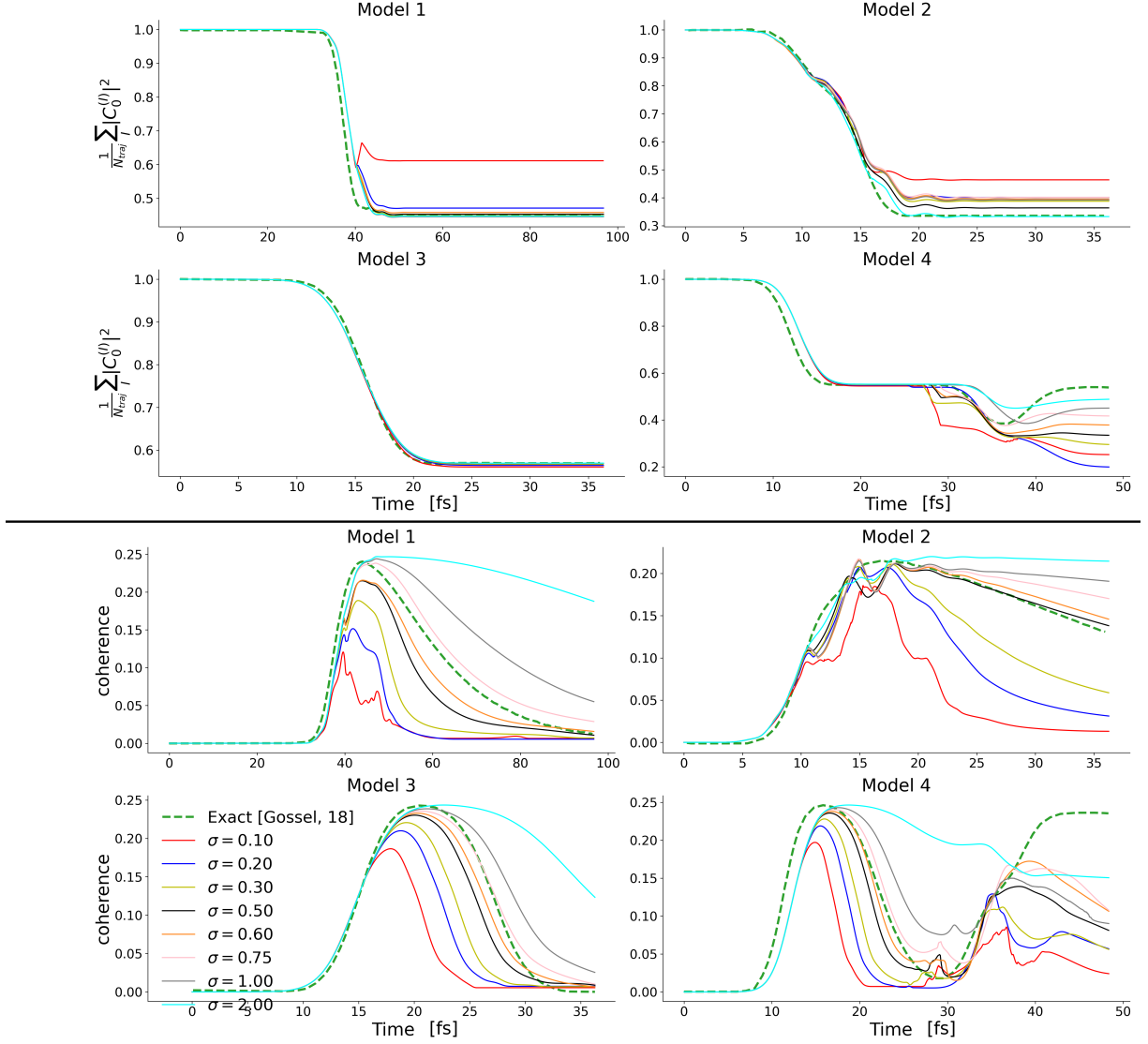


Figure 2.14: 4 high momenta cases of the Tully models with a various constant  $\sigma$  values used in the calculation of the quantum momentum. Thin solid lines show results from my simulations. The thick, green, dashed line shows data from exact quantum dynamics simulations taken from Gossel<sup>3</sup> which should be taken as a reference.

in a mixed state for longer and take more time to collapse onto a single adiabatic state. Clearly, the construction of this  $\sigma$  parameter is important for recovery of correct electronic dynamics. Surprisingly, this doesn't seem to have much of an effect on the resulting populations. However, this is due to the fact in the limit of large  $\sigma$  CTMQC becomes identical to Ehrenfest dynamics and Ehrenfest dynamics captures the evolution of the adiabatic populations very well for each model, with the exception of model 4. It should also be noted that for small values of  $\sigma$ , propagation using CTMQC can become unstable

due to a noisy nuclear density giving rise to an unstable quantum momentum term. A value of 0.6 Bohr qualitatively seems to provide the best fit to exact data. However, this may not be appropriate for all types of simulations and a deeper investigation into this parameter would be useful to investigate how general this finding is.

### 2.3.2 Dynamic $\sigma_v^{(I)}(t)$ calculation

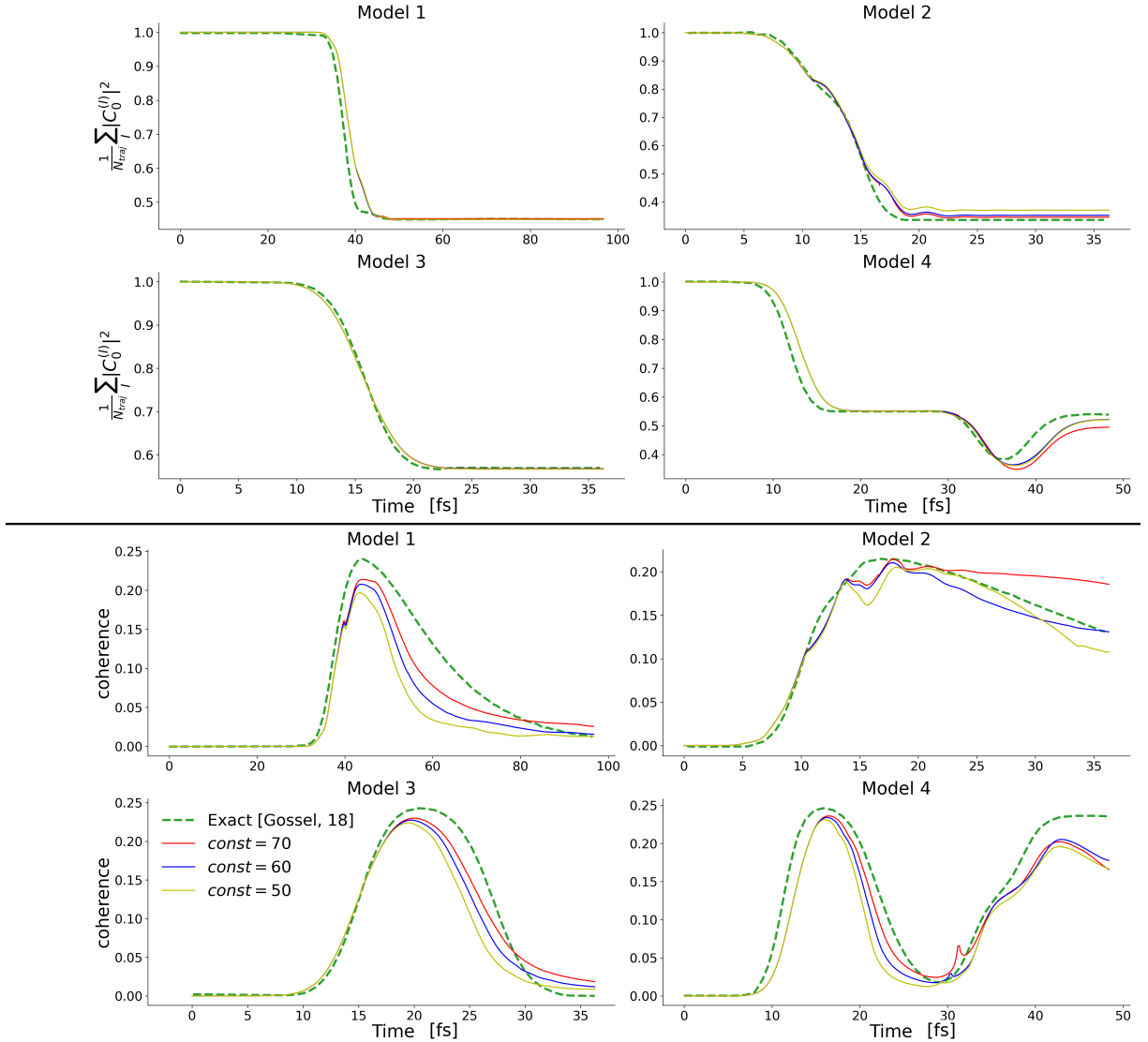


Figure 2.15: Four high momentum cases of the Tully models with a dynamic calculation of sigma using various values for const.

In the appendix of Gossel<sup>3</sup> an algorithm was outlined to calculate  $\sigma$  on-the-fly based on the density of replicas within a cutoff distance of each atom. This is given in appendix F. However, this method also relies on a constant parameter to calculate  $\sigma$  so doesn't

remove a parameter, though the resulting dynamics do not seem as sensitive to changes in this parameter as in  $\sigma$  itself.

Figure 2.15 shows populations and coherences for the 4 (high momentum) Tully models with various values of const. It is encouraging to see populations now resemble exact results more closely. This is especially true in model 4, where the dip in the populations is recovered. All 3 constants give nearly identical populations, though a constant of 60 seems to give results that most closely resemble the exact coherences. However, seeing as this (like the width parameter) is not a physical parameter it is hard to know if this is reasonable for all systems.

## 2.4 Conclusion

In this chapter I have reported results from my implementation of the CTMQC equations applied to the Tully models. The Tully models are a set of 4 Hamiltonians dictating the motion of one atom in 1 dimension. These models are commonly simulated as they are simple enough to be solved analytically and complex enough to provide a reasonable test for any new nonadiabatic molecular dynamics (NAMD) technique. I have shown results from various tests which validate my implementation and shown how well CT-MQC conserves the norm of the wavefunction and total energy, with the latter showing some concerning results. The reason for this is still unknown. I have also highlighted two issues with the dynamics in CTMQC. These are the sudden divergences in the quantum momentum term and the ambiguity surrounding the calculation of the gaussian width parameter,  $\sigma$ . The former issue has not been discussed in the literature though I have given a method designed to address it. This has been shown to significantly improve the norm conservation in the Tully model systems. The latter problem has been touched upon in the literature, though no thorough studies have been reported. I have given results for a various values of the gaussian width parameter,  $\sigma$ , and shown how it can affect the propagation dynamics. Further, I have implemented a method designed to dynamically update the  $\sigma$  parameter and benchmarked this against exact quantum dynamics simulations.

The propagation of the CTMQC equations using a model Hamiltonian is a good first step in implementing a new NAMD technique. Its relative simplicity allows for a close inspection of each of the quantities involved in the propagation, especially new quantities such as the adiabatic impulse term,  $\mathbf{f}_{l,v}^{(I)}$  and the quantum momentum term,  $\mathcal{Q}_{lk,v}^{(I)}$ . The same code used to simulate the Tully model system can also be used as a base for future extensions such as in 3D or many atom systems. However, before such extensions are implemented a new way to construct the Hamiltonian is needed. In the next chapter I will discuss my implementation of CTMQC within the fragment orbital based framework which relies on the fast calculation of the Hamiltonian using a finite difference method for off-diagonals and a classical force-field to calculate diagonal terms.

## Chapter 3

# CTMQC applied to molecular systems

In order to apply CTMQC to large molecular systems (hundreds of molecules) a different way to construct the Hamiltonian is needed. In this work I have implemented the CTMQC equations within the fragment-orbital based framework. This relies on the equations being expressed in a pseudo-diabatic basis and the Hamiltonian being constructed in two parts: the diagonal elements (site energies) and the off-diagonals (electronic couplings). The basis is termed ‘pseudo-diabatic’ due to the fact that non-adiabatic coupling vectors are small but non vanishing, this results in a basis where the excess charge carrier is strongly but not strictly localised on a single molecule. Within the Hamiltonian, the site energies (diagonal elements) are calculated via classical force-fields and the electronic couplings (off-diagonals) are calculated via the analytic overlap method<sup>58,81</sup> (AOM). In this method the coupling elements are assumed to be proportional to the overlap between the highest singly occupied molecular orbitals (SOMO) on the donor and acceptor molecules (see equation (3.1)). This approximation is often used in the literature, e.g. in the fragment orbital density functional theory<sup>86–88</sup> (FODFT) method and has been shown to be valid for many  $\pi$ -conjugated molecules<sup>58,89</sup>.

$$H_{ab} = C\langle \varphi_a | \varphi_b \rangle = CS_{ab} \quad (3.1)$$

Where  $\varphi_{a(b)}$  represents a singly occupied molecular orbital on the donor (acceptor) and  $C$  is the scaling constant and comes from DFT parameterisation. The singly occupied molecular orbitals are calculated as a linear combination of Slater-type orbitals (STO)

as in equation (3.2). In this equation we loop over each atom in the molecule and sum the size of the contribution,  $c_{p\pi,i}$ , multiplied by the STO,  $p_{\pi,j}$ . In this case the STO is represented by a p-orbital. The size of the p-orbital on each atom,  $c_{p\pi,i}$ , is parameterised before the simulation with DFT.

$$|\varphi_{mol}\rangle = \sum_{i \in mol}^{N_{atoms}} c_{p\pi,i} |p_{\pi,i}\rangle \quad (3.2)$$

Importantly, the AOM method offers a very fast way to calculate the off-diagonal elements of the Hamiltonian via a finite-difference method with an accuracy comparable to that of DFT methods<sup>90</sup>. This has been implemented within an open-source software package named CP2K and is used by a fragment-orbital based surface hopping technique to study large systems of hundreds of molecules. In the next chapter, the surface hopping technique will be discussed in further detail and applied to a system of pentacene molecules in order to investigate charge carrier (hole) transfer within amorphous systems.

### 3.1 Basis Transformation

In order to use the FOB method, as stated above, the CTMQC equations in the adiabatic basis must be transformed to the diabatic basis. In the following derivation  $C_l$  will represent the adiabatic expansion coefficient corresponding to state l and  $u_l$  will represent the orthogonal diabatic expansion coefficients.

The CTMQC equations in the adiabatic basis are given below in equation (3.3) of the forces and (3.4) coefficients:

$$\begin{aligned} \mathbf{F}_v^{(I)} = & - \sum_k |C_k^{(I)}|^2 \nabla_v E_k^{(I)} - \sum_{k,l} C_l^{*(I)} C_k^{(I)} \left( E_k^{(I)} - E_l^{(I)} \right) \mathbf{d}_{v,lk}^{ad,(I)} \\ & - \sum_{l,k} |C_l^{(I)}|^2 \left( \sum_{v'}^{N_n} \frac{2}{\hbar M_{v'}} \mathcal{D}_{v',lk}^{(I)} \cdot \mathbf{f}_{l,v'}^{(I)} \right) [\mathbf{f}_{k,v}^{(I)} - \mathbf{f}_{l,v}^{(I)}] |C_k^{(I)}|^2 \end{aligned} \quad (3.3)$$

$$\begin{aligned}\dot{C}_l^{(I)} = & -\frac{i}{\hbar} E_l^{(I)} C_l^{(I)} - \sum_k C_k^{(I)} \sum_{v=1}^{N_n} \frac{\mathbf{P}_v^{(I)}}{M_v} \cdot \mathbf{d}_{v,lk}^{ad,(I)} \\ & - \sum_{v=1}^{N_n} \sum_k \frac{\mathcal{Q}_{v,lk}^{(I)}}{\hbar M_{v'}} \cdot [\mathbf{f}_{k,v}^{(I)} - \mathbf{f}_{l,v}^{(I)}] |C_k^{(I)}|^2 C_l^{(I)}\end{aligned}\quad (3.4)$$

Where:

- $E_l^{(I)}$  is the adiabatic energy for state l and trajectory I
- $C_k^{(I)}$  is the adiabatic expansion coefficient for state k and trajectory I
- $\mathbf{P}_v^{(I)}$  is the classical momentum of atom  $v$  on trajectory  $I$
- $\mathbf{d}_{v,lk}^{ad,(I)}$  is the nonadiabatic coupling vector (given in the adiabatic basis)
- $M_v$  is the mass of nucleus  $v$
- $\mathcal{Q}_{v,lk}^{(I)}$  is the quantum momentum vector for atom  $v$  corresponding to the  $lk$  pair of states in trajectory  $I$
- $\mathbf{f}_{l,v}^{(I)}$  is the adiabatic impulse on state l, atom  $v$  and trajectory  $I$

### 3.1.1 Coefficients

To transform the equation for the propagation of the coefficients it is far neater to use the matrix notation as in equation (3.5) below:

$$\dot{\mathbf{C}}^{(I)} = \mathbb{X}_v^{(I)} \mathbf{C}^{(I)} = \left( \mathbb{X}_{eh,v}^{(I)} + \mathbb{X}_{qm,v}^{(I)} \right) \mathbf{C}^{(I)} \quad (3.5)$$

Where the  $\mathbb{X}$  matrices are defined as in equations (3.6) and (3.7) below.

$$\mathbb{X}_{lk,v}^{eh(I)} = -\frac{i}{\hbar} E_l^{(I)} - \sum_v \frac{\mathbf{P}_v^{(I)}}{M_v} \cdot d_{lk,v}^{ad,(I)} \quad (3.6)$$

$$\mathbb{X}_{ll,v}^{qm(I)} = - \sum_{v=1}^{N_n} \sum_k \frac{\mathcal{Q}_{v,lk}^{(I)}}{\hbar M_{v'}} \cdot [\mathbf{f}_{k,v}^{(I)} - \mathbf{f}_{l,v}^{(I)}] |C_k^{(I)}|^2 \quad (3.7)$$

The subscript  $ll$  in equation (3.7) indicate that these values occur only along the diagonal of the matrix  $\mathbb{X}^{qm(I)}$

Using the identities:

$$\mathbb{U}^{-1} = \mathbb{U}^\dagger \quad (3.8)$$

$$\mathbf{C}^{(I)} = \mathbb{U}^{\dagger(I)} \mathbf{u}^{(I)} \quad (3.9)$$

$$\dot{\mathbf{C}}^{(I)} = \mathbb{U}^{\dot{\dagger}(I)} \mathbf{u}^{(I)} + \mathbb{U}^{\dagger(I)} \dot{\mathbf{u}}^{(I)} \quad (3.10)$$

Where  $\mathbb{U}^{(I)} = \langle \phi_l^{(I)} | \psi_n^{(I)} \rangle$  is the unitary transformation matrix transforming from the diabatic to adiabatic basis. The  $\mathbf{u}^{(I)}$  terms are the diabatic expansion coefficients on trajectory I.

After some algebra we arrive at:

$$\dot{\mathbf{u}}^{(I)} = \underbrace{\left( \mathbb{U}^{(I)} \mathbb{X}_{eh} \mathbb{U}^{\dagger(I)} + \mathbb{U}^{(I)} \mathbb{U}^{\dagger(I)} \right) \mathbf{u}^{(I)}}_{\text{Ehrenfest}} + \underbrace{\left( \mathbb{U}^{(I)} \mathbb{X}_{qm} \mathbb{U}^{\dagger(I)} \right) \mathbf{u}^{(I)}}_{\text{Quantum Momentum}} \quad (3.11)$$

In equation (3.11) I've separated the contribution from Ehrenfest and the contribution from the new quantum momentum terms. The Ehrenfest part can be shown to reduce to a simpler form (see Spencer, 2016<sup>81</sup> and Carof, 17<sup>91</sup> for more details). The quantum momentum term must be coded up as shown with the transformation matrices. This gives the final equation for the propagation of the diabatic expansion coefficients, shown in equation (3.12).

$$\dot{\mathbf{u}}^{(I)} = \left( -\frac{i}{\hbar} \mathbb{H}^{(I)} - \mathbb{D}_{diab}^{(I)} \right) \mathbf{u}^{(I)} + \left( \mathbb{U}^{(I)} \mathbb{X}_{qm} \mathbb{U}^{(I)\dagger} \right) \mathbf{u}^{(I)} \quad (3.12)$$

Where  $\mathbb{H}^{(I)}$  is the diabatic Hamiltonian constructed via the AOM method,  $\mathbb{D}_{diab}^{(I)}$  are the diabatic nonadiabatic coupling elements ( $d_{diab,lk}^{(I)} = \langle \phi_l | \dot{\phi}_k \rangle$ ).

### 3.1.2 Forces

A full derivation of the transformation of basis for the equation propagating forces is given in appendix G. The result is given in equation (3.13) below:

$$\begin{aligned} \mathbf{F}_{eh,v}^{(I)} = & \sum_{i,j} \mathbf{u}_i^{*(I)} \mathbf{u}_j^{(I)} \left( \nabla_v H_{ij}^{(I)} + \sum_l \mathbf{d}_{lk,v}^{(I)} H_{lj}^{(I)} - \sum_l \mathbf{d}_{lj,v}^{(I)} H_{il} \right) \\ & - \sum_{l,k} |C_l^{(I)}|^2 \left( \sum_{v'}^{N_n} \frac{2}{\hbar M_{v'}} \mathcal{Q}_{v',lk}^{(I)} \cdot \mathbf{f}_{l,v'}^{(I)} \right) [\mathbf{f}_{k,v}^{(I)} - \mathbf{f}_{l,v}^{(I)}] |C_k^{(I)}|^2 \end{aligned} \quad (3.13)$$

Where the definitions of the terms within equation (3.13) have been explained previously. There are a couple of things to note with this equation. Firstly, (as in the coefficients equation) the quantum momentum part has not been transformed. This is because the forces are basis independent and don't need to be transformed. Secondly, the quantities required for the calculation of this part of the equation are already calculated in order to propagate the coefficients so only a small amount of extra effort is required to calculate the quantum momentum force term. The Ehrenfest part of the equation has been transformed. This is because the nonadiabatic coupling vectors within the adiabatic basis are never required so are never calculated. The Ehrenfest force term requires these nonadiabatic coupling vectors so would add an extra computational overhead. Further, the commutator term in the diabatic basis has been observed to provide a negligible contribution to the overall force in previous simulations (not shown in this work). This term requires significant computational effort and can be neglected. This makes the calculation of the Ehrenfest forces in the diabatic basis far cheaper than in the adiabatic basis.

## 3.2 Testing the diabatic propagator

The diabatic propagation can be tested against the already tested adiabatic propagator using the Tully model Hamiltonian. The code should give the same results, given the same inputs. To check this, in figure 3.1, the simulations carried out in figure 2.13 were repeated though this time the diabatic propagator was used. We can see in figure 3.1 that the results for the adiabatic and diabatic propagator are almost exactly the same for each model. In model three, where the problem with the divergent  $\mathcal{Q}_{lk,v}^{(I)}$  doesn't occur, the two results are exactly on top of each other. In the other models there is a slight

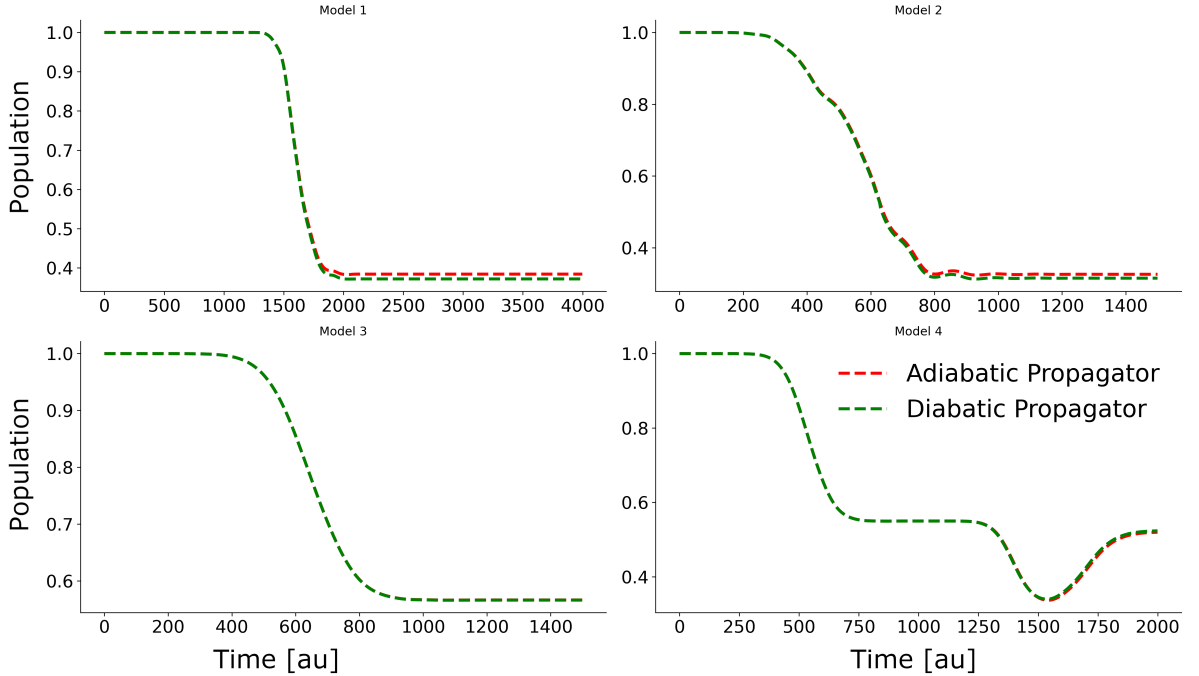


Figure 3.1: The four Tully models simulated using propagating the equations within a diabatic and adiabatic basis. The green line shows results from the diabatic propagator and the red line shows results from the adiabatic propagator. Model three shows an exact agreement between the adiabatic and diabatic propagators hence only one line is seen.

discrepancy. This is due to the unpredictable  $\mathcal{Q}_{lk,v}^{(I)}$  spikes not being perfectly corrected. However, figure 3.1 still serves as confirmation of the propagation within the diabatic basis.

### 3.3 Simulating Molecular Systems

To go beyond the 1D Tully model systems the AOM method is combined with CTMQC and applied to an Ethylene dimer. Fortunately, the majority of the code from the Tully model systems can be re-used. In fact, the only difference is the way the Hamiltonian (and diabatic NACE) is constructed. The code for carrying out these tasks (the AOM part) has been implemented by previous members of the group and has been well tested and verified against the literature and experimental studies. Therefore, I will not include any tests of this part of the code in this document but instead refer the reader to the numerous papers discussing AOM and its use in within the fewest switches surface hopping framework<sup>26,53,54,57,59–63,90,92</sup>. An ethylene dimer was chosen as a reasonable first

system due to its relative simplicity (shown in figure 3.2) the total number of atoms is twelve and only two electronic states will be considered. The system shown in figure 3.2

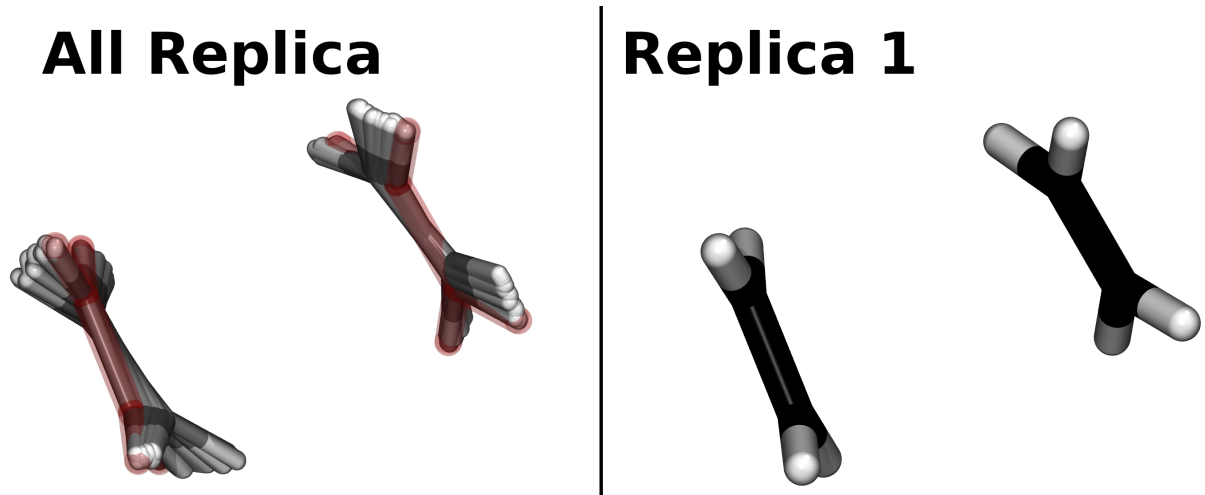


Figure 3.2: An example Ethylene dimer used to test the CTMQC implementation. The right panel shows the positions of just one replica. The left panel shows the positions of all replicas with the replica on the right highlighted in red.

was initialised in the adiabatic ground state. Positions and velocities were sampled from a short NVT molecular dynamics equilibration. The scaling factor ( $C$  in equation (3.1)) was chosen to give a coupling of approximately 27 meV. This is approximately  $\frac{1}{4} \times$  the reorganisation energy parameterised to be 100 meV. The amount of charge transfer is dependent on the ratio between reorganisation energy and the electronic couplings ( $\frac{H_{ab}}{\lambda}$ ). The factor of  $\frac{1}{4}$  was chosen to be a reasonable factor seen in other organic semiconducting systems. The nuclear timestep was chosen to be 0.05fs and the electronic one was 0.005 fs. The switch to  $\mathbf{R}_{0,v}^{(I)}$  was chosen as the correction method of the quantum momentum and 100 trajectories were used. A constant  $\sigma$  of 0.7 was used as the dynamic  $\sigma$  tended to either vanish to zero or blow up to a very large number.

In figure 3.3 the norm of the diabatic expansion coefficients are plotted, from the system described above. In this figure we see large jumps in the norm, these are caused by the divergences in the quantum momentum term. These occur more in this system than in the Tully models as it is more complex (more atoms, higher dimensional) and runs for a longer time with more avoided crossings. The fact that there are twelve atoms and three Cartesian dimensions instead of one means that the  $\mathbf{R}_{lk,v}$  term must be calculated many

more times increasing the probability of happening upon a divergence. For example, the Tully models tended to run for 10s of fs and had one value of  $\mathbf{R}_{lk,v}$ . The Ethylene dimer typically runs for 100s of fs encountering 10s of avoided crossings with 36 unique values of  $\mathbf{R}_{lk,v}$ . The errors can also accumulate meaning that after a few trivial crossings the populations become extremely noisy. This eventually causes the code to crash and results from it cannot be trusted. Most commonly the reason for the code crashing is a large spike in the computed forces caused by a spike in the quantum momentum. This large force then causes the atoms to collide and the code to crash. The code is very stable when just using Ehrenfest dynamics. Many more simulations have been carried out to

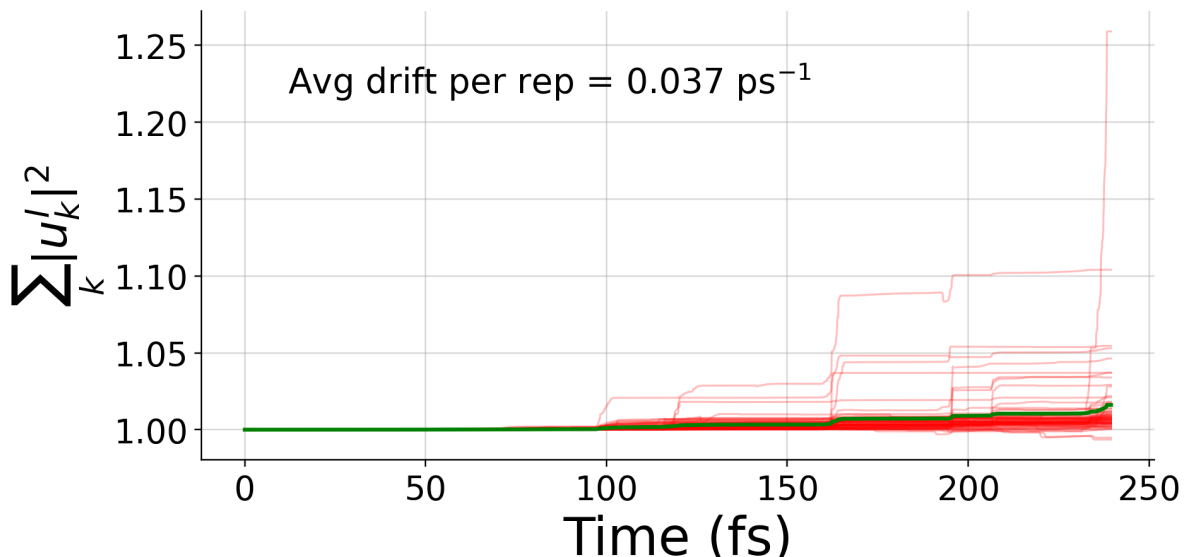


Figure 3.3: The norm of the adiabatic expansion coefficients. Thin red lines show the norm for each trajectory and the thick green line shows the average over all trajectories.

diagnose and fix this issue. Results from all of these cannot be included in this document though I will provide a brief summary of results below.

- Varying the number of replicas: Increasing the number of replicas in the system, somewhat counterintuitively, decreases stability. This is because with more replicas there is more of a chance the code will stumble upon a calculation giving a divergence in the quantum momentum term.

- Varying the timestep: Decreasing the timestep does help to improve norm conservation (before the code crashes). However, it does not lead to a more stable simulation that allows for longer timescales to be simulated. This is because decreasing the timestep provides more opportunity for a small numerical error to cause a divergence in the quantum momentum term.
- Removing Center of Mass Motion: In some simulations the replicas positions spread out so much that the quantum momentum term became negligible. This was to prevent that from happening.
- Varying the gaussian width ( $\sigma$ ) parameter: If the  $\sigma$  parameter is set to be large ( $> 2$ ) then the simulation is more stable as the quantum momentum term is smaller and errors don't accumulate as quickly. However, the limit of a very large  $\sigma$  is Ehrenfest dynamics. If the  $\sigma$  is set to be small ( $< 0.2$ ) the simulation becomes extremely unstable as the quantum momentum forces populations to decohere too quickly. This is discussed in more detail in section 2.3.
- Turning off the quantum momentum addition to the force term: The code runs more stably if the quantum momentum term is not included in the forces. This has also been shown to be much less important for the accuracy of the results than the quantum momentum addition to the coefficients. However, even in this case the code eventually crashes after an accumulation of errors in the coefficients results in erroneous forces resulting in geometries that fail CP2K internal checks.
- Renormalisation: This does not seem to help with stability. Furthermore, it merely helps hide the large norm drift and doesn't fix the problems it causes.

## 3.4 Conclusions

The CTMQC method shows great promise as a new nonadiabatic molecular dynamics (NAMD) technique. It was derived as the semi-classical limit of the exact factorisation of the time-dependent electron-nuclear wave function<sup>68,69</sup>. It purports to handle decoherence corrections in a more rigorous, first principles, way without the need of empirical parameters. Although this method was first reported in 2015<sup>69</sup>, there are still very few

papers reporting results using this method<sup>3,69,78</sup>. With the most complex system being restricted to a seven atom molecule simulated for just 10s of fs<sup>78</sup>. In this work, I have transformed the basis of the CTMQC equations, to an orthogonal diabatic basis, and implemented it within the FOB framework. This has allowed me to study to a molecular system (dimer of Ethylene) totalling twelve atoms, simulated for hundreds of fs. However, instabilities in the algorithm have prevented any physical conclusions being drawn from this. Before the widespread acceptance of CTMQC as a standard nonadiabatic molecular dynamics method, two critical flaws must be addressed. First is the calculation of the gaussian width parameter,  $\sigma$ , and the second is the divergence of the quantum momentum term. It would be possible to further investigate the width parameter, perhaps through benchmarks against higher level calculations to establish a relationship between it and other characteristics of the system. From a short investigation using the Tully models it seems a constant width parameter gives reasonable results and it should be set to be between 0.2 and 0.5. The on-the-fly update of the width parameter, from an algorithm given in Gossel<sup>3</sup>, provided even better results that came very close to the exact quantum dynamical values. Therefore, the setting of this width parameter does not seem like an intractable problem. However, it may be harder to correct for the large divergences in the quantum momentum caused by the denominator of the quantum momentum intercept term,  $\mathbf{R}_{lk,v}$ , approaching zero. This causes the code to become unstable for even simple molecular systems. In the 1D Tully models, this could be corrected by switching to an alternative intercept,  $\mathbf{R}_{0,v}^{(I)}$ . The switch occurs after two conditions are satisfied: a threshold on the time-derivative of the  $\mathbf{R}_{lk,v}$  term has been surpassed and the denominator of the  $\mathbf{R}_{lk,v}$  term is sufficiently close to zero. The correction helps conserve norm within the Tully model simulations. However, in larger, longer running simulations errors soon accumulate and the code becomes unstable. The Tully models also gave fewer divergences due to smaller run-times and the fact it is a simpler system. The alternative intercept results in unphysical population transfer in regions of zero nonadiabatic coupling, so cannot be used throughout the simulation.

Both these problems can both be traced back to the construction of the nuclear density

from the nuclear positions. The method explored in this thesis is the method reported in the literature. That involves placing a gaussian function centered on each atomic position with a certain width,  $\sigma$  to smear out the (point) position and give a smooth nuclear distribution. I believe that exploring alternative techniques to construct the nuclear density from atomic positions may lead to the largest improvements in the CTMQC technique. Perhaps even allowing one to study complex molecular systems with many nonadiabatic coupling regions such as those typically found in charge transfer studies.

Finally, the algorithm does not seem to conserve total energy. Using the equation for potential energy given in<sup>69</sup> we see that even very small nuclear timesteps do not conserve total energy to better than  $10^{-2}$  Ha ps<sup>-1</sup> atom<sup>-1</sup> in the best case. For reference, a good energy conservation within classical molecular dynamics is considered to be  $\sim 10^{-10}$  or less. Further, and perhaps more concerningly, reducing the timestep does not seem to improve the issue. This would be a major obstacle to CTMQC's widespread adoption as a nonadiabatic molecular dynamics algorithm and further work is needed to address the issue. In the rest of this work I will discuss an alternative NAMD technique, namely fewest switches surface hopping (FSSH), and apply it to large molecular systems to get experimentally verifiable results.

I have implemented and tested a working version of CTMQC both in CP2K and as a standalone python script. These are both available for downloading from the author's github page at: <https://github.com/95ellismle>.

## Chapter 4

# Charge transfer in amorphous systems

Although it is important to know the maximum bound on the mobility of the charge carrier in a perfect crystal of an organic semiconductor, in reality it is very difficult to control defect formation in OSs<sup>93,94</sup>. This is due to van der Waals forces only weakly holding molecules at lattice sites, allowing molecules greater freedom than in traditional inorganic crystal, and increasing the chance of defect formation which can trap/scatter charge carriers, thereby reducing overall mobility. This means it is important to investigate and characterise charge transport properties for not just perfectly crystalline OSs but also those that show a range of amorphicity.

In this chapter I investigate how structural disorder of the OS, on top of thermal disorder, changes the physical nature of the charge carrier, its localization length, transport mechanism and mobility. In particular, the degree of structural disorder at which the flickering polaron loses its delocalized character and becomes localized. This is important because a decrease in charge carrier delocalization correlates with a decrease in charge mobility, the essential result of transient localisation theory. To do so, I present quantum dynamical calculations of the charge carrier dynamics at room temperature in a number of samples of pentacene with varying levels of crystallinity, from fully amorphous to perfectly crystalline. The quantum dynamical simulation method, denoted fragment orbital-based surface hopping (FOB-SH), is well suited for this task because it makes no assumptions with regard to the charge transport mechanism. FOB-SH was shown to predict charge mobilities well over several orders of magnitude but it has so far only been

applied to single crystalline OS. Methodological developments by me and other members of the Blumberger group have now made it possible to apply this novel methodology, for the first time, to large samples of disordered OS with different nanoscale morphologies.

The molecule under investigation is pentacene. This molecule is a popular organic semiconductor and the subject of much research due to its high field effect mobility<sup>95</sup>, use in device applications<sup>96</sup> and, more recently, the use of functionalization to alter device properties<sup>97,98</sup>. The pentacene molecule consists of five joined benzene rings (thirty six atoms) and crystals typically pack with a herringbone motif as shown in figure 4.1.

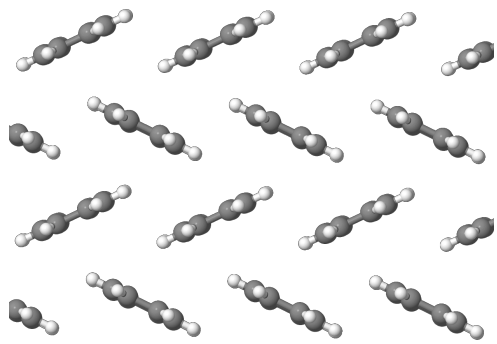


Figure 4.1: An example of the herringbone packing typically found in Pentacene crystals

## 4.1 Creating Amorphous Pentacene

In order to create the amorphous pentacene systems a melt-quench technique was used. This is a standard technique, often used to create amorphous systems in both computational and experimental fields<sup>99–103</sup>. The procedure followed is shown in figure 4.2.

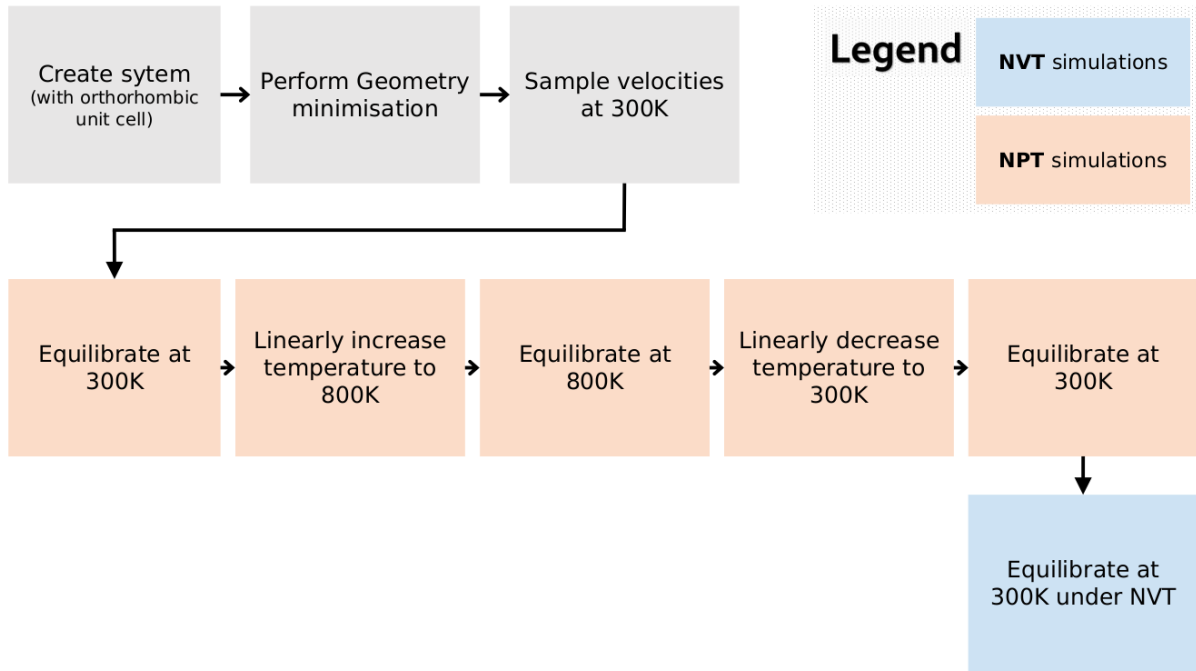


Figure 4.2: The melt-quench scheme used to create amorphous pentacene systems. Blue boxes indicate steps using an NPT ensemble, orange boxes indicate use of a NVT ensemble.

In this procedure, the system was initialised with an individual pentacene molecule on a regular three dimensional grid using an orthorhombic unit cell. This was chosen to make analysis of the resulting structures easier than with the triclinic unit cell typically used to simulate pentacene crystals. The velocities were initially randomly sampled from a gaussian distribution and a Nose-Hoover thermostat and barostat was used to control the temperature and pressure. The Lammps molecular dynamics package was used<sup>104,105</sup> and electrostatic interactions were handled with Lammps' particle-particle-particle-mesh ewald method<sup>106</sup>. RESP<sup>107</sup> (restrained electrostatic potential) partial charges were parameterised using Gaussian 16<sup>108</sup> with the B3-LYP<sup>109,110</sup> level of theory and a 6-311g(d) basis set. The use of partial charges was essential in the creation of the amorphous systems and neglecting them lead to unphysical face-to-face stacking of pentacene molecules. This is shown in figure 4.10, in section 4.3.1. Finally, for inter and intra molecular interactions

the general AMBER force-field<sup>111</sup> (GAFF) was applied. There isn't one predominant forcefield used in simulations of pentacene in the literature, though parameters from GAFF have been used and validated in a number of studies<sup>112–118</sup>.

Four different quenching times were used spanning four orders of magnitude: 0ns, 1ns, 10ns and 100ns. For the 0ns, 1ns and 10ns quenching simulations three thousand molecules were simulated. In the 100ns quenched structure three thousand and sixty molecules were simulated. The initial structure for the 1ns and 10ns quenched structures were taken from a restart of the 0ns quenched simulation after the 800K equilibration step. The 0ns and 1ns quenched structure were carried out under one atmosphere of pressure in x, y and z. However, the 10ns quenching required a small increase to five atmospheres as the structure had a tendency to deform such that one of the cell vectors became either very large or very small. In the 100ns quenched structure I updated the barostat target pressure (before the phase transition) to account for similar deviations in simulation box dimensions.

## 4.2 Structure of the quenched simulations

A movie showing the full 100ns melt-quench simulation can be found here: <https://youtu.be/6IQ-cYErQHVs>. Still images of the final snapshot of each different quenching time are shown in figure 4.3.

### 4.2.1 Final Structure Snapshots

We can see qualitatively that as we increase the quenching time from a) → d) the structure starts to look more ordered and crystal layers are starting to be formed. Looking longer at the structure we see that lower quench times tend to form small crystal clusters. In the 0ns quenched structure these clusters tend to be just ∼seven to ten molecules in size. As we increase the quenching time to 1ns we see one dimensional channels of crystalline pentacene start to form throughout the structure, though the structure is still relatively disordered due to these channels being randomly oriented with respect to one another. As we increase the quenching time these crystal fragments become larger until in the 100ns quenched structure the whole system is comprised of just two crystals. The reason for this

is, as the rate of cooling is decreased, the rate of crystal seeding is also decreased. At longer quenching times, more spent is spent at a temperature where it is unlikely for crystal to start to form –so fewer form. Those that do form can therefore propagate through the full system before being impeded by others. This can be seen in the animation of the [100ns melt quench simulation](#) linked above. The reverse is true for the shorter quenching times. In these systems, we quickly pass into a state that's energetically favourable for many crystals to start to form. These all propagate out at random orientations with respect to each other and block each other's growth.

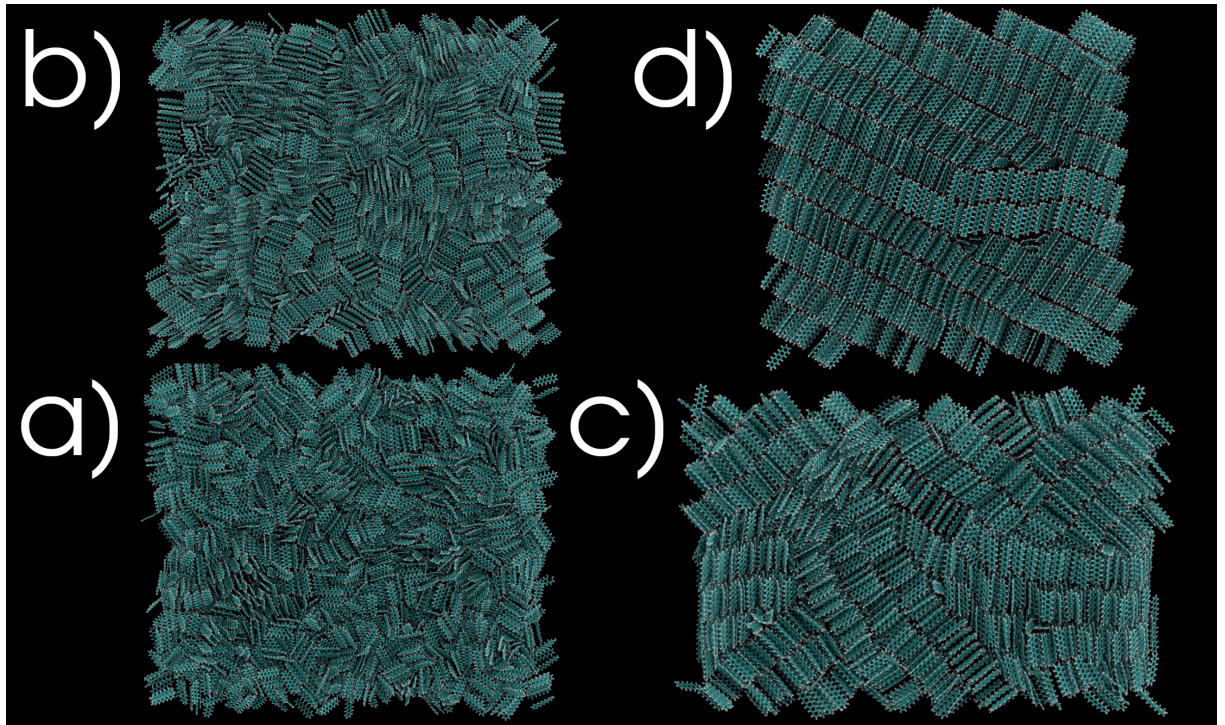


Figure 4.3: The final snapshot of each quenching simulation visualised in VMD<sup>4</sup> and rendered with Tachyon<sup>5</sup>. Snapshots are ordered by quenching time i.e. a) is the 0ns quench, b) is the 1ns quench and so on.

#### 4.2.2 Molecular Packing

We can isolate clusters in each of the different structures shown in figure 4.3 to reveal the molecular packing within. In figure 4.4 an algorithm similar to the density-based spatial clustering of applications with noise (DBSCAN) one<sup>119</sup> has been applied to the final structure from the 100ns quench to cluster molecules based on the density of centers of mass of molecules. These clusters have then been highlighted by different colours. The top-most

green cluster has been rotated such that, on the left, we are viewing it at an angle perpendicular to the plane of molecules, as shown by the cartoon eye. Comparing this plane to the crystal plane to the right, we can see a striking similarity in the packing motif. The herringbone packing has formed and (as can be seen in figure 4.7 in section 4.2.4) the herringbone intersection angle is remarkably similar to that of the crystal plane. This serves as a confirmation of the choice of force-field and the parameterisation of the partial charges.

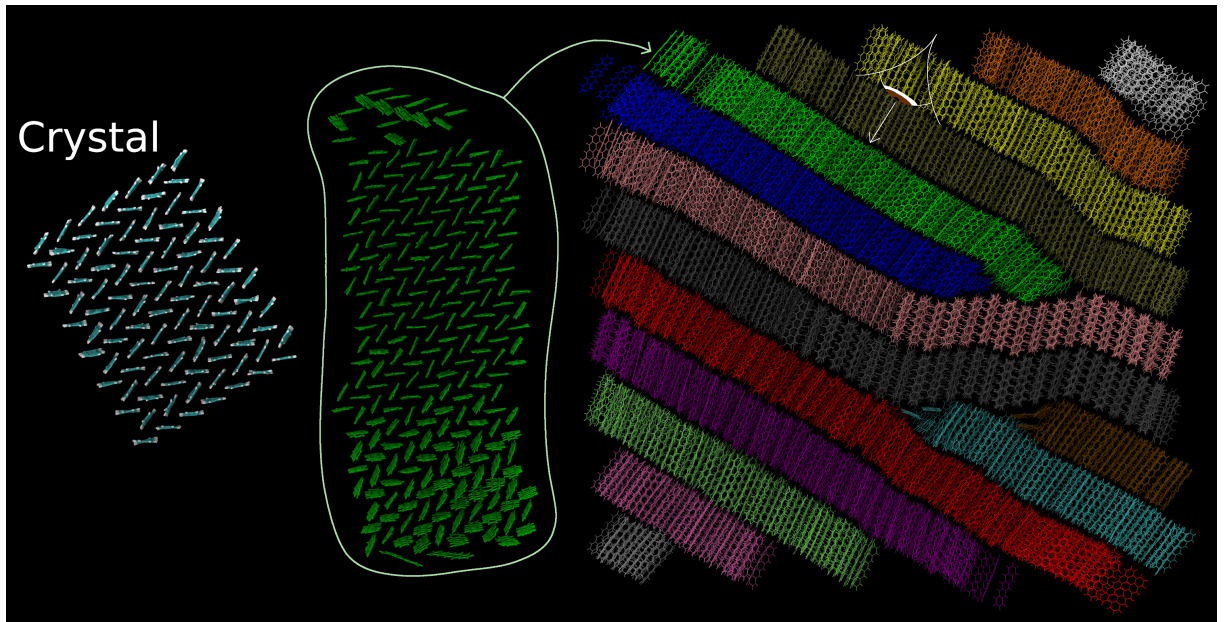


Figure 4.4: The 100ns quenched structure with different clusters shown with different colours. A bird's eye view of the green cluster has been shown on the left to demonstrate the herringbone packing within each cluster/layer. The far-right image labelled 'Crystal' is a snapshot of a crystal plane after a short MD equilibration.

Although this herringbone packing pattern is most obvious in the 100ns quenched structure, it can also be seen in the other structures too. At the other extreme in the 0ns quenched structure we see tiny clusters (<ten mol) of pentacene crystals forming. This is shown in figure 4.5. At this quenching time (zero to fifty ps) it was energetically favourable for many regions of the structure to start to crystallise

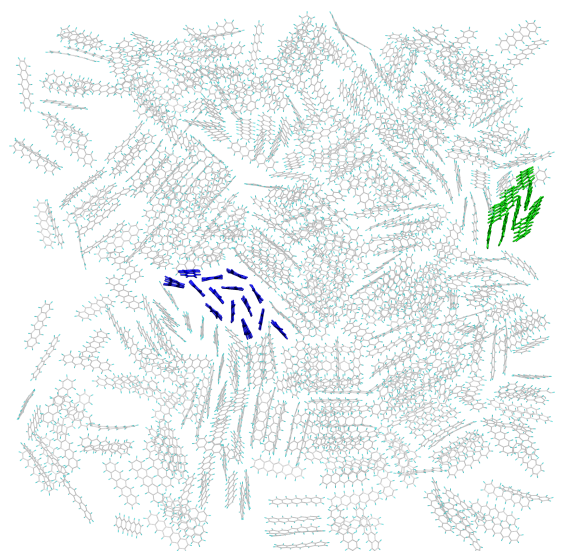


Figure 4.5: A slice from the 0ns quenched structure with two selected clusters displaying herringbone-like packing.

at once. This resulted in a high density of crystal fragments growing into each other and stopping when a neighbouring crystal fragment was encountered. In figure 4.5, two such clusters are shown in blue and green. In both clusters the packing motif has become very herringbone-like. However, due to their small size they are more affected by the surrounding environment which warps the structure slightly.

To quantify the change in the structure for the differently quenched structures three macroscopic properties have been plotted: the mass density, the angular distribution and the radial distribution function. These are discussed in the following sections.

#### 4.2.3 Mass Density

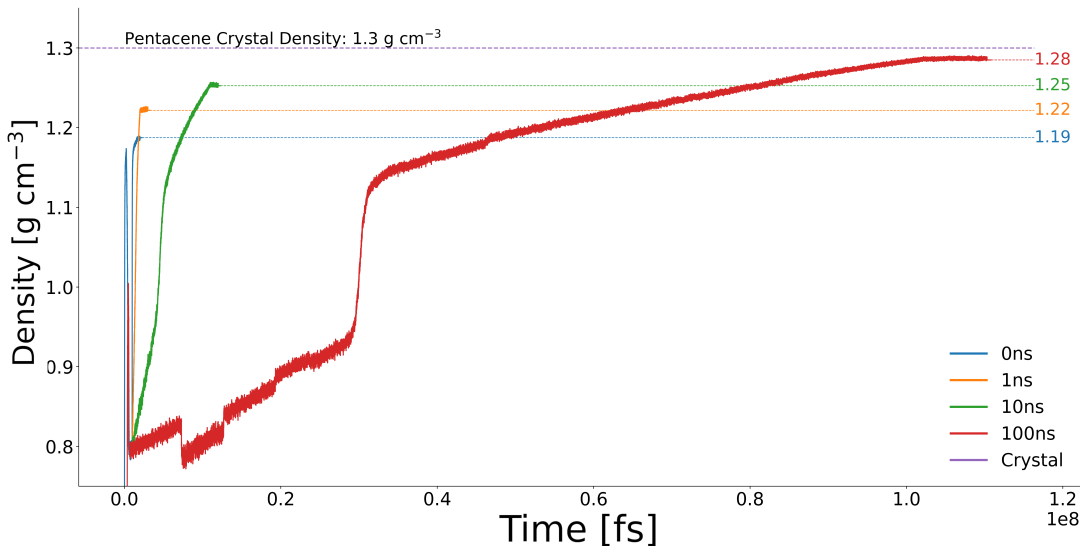


Figure 4.6: A time series of the density of the quenched structures. The black line shows the experimental mass density of crystal pentacene.

The mass density of the four different quenching simulations can be seen in figure 4.6. This was calculated by dividing the total mass of the atoms in the system by the volume (product of cell vectors) of the simulation box. The first thing to notice in this graph is as we increase the quenching time we increase the density of the final sample. This is due to the molecules packing more efficiently in the crystal than in an amorphous structure. We also see very clearly in the plots the sudden increase in density associated with the phase transition from liquid to solid Pentacene. In the 1ns quench structure (quenched with the barostat set to one atmosphere) this occurs around Pentacene's experimental melting of

530.15K<sup>120</sup> providing confirmation of the choice of force-field. The 0ns, 1ns and 10ns runs were performed in a single twenty four hour run. The 100ns quench was performed using many restarts, the discontinuities in the density for the 100ns structure come from these restarts. These do not affect the final structure as these only occur while the system is in the liquid state.

#### 4.2.4 Angular Distribution

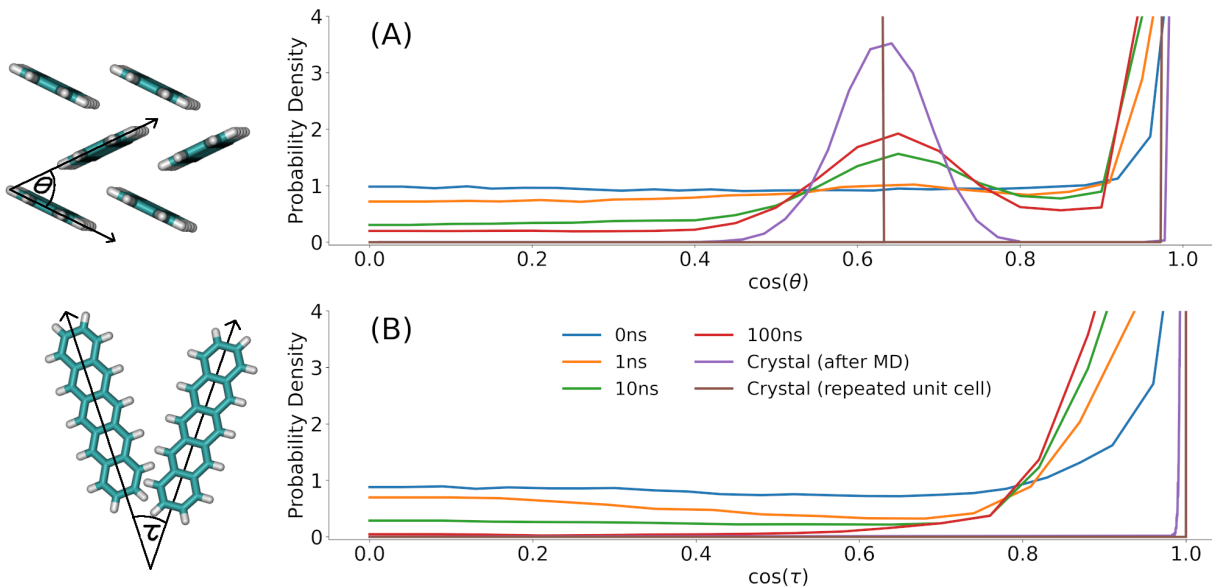


Figure 4.7: The angular distribution for the four different quench times is shown above. The brown and purple lines are from a perfect crystal before and after a short MD run. The others are after the various melt-quench simulations. On the right is a schematic showing which angles are referenced in each plot.

The angular distribution shows the distribution angles each molecule makes with the other molecules in the system. In figure 4.7 it was calculated by calculating the angle of an axis of each molecule with its nearest neighbours (a twenty Angstrom center of mass cutoff was used). This data was then grouped into a histogram which is plotted. In figure 4.7 we can see as the quenching time increases we start to notice an ever more prominent peak appear at either extreme of the x axis. This is because the molecules are aligning parallel with one another. The symmetry of the plot is an artefact of the melt stage of the simulation where each molecule was free to rotate randomly.

If we now look at the short axis plot we can see that, again, as the quench time in-

creases we start to see a more ordered structure start to form. This time the herringbone intersection angle between molecules ( $54.3^\circ$ <sup>121</sup>) within the herringbone structure is retrieved. This is a result of using partial charges in the simulation: running the same simulations without partial charges results in an unrealistic face-to-face stacking. The brown and purple line show the same calculation run on a crystal of pentacene before and after MD. The purple line comes from an analysis of a repeated unit cell, hence we get two delta functions: one at  $54.3^\circ$  and one at  $0^\circ$ . This structure was then equilibrated with electrostatics for 50ps and we start to see a broadening of the herringbone intersection angle and to a lesser extent (on the left side) a broadening of the angle between parallel pairs.

#### 4.2.5 Radial Distribution Function

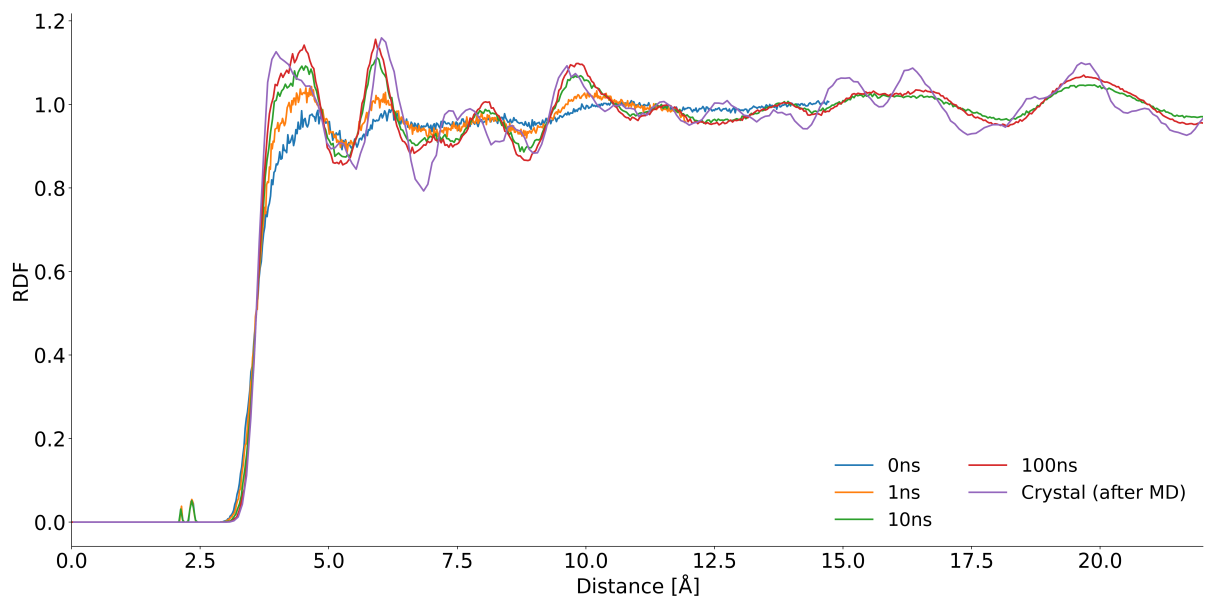


Figure 4.8: The carbon-carbon radial distribution function for four different quenching times and a crystal before and after 50ps of MD. The quenches (0, 1, 10 and 100ns) are shown in blue, orange, green and red respectively. The crystal data are shown in purple and brown.

The radial distribution function (RDF) describes the change of density from each particle in the system and is normalised to the bulk density (i.e.  $\frac{N}{V}$ ). This was calculated by counting the number of atoms within a spherical shell from each atom and then dividing by the volume between these spheres. This local density was then normalised to the

bulk crystal density. In systems with atoms regularly placed throughout the system we would expect to see sharp peaks in the RDF as there would be many gaps with no atoms. Conversely, with a totally amorphous system we would expect to see (once we reach a few times the Van der Waals radius from each atom) a flat line at one as local density should be very similar to the global density. This pattern is what we observe in figure 4.8. The sharp peaks of the purple line show the RDF of a perfect crystal (repeated unit cell) confirming we have a highly ordered system. On the other extreme, the blue line shows very weak ordering of the atoms' positions with any ordering vanishing after  $\sim 12.5\text{\AA}$  from each atom. This is due to the 0ns structure comprising primarily of small crystal fragments giving rise to a small amount of very local order but over longer distances this order vanishes. Again, as the quench time increases, the ordering increases resulting in larger peaks that more closely match the RDF of the crystal after a short MD equilibration.

#### 4.2.6 Crystallinity

In order to quantify the level of order within the system, an estimator of crystallinity based on the final mass density of the superstructure was used. The formula for this is presented below in equation (4.1)

$$C = 100 \left( \frac{\rho_{sample} - \rho_{amorphous}}{\rho_{crystal} - \rho_{amorphous}} \right) \quad (4.1)$$

This estimator simply linearly interpolates between the minimum (amorphous) density,  $\rho_{amorphous}$ , and the maximum (crystal) density,  $\rho_{crystal}$ . The relationship between the quenching time and this definition of crystallinity is shown in figure 4.9. Note in this figure, the quench time 0ns is missing. This is because the system didn't equilibrate instantly and it took approximately 100ps for the density to converge. It can be seen in this figure, that surprisingly, the crystallinity (final density) increases almost exactly logarithmically with respect to quench time. The black dashed line shows a line of best fit using the equation  $C = m \log_{10}(t) + C_0$  as a guide for the eye. This crystallinity parameter will be used when looking at the electronic transport properties (hole mobility and IPR) in the following section, in order to compare the electronic transport properties to a physically meaningful property.

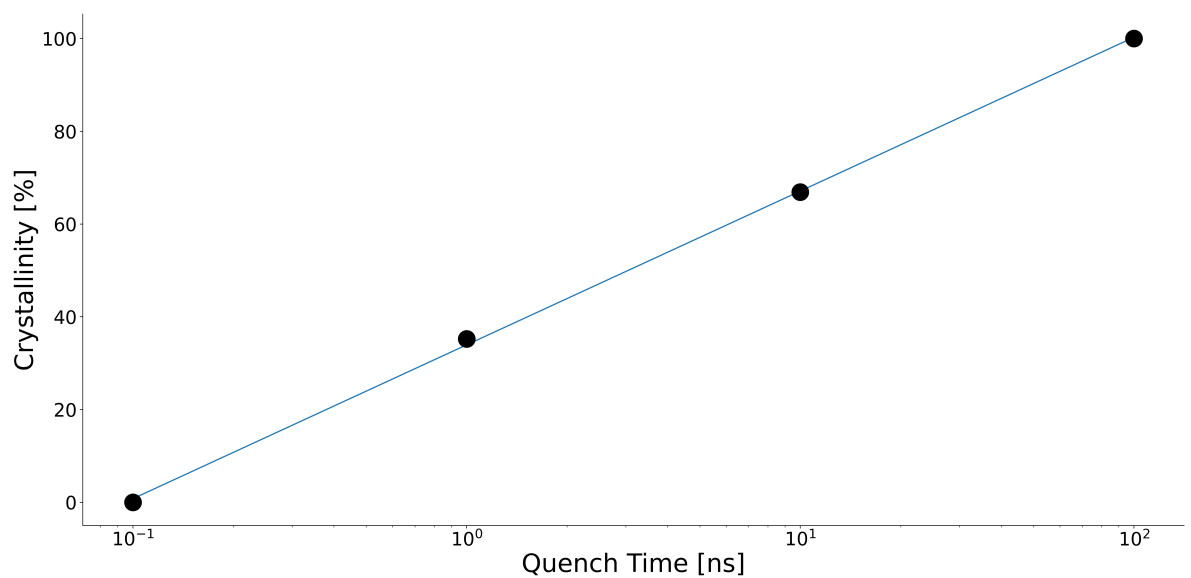


Figure 4.9: The quench time vs crystallinity given by equation 4.1. Black circles show raw data and the dashed black line is a line of best fit using the equation  $C = m \log_{10}(t) + C_0$ .

## 4.3 Charge Transfer Properties

We have seen that the final structure of the pentacene systems becomes more ordered and crystal-like as the quenching time is increased. It would be good now to see how this affects the charge transfer properties. A key quantity governing charge transfer rates is the ratio between electronic coupling and reorganisation energy,  $\frac{H_{ab}}{\lambda}$ . Seeing as we have a single molecule system, by plotting the electronic coupling we can get a qualitative view of the charge transfer dynamics and see which paths are the most likely within the structure.

### 4.3.1 Global Couplings

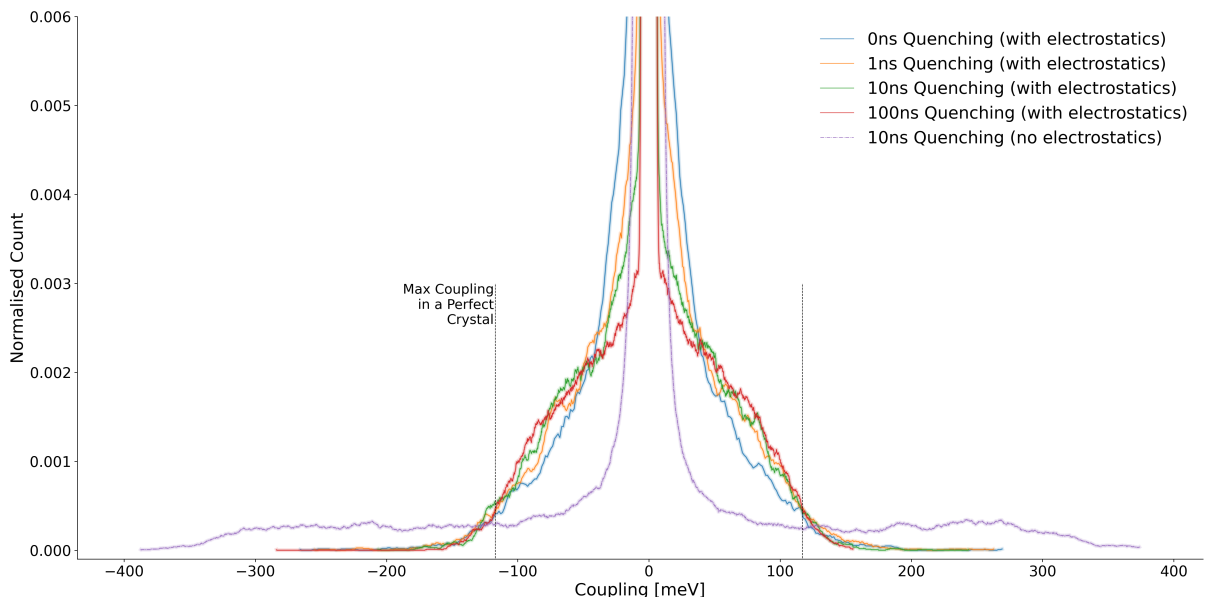


Figure 4.10: The global coupling distribution for each of the quenched structures (in blue, orange, green and red) and one structure after a 10ns quench without using electrostatics (purple line). The black dashed lines represent the maximum coupling within a perfect pentacene crystal.

The global coupling distribution gives an overview of the values of coupling within the system, hence an idea of the charge transport properties of the system. To calculate these couplings I have used the analytic overlap method (AOM)<sup>58</sup> between all pairs of molecules (using a nearest neighbour cutoff) in the final snapshot of each quenched system. As can be seen from figure 4.10, as the quench time increases a shoulder starts to form in the distribution at a high coupling value (approximately eighty meV). This is

especially obvious in the 100ns quench structure (red curve) which has far fewer lower energy couplings and more coupling values approaching the crystal maximum of one hundred and seventeen meV.

The figure also highlights the importance of a correct account of electrostatic interactions in the formation of these structures. The purple line shows the coupling distribution for the same simulation without any electrostatics. In this curve we see far more very high values of coupling –substantially higher than those seen in the perfect crystal. This is due to it now being energetically favourable to form more tightly packed face-to-face structures giving rise to larger molecular overlaps hence higher couplings. The effect of the inclusion of electrostatic interactions has been discussed in other studies<sup>122–124</sup>. In short, the positive charges on the outside of each pentacene molecule and the negative charges in the centre forces each molecule to align tilted with respect to one another. We see all the other distributions fit well between the two black lines, which denote the maximum coupling value in a perfect crystal. This serves as a further confirmation of the forcefield parameterisation.

### 4.3.2 Coupling Networks

In figure 4.11, the lower row shows representative two dimensional cuts through each of the quenched samples. These are the areas coloured in gray. In the middle row, the centres of mass of each molecule are joined with lines according to the strength of electronic coupling ( $H_{ab}$ ) between them. Blue, green and red lines depict small, medium and high coupling strengths respectively. The categories are:  $\lambda/100 \leq H_{ab} < \lambda/10$ ,  $\lambda/10 \leq H_{ab} < \lambda/2$  and  $\lambda/2 \leq H_{ab}$ , where  $\lambda$  is the molecular (or inner-sphere) reorganisation free energy of pentacene, ninety eight meV. If the picture of hole hopping between molecules was applicable, the blue and green lines would correspond to ET steps in the non-adiabatic and adiabatic regime, respectively. For all red connections, ET theory breaks down because at this point electronic coupling is so strong that there is no longer an activation barrier between initial and final state and the charge carrier starts to delocalise<sup>63</sup>. As expected, it is observed that the sample becomes electronically better connected (more red connections) as the crystallinity increases. This is quantified by clustering regions of high couplings

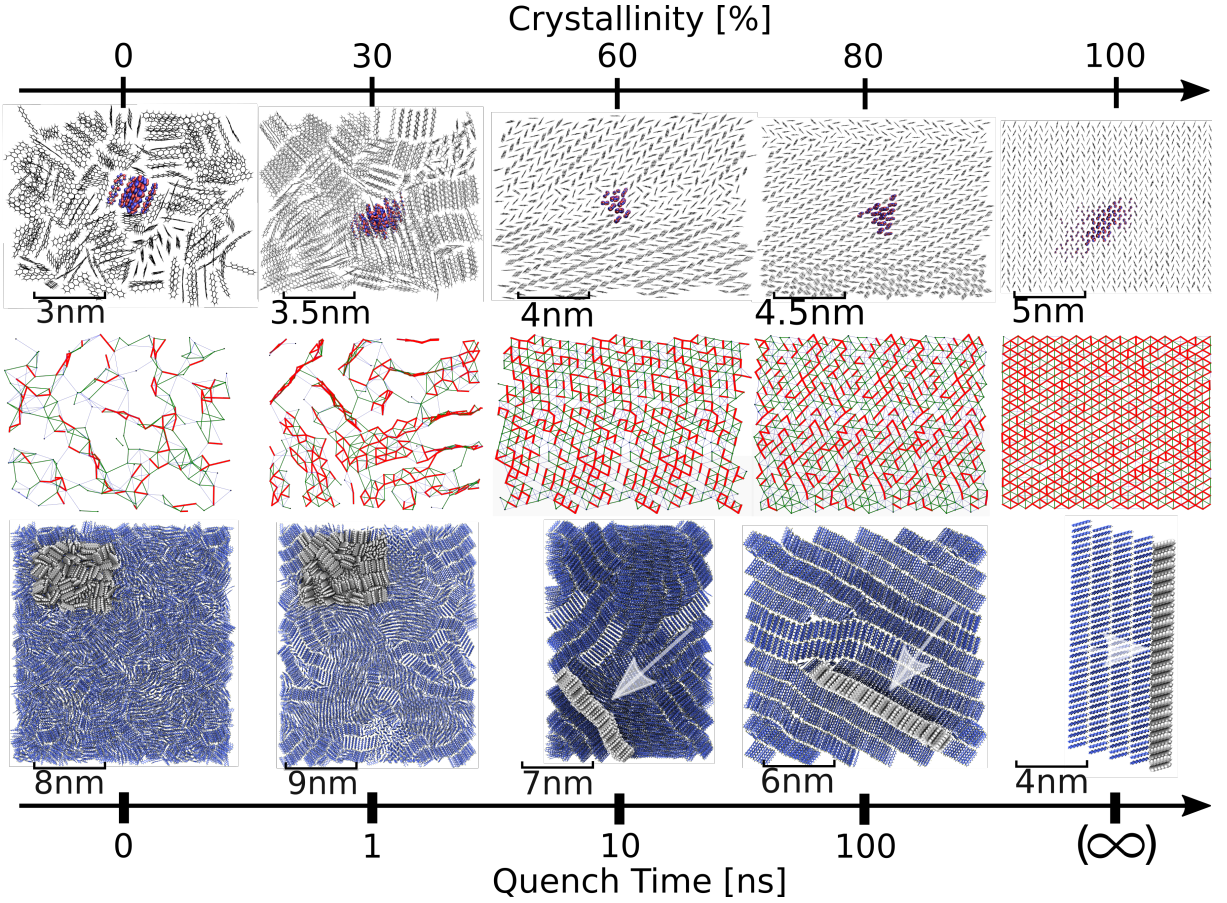


Figure 4.11: Structure and electronic properties of bulk pentacene phases. The disordered structures were obtained from melt-quench molecular dynamics simulation. The bottom row, show a 'front on' view of the entire simulated sample of three thousand molecules for amorphous and nanocrystalline phases. The final (far-right) image shows the experimental structure of single-crystalline pentacene (polymorph I)<sup>6</sup>. The region highlighted in light gray, in the following denoted 'active region', is shown enlarged in the middle and bottom rows and viewed 'front on' or as indicated by arrows. The middle row, shows a weighted graph of electronic couplings within the active region. Molecular centers of mass are joined with lines denoting coupling strengths relative to the re-organisation energy of the pentacene molecule. Blue lines depict couplings of  $\frac{\lambda}{100} \leq H_{ab} < \frac{\lambda}{10}$ , green lines depict couplings of  $\frac{\lambda}{10} \leq H_{ab} < \frac{\lambda}{2}$  and red lines depict couplings of  $\frac{\lambda}{2} \leq H_{ab}$ . The upper row, depicts an isosurface of the hole carrier wavefunction,  $\Psi(t)$  (Eq. (1.6)), during FOB-SH simulation of charge transport (red and blue). The crystallinity is an indication of the structural order of the system and was calculated from linearly interpolating between the mass-density of amorphous and single crystalline phases.

as sets of  $N$  molecules that can all be connected with an uninterrupted path of red lines (see Table 4.1 for a summary). In the amorphous sample (0ns) formation of small islands of size four plus or minus four molecules begins. At thirty percent crystallinity these

Table 4.1: Properties of pentacene in different bulk structures and in ultrathin (2D) films.

$\tau$ (ns) <sup>a</sup>	structure <sup>b</sup>	$\rho$ (g cm <sup>-3</sup> ) <sup>c</sup>	bulk pentacene				$\mu^{g,h}$ (comp)	$\mu^h$ (exp)	
			$Cr$ (%) <sup>d</sup>	$N^e$	IPR <sup>f</sup>				
0	am	1.19	0	$4 \pm 4$	3.0	0.21			
1	nc	1.22	30	$5 \pm 5$	3.8	0.23			
10	nc	1.25	60	$7 \pm 9$	4.8	0.92			
100	nc	1.28	80	$9 \pm 16$	9.5	1.8			
( $\infty$ )	sc	1.30	100	$\infty$	17	10		$5^i; 5.6^j$	
2D pentacene									
	sc, 1L			$\infty$	5.4	4.2		1.6 <sup>k</sup>	
	sc, 2L			$\infty$	12	7.3		3 <sup>k</sup>	

islands become connected resulting in the formation of elongated one dimensional paths, which extend to two dimensional clusters at sixty percent crystallinity. At eighty percent crystallinity these clusters grow to nine plus or minus sixteen molecules, but still short of the formally infinitely large cluster size of the single crystal. The notably wide spread in cluster size distribution is due to the presence of a large number of smaller clusters (two to four molecules). This, as will be discussed further below, has a marked impact on electron hole delocalisation and mobilities.

<sup>a</sup> Quench time from 800 K to 300 K in molecular dynamics simulation in the NPT ensemble.

<sup>b</sup> am = amorphous, nc = nanocrystalline, sc = single crystalline, 1L = 1 wet layer + 1 sc monolayer, 2L = 1 wet layer + sc bilayer.

<sup>c</sup> Mass density.

<sup>d</sup> Crystallinity, see main text for definition.

<sup>e</sup> Mean and root-mean-square fluctuation of number of molecules in clusters with high coupling, see main text.

<sup>f</sup> Equation (4.2), defined later.

<sup>g</sup> Equation (4.6), defined later.

<sup>h</sup> in units of cm<sup>2</sup> V<sup>-1</sup> s<sup>-1</sup>.

<sup>i</sup> Ref. <sup>16</sup>, OFET, single crystal on Al<sub>2</sub>O<sub>3</sub>+ionic liquid, polymorph I.

<sup>j</sup> Ref. <sup>17</sup>, OFET, thin single crystal on SiO<sub>2</sub>.

<sup>k</sup> Ref. 14, OFET, ultrathin (2D) single crystal on boronitride.

Finally, in figure 4.11, the upper row shows a representative wavefunction for each of the systems studied. In the first image (zero percent crystallinity) we see the wavefunction localised primarily on a single molecule with a small tail its neighbours. As the crystallinity increases so too does the delocalisation of the wavefunction, until eventually, in the single crystal sample (one hundred percent crystallinity) the wavefunction is delocalised over seventeen molecules.

## 4.4 Surface Hopping Methodology

Several experimental as well as computational studies have indicated that charge transport in crystalline molecular OS falls into a difficult regime where the charge is neither fully delocalised over the bulk material nor completely localised on a single molecule, as had often been assumed.<sup>125–131</sup> It has recently been shown, using advanced quantum dynamical simulations, that charge carriers in single-crystalline OS form “flickering polarons”, objects that are half-way between waves and particles<sup>26,62,132</sup>. It was found they are delocalised over up to ten to twenty molecules in the most conductive crystals and constantly change their shape and extension under the influence of the thermal motion of the atoms (crystal vibrations). Taking the example of bulk crystalline pentacene, it was found that the excess hole is typically delocalised over seventeen molecules, in excellent agreement with experimental estimates from electron spin resonance data (seventeen molecules). The delocalisation of the polaron and mobility are limited by the thermal fluctuations of electronic coupling (off-diagonal electron-phonon coupling) and site energy. This picture of charge transport, obtained by numerically solving the time-dependent electronic Schrödinger equation coupled to nuclear motion, resembles closely, and gives support to, the transport scenario predicted by the recently established Transient Localisation Theory (TLT).<sup>30,31</sup> However, this makes simulating the charge carrier particularly difficult as the two standard techniques (hopping and band theories) breakdown in this regime. Further, TLT is inapplicable to systems with high levels of disorder. For this reason, fragment orbital surface hopping (FOB-SH) was used to simulate the motion of the excess charge carrier in each of the samples and hole-mobilities and inverse participation

ratios (IPR) were calculated.

The FOB-SH methodology is a combination of Tully's original fewest switches surface hopping (described in the introduction) with fragment orbital based framework (described at the beginning of chapter ). That is, the Hamiltonian is constructed with diagonals calculated from a classical force-field and off-diagonals calculated from the overlap between singly occupied molecular orbitals (SOMOs). Various extensions to the original surface hopping method have been added to account for overcoherent propagation and trivial crossings leading to spurious transfer. These are mentioned in the introduction and have been discussed at length in various papers<sup>53,54,57,59–62</sup>.

#### 4.4.1 Surface Hopping Setup

The surface hopping simulations require a swarm of hundreds of independent trajectories (two hundred to five hundred), each with slightly different geometries to fully sample phase space. To create these trajectories, initial positions and velocities were sampled every 1ps from a classical MD simulation (carried out under NVT). In order to initialise the (electron-hole) wavefunction for each trajectory, the Hamiltonian was calculated. This was then used to find an adiabatic state within  $3k_B T$  of the ground state energy and relatively close to the center of the simulated system. The details of this procedure are given in appendix H. This initialisation of the wavefunction in a low lying adiabatic state allowed for quick convergence of the mean-squared displacement of the charge carrier. Other parameters, such as the method chosen for correcting for over-coherence, trivial crossings and spurious transfer were taken from previous surface hopping simulations carried out by other members of the Blumberger group. The code at the time did not support the calculation of electrostatic interactions. So, in order to maintain the structure from the melt-quench simulations, center of mass restraints were used. These are shown in appendix I. Finally, the full system for each of the four quench times was very large (three thousand mol). So, to sample the mobility at various points within the superstructure the full system was divided into smaller subsystems. The procedure for dividing the superstructure was different for each quench time and full details are given in appendix J. In the 0ns and 1ns quenched runs, the full system was divided into six roughly even

slabs. This was because these structures had very little order and the charge transport was expected to be isotropic. In the 10ns and 100ns quenched systems, a DBCAN-like algorithm<sup>119</sup> was used to cluster molecules (by mass-density). These clusters were then used as active regions within the surface hopping code. It is important to note that, although it is not thought to affect the FOB-SH simulations within the single-crystal sample, electrostatics are thought to reduce the mobilities within the more amorphous samples. This is due to an increase in energetic disorder<sup>133</sup> from the electrostatics. This will be the subject of further research and in the following chapter, two implementations of electrostatic interactions within the FOB-SH code will be presented.

#### 4.4.2 Inverse Participation Ratio

The inverse participation ratio (IPR) gives a measure of spread of the polaron. A value of one would mean the polaron is localised on a single molecule, a completely delocalised polaron would have a value of  $N_{mol}$  where  $N_{mol}$  is the number of molecules in the system. The formula used in its calculation is given below in equation (4.2):

$$IPR(t) = \frac{1}{N_{\text{traj}}} \sum_{n=1}^{N_{\text{traj}}} \frac{1}{\sum_i^{N_{\text{mol}}} |u_i^n(t)|^4} \quad (4.2)$$

Where  $N_{\text{traj}}$  represents the number of trajectory (molecules) and  $u_i^n(t)$  is the diabatic expansion coefficient at time  $t$ , on replica  $n$  and molecule  $i$ .

The IPR is an important quantity as the level of delocalisation of the wavefunction is positively correlated with its mobility. That is, molecular systems that have a large delocalisation of the charge carrier tend to have larger mobilities. It is also useful in determining if the system has reached equilibrium, as in equilibrium the IPR tends to converge to a constant value.

##### 4.4.2.1 Quantum Localisation Results

Three qualitatively different charge transport mechanisms are observed, depending on the crystallinity of the sample. These can be seen in figure 4.12, where the hole wavefunction is plotted embedded within the molecular system. In the amorphous sample (Figure 4.12

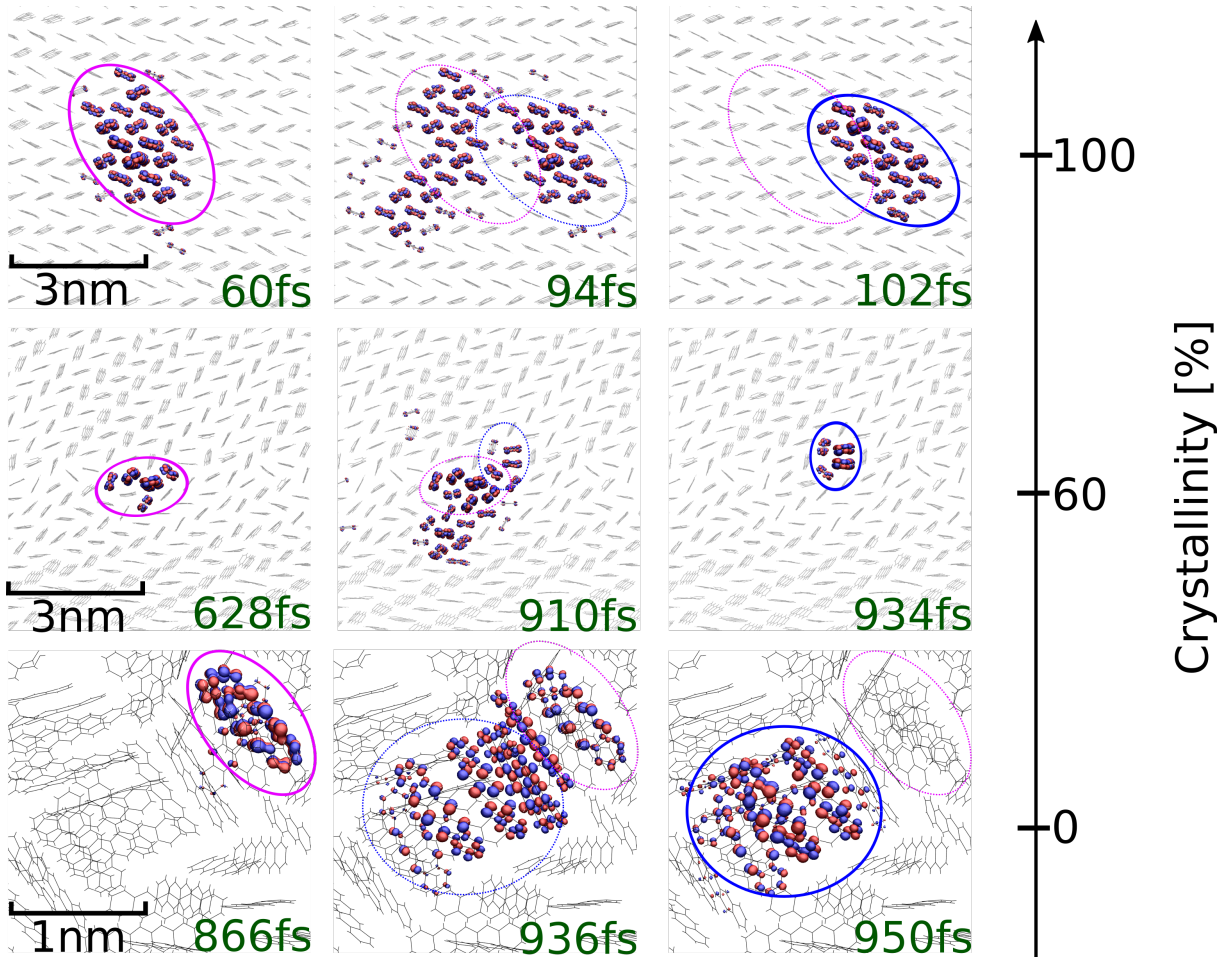


Figure 4.12: Mechanism of hole transport in bulk pentacene phases. The transport scenario for amorphous, nanocrystalline and single-crystalline pentacene are shown in the bottom, middle and top row, respectively. Pentacene molecules are shown in grey stick representation and the crystallinity of the phases is indicated on the scale to the right. Isosurfaces of the charge carrier wavefunction,  $\Psi(t)$  (Eq. 1.6), are depicted in red and blue colors for three different times along a FOB-SH trajectory as indicated. The red and blue colours depict positive and negative phases of the wavefunction. The initial positions and extensions of the hole polaron are shown in the snapshots to the left (circles in pink), the transitions to the new positions are shown in the snapshots in the middle, and the hole polaron in the new position is shown in the snapshots to the right (circles in blue). Notice the different extent of hole carrier delocalisation for the different phases.

bottom row), the localized charge is observed to hop infrequently from one small island to the next via transient delocalisation over and relocalisation on a new island, confirming the charge hopping mechanism that is often assumed for disordered structures. There is no preferential direction for hopping, the transport is slow and isotropic. The situation is markedly different at sixty percent crystallinity (Figure 4.12 middle row) In this system, as a consequence of multiple crystal domains forming, the transport mechanism is strongly dependent on the initial position of the charge. If initialized within an interfacial region (more static disorder), the transport remains sluggish and the polaron is localized over just a few molecules. When initialized within the crystal domain, the transport is similar to that of the eighty plus percent crystallinity samples. In these, more crystalline, systems (Figure 4.12 top row) the delocalized charge carrier frequently expands to more than twice its original size, preferably along the high coupling direction T1 within the herringbone layer, followed by collapse to its original size at a neighbouring region in the crystal. These “diffusive jumps” of a “flickering” polaron as they have previously been called<sup>26,62</sup> displace the centre of charge of the polaron by several lattice spacings at a time resulting in high (and anisotropic) charge mobilities.

To quantify this change in localisation of the wavefunction with respect to crystallinity, the IPR is plotted, along with the hole mobility, in figure 4.13. It is clearly visible that the delocalisation of the carrier wavefunction, defined in terms of the inverse participation ratio (IPR, Eq. (4.2)), increases with increasing crystallinity, reflecting the trend seen in the electronic coupling maps. In the amorphous sample, the static disorder of electronic coupling results in the wavefunction localising, on average, over just two to three molecules. At thirty percent and sixty percent crystallinity, the high concentration of defects restricts wavefunction delocalisation over five to six molecules, whereas at eighty percent we observe a marked increase to ten molecules, which is still some way off from the value for the single crystal, seventeen molecules. At this point we also see for the first time a clear spatial anisotropy of the charge carrier wavefunction extending more strongly along the T1 high coupling direction in the pentacene crystal (diagonal direction in Figure 4.9). Remarkably, a good correlation between the IPR and the cluster size in

the electronic coupling map can be seen in Table 4.1 suggesting that carrier delocalisation is limited by static disorder of electronic coupling. This correlation is lost for the single crystal because in this case delocalisation is limited by the thermal disorder of electronic couplings (i.e., dynamic or electron-phonon coupling).

#### 4.4.3 Hole Mobilities

A full discussion of the calculation of the charge carrier mobility calculation can be found in various papers<sup>26,53,54</sup>. It is calculated from the Einstein diffusion constant,  $D$ , which in turn is calculated from the change in the mean squared displacement (MSD) of the charge carrier. The MSD is calculated via equation (4.4) below

$$MSD_{ab}(t) = \frac{1}{N_{\text{traj}}} \sum_{n=1}^{N_{\text{traj}}} \langle \Psi^n(t) | (\mathbf{R} - \mathbf{R}_0)^2 | \Psi^n(t) \rangle \quad (4.3)$$

$$\approx \frac{1}{N_{\text{traj}}} \sum_{n=1}^{N_{\text{traj}}} \left( \sum_i^{N_{\text{mol}}} |u_i^n(t)|^2 (\mathbf{R}_i^n(t))^2 \right) \quad (4.4)$$

where  $\Psi^n$  is the wavefunction for trajectory  $n$ ,  $\mathbf{R}$  is the position coordinate and  $\mathbf{R}_0$  is the position coordinate at time  $t = 0$ .  $\mathbf{R}_i^n(t)$  is the time-dependent position of the center of mass of molecule  $i$  on trajectory  $n$ . Equation (4.3) is the exact quantum mechanical equation for the MSD, equation (4.4) is the equation that is used to calculate the MSD from the surface hopping output. The quantity is in general a three by three matrix and the values  $a$  and  $b$  are indices indexing each of the three Cartesian dimensions.

After a short equilibration, the MSD increases linearly. This is indicative of Einstein diffusion and the coefficient can be calculated, in this linear regime, as in equation (4.5) below:

$$D_{ab} = \frac{1}{2} \lim_{t \rightarrow \infty} \frac{d}{dt} MSD_{ab}(t) \quad (4.5)$$

In order to calculate the time-derivative of the MSD, a line of best-fit is fitted to the MSD vs simulation time and the gradient is calculated. This is then used in the calculation of the mobility in equation (4.6) below.

$$\mu_{ab} = \frac{eD_{ab}}{k_B T} \quad (4.6)$$

Where  $k_B$  is the Boltzmann constant,  $e$  the elementary charge and  $T$  is the temperature. The charge mobility is a quantity that can be calculated in experimental studies, so is an important quantity to calculate. It shows how quickly charge can be transported across a system and can be used to calculate other important quantities such as drift velocity ( $v_d = \mu E$ ) or conductivity ( $\sigma \propto \mu N_{carrier}$ ).

#### 4.4.4 Surface Hopping Results

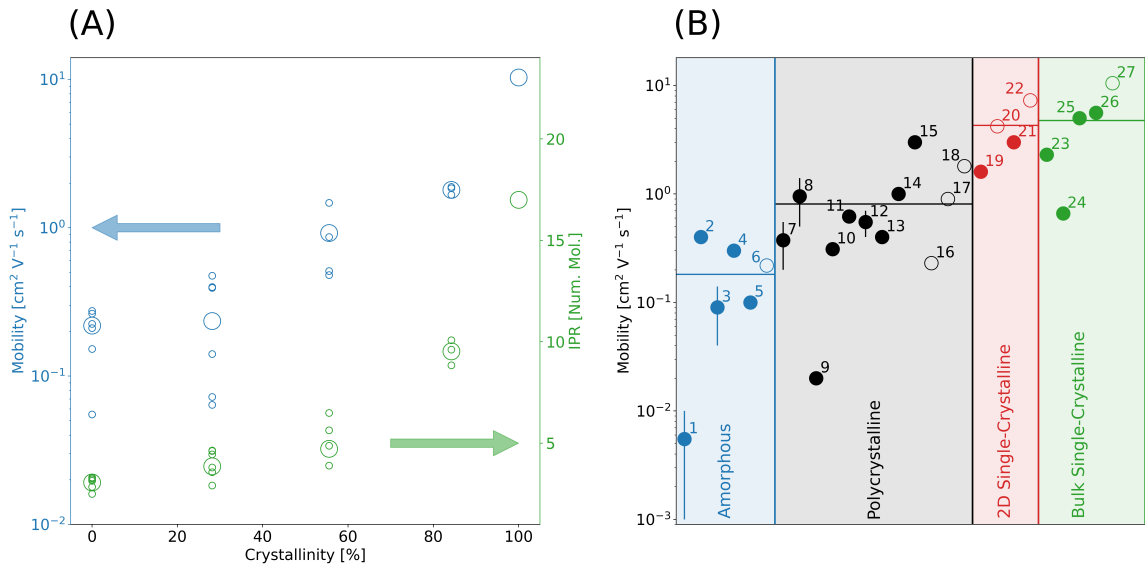


Figure 4.13: Hole mobilities and inverse participation ratio (IPR) for the pentacene phases studied. In (A), computed hole mobilities and IPR from FOB-SH simulation are shown for bulk pentacene phases as a function of the crystallinity of the sample (blue and green circles, respectively). The local mobilities and IPR for different regions of the sample are shown in small circles and the averages are shown in large circles. In (B), computed mobilities for bulk pentacene phases and 2D pentacene layers (hollow circles) are compared to experimental results (filled circles). The bulk pentacene phases were classified as ‘amorphous’, ‘polycrystalline’ and single-crystalline. The mean value for each category is given by a horizontal line. Error bars for computed values indicate the spread in local mobility. 1,2: ref.<sup>7</sup>, 3: ref.<sup>8</sup>, 4,5: ref.<sup>9</sup>, 6: this work,  $Cr = 0\%$ , 7,8: ref.<sup>10</sup>, 9,10,11: ref.<sup>11</sup>, 12: ref.<sup>12</sup>, 13,14,15: ref.<sup>13</sup>, 16: this work,  $Cr = 30\%$ , 17: this work,  $Cr = 60\%$ , 18: this work,  $Cr = 80\%$ , 19: ref.<sup>14</sup>, 20: this work, 2D pentacene, 1L, 21: ref.<sup>14</sup>, 22: this work, 2D pentacene, 2L, 23,24: ref.<sup>15</sup>, 25: ref.<sup>16</sup>, 26: ref.<sup>17</sup>, 27: this work,  $Cr = 100\%$ . Additional information on the device measurements and gate dielectrics used can be found in appendix K, Table K.1.

#### 4.4.4.1 Hole Mobilities

Hole mobilities for all samples were obtained as explained in section 4.4.3. For each superstructure multiple active regions were selected to calculate a mobility for. These “local” charge mobilities can show the impact of structural inhomogeneity of the quenched samples on charge transport. It can be seen that in the disordered samples, especially the one with approximately thirty percent crystallinity, the local charge mobilities and IPR values exhibit a relatively large spread as some regions are more crystalline and thus more conductive than others (Figure 4.13, small open circles). In the structurally more homogenous sample with eighty percent crystallinity, the variation in local mobility becomes almost negligible. The average of the local charge mobilities and IPRs correlate well with the crystallinity of the sample (Figure 4.13, large circles). In figure 4.13 Panel B, I have also included results from simulations and experimental measurements of mobility calculated for a two dimensional thin film polymorph of pentacene, to fill the gap between polycrystalline and single-crystalline. The structure for this system is reported in Zhang et al<sup>14</sup> and the simulations were carried out by a previous member of the group: Dr Samuele Giannini.

Over the last twenty years a large number of experimental hole mobilities have been reported for pentacene thin films and crystals from organic field effect transistor (OFET) measurements. Yet, there are several issues to consider when comparing my calculations to these measurements. In OFETs charge transport is typically probed on the micrometer scale over macroscopic time scales, whereas present calculations are carried out for nanoscale samples over short times (ps-ns). Moreover, OFET mobilities have been shown to be very sensitive to many details of the preparation method including, e.g., the gate dielectric used, the surface roughness, deposition rate and temperature etc. This can be seen in the very large spread of experimental mobilities for amorphous pentacene (figure 4.13, panel B -blue section). My calculated value of hole mobility, of  $0.14 \text{ cm}^2 \text{ V}^{-1} \text{ s}^{-1}$ , fits towards to upper end of this spread. It is suspected that the inclusion of electrostatic interactions may reduce this further. A more in-depth discussion of the role of electrostatics can be seen in Martinelli et al<sup>133</sup>.

Notwithstanding the above caveats, the correlation between experiment and computed FOB-SH mobilities is rather good, which supports the mechanistic picture that my simulations have revealed. The simulated results have been compared to experimental values for the fully amorphous and fully crystalline samples. For the fully crystalline sample the agreement to experiment is very good, my simulations produced a value of  $10.3 \text{ cm}^2 \text{ V}^{-1} \text{ s}^{-1}$  whereas experimental studies have reported values ranging from  $5\text{--}10.5 \text{ cm}^2 \text{ V}^{-1} \text{ s}^{-1}$ . Again the value reported in this work sits at the upper end of the experimentally reported values for reasons discussed previously.

## 4.5 Conclusions

In this chapter, I have presented a molecular dynamics method for tuning the crystallinity of a pentacene sample based on melting and subsequently quenching the sample over various timescales. I have shown, as was expected, that longer quench times lead to more ordered structures and discussed the mechanism leading to this. That is, in longer quench times the few crystal fragments that begin to seed have a longer time to grow before their growth is impeded by neighbouring crystal fragments. I have displayed various macroscopic properties that confirm that the longer quench times do indeed show more order, including mass-density, angular distribution and the radial distribution function. Further, I have presented networks of electronic coupling within each of the quenched systems, that can be used to get a qualitative feel for the electronic transport properties without expensive quantum dynamics simulations.

In calculating quantitative values for hole mobilities to compare to experimental values, I have shown that it is now possible to use explicit quantum dynamical calculations to simulate charge carrier transport in large, realistic samples of disordered organic semiconductors. My results are in remarkably good agreement with those available from experiment and provide a molecular-scale picture of the nature of the charge carrier and the transport mechanism as a function of the crystallinity of the system. The notion that charge carrier transport in disordered systems occurs via small polaron hopping is

shown to be a reasonably good approximation only for fully amorphous systems - for semi-crystalline and crystalline samples significant charge carrier delocalisation occurs mandating the use of more advanced transport simulations, e.g. the FOB-SH method used here. In general, there is a good correlation between crystallinity, carrier delocalisation and mobility. Interestingly, we find that even relatively small amounts of structural disorder can lead to a significant drop in charge carrier delocalisation and hole mobility compared to the single crystal. This is an important consideration when comparing charge carrier mobilities in simulated organic systems, usually perfectly crystalline, with those of experiment, where it is difficult to prepare highly pure crystals devoid of defects. This approach is generally applicable to any molecular organic semiconductor and may be used for identifying new disordered materials with high charge mobility and help shape the design rules for creating such materials.

Finally, this study has served to highlight a potential drawback in the FOB-SH methodology as it currently stands. That is, the lack of electrostatic interactions within the simulations. These have not been implemented previously as the group's work was focussed on perfect crystals, where electrostatic interactions are not expected to affect the final result. However, in the more disordered systems this approximation may be a step too far. In the final chapter of this thesis, I will present my implementation of electrostatics within the surface hopping and a possible alternative to expensive Ewald summation.

## Chapter 5

# Extending surface hopping

FOB-SH is a variant of Tully's original fewest switches surface hopping<sup>34</sup>. It has been used to simulate electron-nuclear dynamics in large systems of organic molecules and has been well tested against experimental studies and benchmarked against higher order studies<sup>26,53,54,57,59–63</sup>. However, the FOB-SH code is currently very inefficient when electrostatic interactions are included. This presents a problem when looking at many systems, such as those with large amounts of disorder or those with polarisable molecules.

The standard Coulomb sum of partial charges is only conditionally convergent and extremely slow to calculate. The standard method for calculating electrostatic interactions is by decomposing interactions into long-range and short-range interactions (with corrections such as removing bonded terms etc...). This is normally carried out with an Ewald sum<sup>134</sup> where short-range interactions are calculated in real space and long-range interactions are calculated in reciprocal space. This results in two summations that are now unconditionally, quickly convergent. Further extensions to the standard Ewald technique provide an additional decrease in computational time by interpolating particles onto a grid and using fast fourier transforms to calculate all interactions. Although fast and formally exact, the Ewald sum has some major drawbacks in that it assumes a three dimensional periodicity and is often one of the most expensive parts of a molecular dynamics simulation<sup>135</sup>. In Wolf, 99<sup>136</sup>, a technique for removing the (expensive) reciprocal space term from the sum altogether was proposed by ensuring charge neutrality within a cutoff sphere from each atom. The idea was inspired from an observation

that: if the net sum of charges within the cutoff sphere was neutral then the standard coulomb sum seemed to converge well on accurate Madelung energies. This idea was developed to improve energy conservation and to remove discontinuities within the forces and energies<sup>137,138</sup>. In this work I will investigate the applicability of both the standard Ewald technique and a development of the Wolf method (named damped shifted forces (DSF)<sup>138</sup>) to calculate the electrostatic interactions within FOB-SH.

## 5.1 Implementation details: addition subtraction method

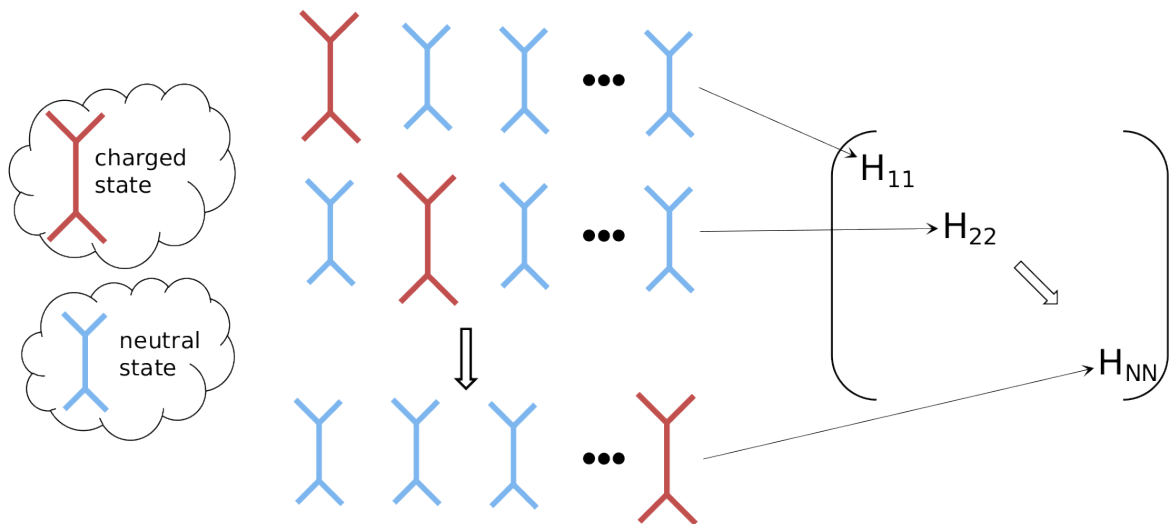


Figure 5.1: A demonstration of the procedure to calculate diagonal elements of the Hamiltonian (site-energies). Red (blue) shapes represent a molecule in its charged (neutral) state. A horizontal line of these shapes represent the full system with all molecules; where a single molecule is in its charged state. The arrow denotes which matrix element this saved as.

In FOB-SH, the electronic Hamiltonian is constructed such that the diagonal elements (site-energies) come from a classical forcefield and the off-diagonal elements (electron couplings) are estimated using the ultrafast atomic overlap method(AOM). These are proportional to the overlap of the diabatic wavefunctions. Each site-energy,  $H_{\gamma\gamma}$ , is defined as the potential energy of the system where the excess charge is localised on the molecule  $\gamma$ . For the avoidance of doubt, I will denote the molecule with the excess charge

localised on it as the ‘charged’ molecule and other molecules as ‘neutral’. The presence of the excess charge on molecule  $\gamma$  results in different input parameters (such as the charge distribution or the length of bonds) than the other neutral molecules. This results in the calculation of site-energies and forces having to be repeated  $N_{mol}$  times for each permutation of the charged molecule. This is summarised in figure 5.1.

To determine whether it is feasible to repeat the calculation of the electrostatic interactions  $N_{mol}$  times a quick timing run was carried out. This simulated two hundred and fifty pentacene molecules (nine thousand atoms) and the time was measured to calculate the electrostatic interactions with the three methods already implemented within CP2K: Smooth Particle Mesh Ewald (SPME), Particle Mesh Ewald (PME) and standard Ewald. The measured time of a simulation without any electrostatics was then subtracted from each of these simulations to isolate the time spent on just the electrostatics. The results are given in figure 5.2.

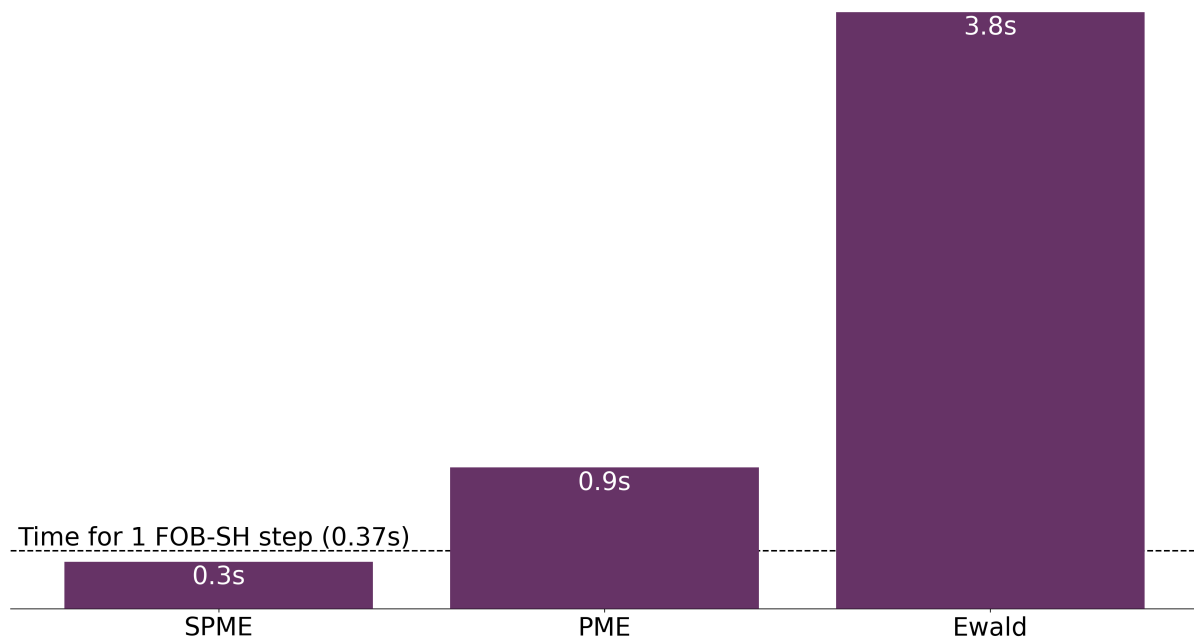


Figure 5.2: The time taken to calculate just the electrostatic interactions within CP2K for a nine thousand atom system using various methods. PME is particle mesh Ewald, SPME is smooth-PME, Ewald is the standard ewald method. The dashed line shows the time taken for a single FOB-SH step.

We can see that even a single calculation of the electrostatic interactions with the fastest

method available within CP2K (SPME) will take a length of time comparable to the rest of the surface hopping code. It is clear then that a more efficient method must be used to calculate the electrostatics.

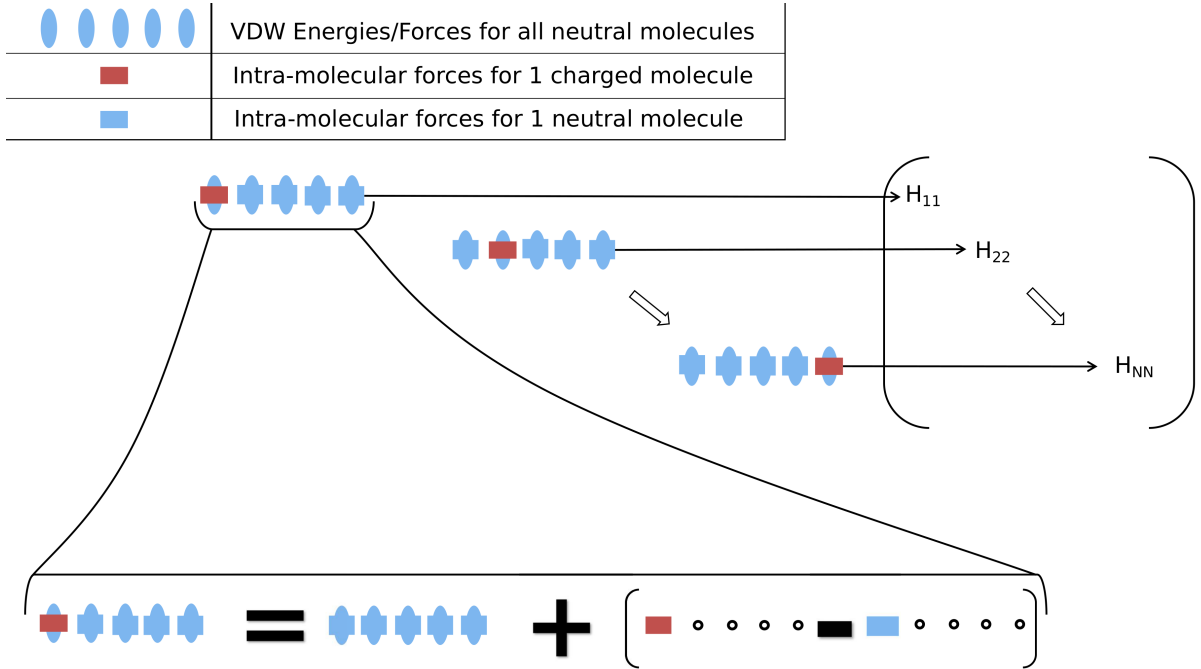


Figure 5.3: A depiction of the decomposition of the forces and energies within FOB-SH. First the all neutral VDW forces/energies are computed (blue ovals). Second the intra-molecular forces for each charged (neutral) molecule, represented by a red (blue) rectangle. The site-energy/force is then computed as a summation of all molecules in their neutral state with a molecule in its neutral state subtracted and the same molecule in its charged state added.

To calculate the intramolecular and Van der Waals energies and forces within the current FOB-SH implementation, the forces and energies consist of intra-molecular components (bonds, bends, torsions etc...) and inter-molecular components (Van der Waals forces provided by a Leonard-Jones potential). The same repetition of the calculation of forces and energies would, at first glance, be required for the correct calculation of these terms. However, an addition-subtraction scheme is used to reduce the calculation time from  $O(N_{mol}N_{atom}^2)$  to  $O(N_{atom}^2)$ . This is summarised in figure 5.3 and relies on the fact that the intra-molecular forces and energies can be decomposed into independent molecular contributions. In order to calculate the force on each atom and site-energy with molecule

$\gamma$  in its charged state the code first calculates the force/energy with all molecules in their neutral state and then adds the contribution of molecule  $\gamma$  in its charged state and subtracts the contribution of molecule  $\gamma$  in its neutral state. We do not make the same adjustment for the VDW forces as the difference is exactly zero if one assumes that VDW does not depend on the charge state (which is customary in force fields). This results in just two calculations of all forces and total energies rather than  $O(N_{mol})$  calculations. This scheme can be used because the intra-molecular forces can be naturally decomposed into discrete molecular contributions. That is, the calculation of the intra-molecular interactions are decoupled from their environment are independent of the charge state of all other molecules. The electrostatic interactions are, unfortunately, not so intuitively broken down. However, a similar trick can be used to reduce the cost of the Ewald sum. In the following work, I will present two frameworks in which to calculate electrostatic interactions: the recalculation method and the addition-subtraction method. The recalculation method references the method of naïvely looping over all molecules and recalculating energies and forces without optimisations. This would involve recalculating all interactions for every permutation of charged/neutral molecules. The addition-subtraction scheme is explained in the proceeding chapters.

### 5.1.1 Ewald Equations and the additional subtraction scheme

The standard Ewald summation for evaluating electrostatic energies in molecular dynamics simulation are given below:

$$\begin{aligned}
 E_{coul}(\mathbf{r}) = & \frac{1}{4\pi\epsilon_0} \sum_{\mathbf{n}}' \sum_{j=1}^{N_{at}^*} \sum_{i \neq j}^{N_{at}^*} q_i q_j \frac{\operatorname{erfc}(\alpha \cdot |\mathbf{r}_{ij} + \mathbf{n}|)}{|\mathbf{r}_{ij} + \mathbf{n}|} \Theta(r_{cut} - |\mathbf{r}_{ij} + \mathbf{n}|) \\
 & + \frac{4\pi}{V} \sum_{\mathbf{k} \neq 0} \frac{1}{|\mathbf{k}|^2} e^{-\frac{\pi^2 |\mathbf{k}|^2}{\alpha^2}} \left| \sum_{j=1}^{N_{at}^*} q_j e^{2\pi i \mathbf{k} \cdot \mathbf{R}_j} \right|^2 \\
 & - \frac{\alpha}{\sqrt{\pi}} \sum_j q_j^2 \\
 & - \sum_{(i,j) \in (1-Z \text{ list})} \left( E_{ij}^{1-2} + E_{ij}^{1-3} + (1-\zeta) E_{ij}^{1-4} \right)
 \end{aligned} \tag{5.1}$$

In equation (5.1), the first term is the real space sum. This sums over all periodic images ( $\mathbf{n}$ ) and pairs of atoms  $i, j$  within a cutoff imposed by the Heaviside step function

$\Theta(r_{cut} - |\mathbf{r}_{ij} + \mathbf{n}|)$ . The relative position vector between atoms is given by  $\mathbf{r}_{ij} = \mathbf{r}_i - \mathbf{r}_j$ , the charge on atom  $i$  is given by  $q_i$  and alpha is a convergence parameter. The \* symbol highlights that the loop should be over all non-bonded atoms. The second term is the most expensive part of this calculation and sums over reciprocal space vectors  $\mathbf{k}$  and atoms,  $j$ .  $\mathbf{R}_j$  represents the position vector of atom  $j$ . The third term is the constant self-energy term and the fourth corrects for bonded (intra-molecular) interactions. In the bonded correction  $E_{ij}^{1-Z} = \frac{1}{4\pi\epsilon_0} q_i q_j \frac{\text{erf}(\alpha \cdot |\mathbf{r}_{ij} + \mathbf{n}|)}{|\mathbf{r}_{ij} + \mathbf{n}|}$ . This removes the contribution of bonded interactions, which are accounted for by the intramolecular forcefield. These interactions are easily removed from the first term (real space sum) by simply not looping over the atoms, so this correction acts to amend the energy from the reciprocal space sum.

As these four summations are independent we can look at each one separately when implementing the addition-subtraction scheme, starting with the simplest, the self-energy term. Note in this section I will only discuss the energies; the forces are very similar and their equations are given in appendix L.

### 5.1.2 Self-energy addition subtraction scheme

The self energy term is a correction for over counting within the reciprocal space sum. For each site-energy,  $\gamma$ , we must recalculate the full forces and energies with the excess charge located on molecule  $\gamma$ . This is demonstrated in equation (5.2). Note that for brevity I have replaced the factor  $\frac{1}{4\pi\epsilon_0}$  with  $\eta$ .

$$E_{self}^{\gamma} = \frac{\alpha}{\sqrt{\pi}} \eta \left[ \sum_{j \notin \gamma} (q_j^n)^2 + \sum_{j \in \gamma} (q_j^c)^2 \right] \quad (5.2)$$

In the above equation, the Ewald self-energy correction contribution for site-energy  $\gamma$  is simply a sum of squared neutral state charges for atoms belonging to molecules that aren't  $\gamma$  plus the sum of squared charged state charges of atoms within  $\gamma$ . For clarity, the terms ‘neutral state charges’ and ‘charged state charges’ refer to charges with molecules parameterised in their neutral (no excess charge carrier) and charged (excess charge carrier localised on the molecule) state. This is represented by the superscript  $n$  and  $c$  where  $q_j^n$  represents the charge on atom  $j$  where the force-field for the molecule it belongs to

has been parameterised in its neutral state.  $q_j^c$  represents the charge on atom  $j$ , where the force-field for the molecule the atom belongs to has been parameterised in its charged state.

For a single molecular type system, this value is the same for all  $\gamma$  and no optimisations are required, except to calculate this value once and use it for each  $\gamma$ . However, for a more complex system the addition subtraction scheme used is given in equation (5.3).

$$E_{self}^\gamma = \eta \underbrace{\frac{\alpha}{\sqrt{\pi}} \sum_j^{N_{at}} (q_j^n)^2}_{\text{Calculated Once}} + \underbrace{\frac{\alpha}{\sqrt{\pi}} \eta \sum_{j \in \gamma} [(q_j^c)^2 - (q_j^n)^2]}_{\text{Calculated for each } \gamma} \quad (5.3)$$

In equation (5.3) we have removed the  $\gamma$  index from the most expensive part of the sum; this means we can calculate it once and store it. In the second term we only sum over atoms in charged molecule  $\gamma$  and remove the contribution from molecule  $\gamma$  in its neutral state and add the contribution from molecule  $\gamma$  in its charged state. Seeing as the correction part of equation (5.3) is the only part repeated from each  $\gamma$  this reduces the cost of this calculation from  $O(N_{mol}, N_{atom})$  to just  $O(N_{atom})$ . The same idea is used for the remaining terms in the Ewald sum.

### 5.1.3 Real space addition subtraction

The real space term is more complicated than the self-energy term, though the idea is the same. That is, the fully neutral contribution is calculated and for individual sites/molecules a correction is applied. This is shown in equation (5.4)

$$\begin{aligned} E_{real}^\gamma = & \eta \sum_{\mathbf{n}} \sum_j^{N_{at}} \sum_i^{N_{at}} q_i^n q_j^n R^{dir}(|\mathbf{r}_{ij} + \mathbf{n}|) \\ & + \eta \sum_{\mathbf{n}} \sum_{j \in \gamma, i \in \gamma} (q_j^c q_i^n - q_j^n q_i^n) R^{dir}(|\mathbf{r}_{ij} + \mathbf{n}|) \\ & + \eta \sum_{\mathbf{n}} \sum_{j \in \gamma, i \notin \gamma} (q_j^c - q_j^n) q_i^n R^{dir}(|\mathbf{r}_{ij} + \mathbf{n}|) \end{aligned} \quad (5.4)$$

In equation (5.4) the most expensive summation ( $O(N_{atom}^2)$ ) is the first term. Fortunately, we can once again calculate this once and use the same value for each site-energy. This first

term calculates all interactions between atoms belonging to molecules in their neutral state (interactions between molecules both in their neutral state). The next two terms show the addition-subtraction correction. The second term shows a sum over all pairs of atoms in the charged molecule,  $\gamma$ . In this term we subtract any interactions with both molecules in their neutral state and replace them with any charged-charged interactions. This scales as  $O(N_{\text{atom per mol}})$  and is repeated  $N_{\text{mol}}$  times so the full correction scales as  $O(N_{\text{atom}})$ . The third term replaces any interactions of atoms on the charged molecule with its environment (neutral molecules), hence it removes neutral-neutral interactions and replaces them with charged-neutral interactions. This scales as  $O(N_{\text{atom per mol}}, N_{\text{atom}})$  and is repeated  $N_{\text{mol}}$  times, resulting in an ultimate scaling of  $O(N_{\text{atom}}^2)$ . Therefore, this optimisation scales in the same manner as a single calculation of the Ewald interactions and any additional overheads will be minimal. For the avoidance of doubt, in equation (5.4) I have replaced the complementary error function and Heaviside step function in equation (5.1) with the term  $R^{dir}(|\mathbf{r} + \mathbf{n}|)$ , i.e.  $R^{dir}(|\mathbf{r}_{ij} + \mathbf{n}|) = \frac{\text{erfc}(\alpha \cdot |\mathbf{r}_{ij} + \mathbf{n}|)}{|\mathbf{r}_{ij} + \mathbf{n}|} \Theta(r_{cut} - |\mathbf{r}_{ij} + \mathbf{n}|)$

### 5.1.4 Bonded corrections addition subtraction

The bonded correction terms remove electrostatic contributions to energies (and forces) for atoms that are bonded. This is because interactions are already accounted for by the intra-molecular force-field (bonds, bends, torsions etc...). These interactions occur within molecules and their contribution can be decomposed into molecular contributions. These interactions can therefore be handled in the same way as the intra-molecular addition-subtraction scheme as discussed in section 5.1. The correction is given in equation (5.1) and just involves looping over atoms that are bonded and subtracting the coulomb energy and forces from the total.

### 5.1.5 Reciprocal space addition subtraction

The correction for the reciprocal space sum is given below in equation (5.5).

$$E_{recip}^\gamma = \frac{1}{2\pi V} \sum_{\mathbf{k} \neq 0} \frac{1}{|\mathbf{k}|^2} e^{\frac{\pi^2 |\mathbf{k}|^2}{\eta^2}} \left| \sum_j^{N_{at}} q_j^n e^{2\pi \mathbf{k} \cdot \mathbf{R}_j} + \sum_{j \in \gamma}^{N_{at}} (q_j^c - q_j^n) e^{2\pi \mathbf{k} \cdot \mathbf{R}_j} \right|^2 \quad (5.5)$$

The idea here is the same. The first term, looping over all neutral state charges, is calculated just once. The second term is then repeated for every state/molecule. This corrects term one which only includes interactions of neutral state molecules with neutral state molecules. This is done by adding the charged state contribution and subtracting the neutral state contribution.

The reciprocal energies can be optimised using the addition-subtraction technique. However, the forces cannot. I have given the equation for the forces below in (5.6)

$$\mathbf{F}_i^\gamma(\mathbf{R}) = \begin{cases} 4\pi q_i^C \sum_{\mathbf{k} \neq 0} \text{Im} [S'_\mathbf{k} E_{\mathbf{k},i}^*]; & i \in \gamma \\ 4\pi q_i^N \sum_{\mathbf{k} \neq 0} \text{Im} [S'_\mathbf{k} E_{\mathbf{k},i}^*]; & i \notin \gamma \end{cases} \quad (5.6)$$

Where:

- $S'_\mathbf{k} = A_\mathbf{k} \left[ \sum_j q_j^N E_{\mathbf{k},j} + \sum_{j \in \gamma} (q_j^C - q_j^N) E_{\mathbf{k},j} \right]$
- $A_\mathbf{k} = \frac{\mathbf{k}}{|\mathbf{k}|^2} e^{\frac{|\mathbf{k}|^2}{4\alpha^2}}$
- $E_{\mathbf{k},j} = e^{2\pi i \mathbf{k} \cdot \mathbf{R}_j}$

The calculation of this equation scales as  $\mathcal{O}(N^3)$  where  $N^3 = N_{\text{states}} N_{\text{atom}} N_k$ . This is because for every atom,  $i$ , in charged molecule,  $\gamma$ , a loop over  $\mathbf{k}$  vectors must be calculated.

This is a big problem for any implementation of Ewald electrostatics within surface hopping as the reciprocal space part of the Ewald sum is by far the most expensive part of the electrostatics calculation. In fact in the same two hundred and fifty molecule system as in figure 5.2 the reciprocal space component took eighty eight percent of the calculation time. In larger systems this increases. Repeating this calculation  $N_{\text{mol}}$  times would be far too slow and would limit the surface hopping code to small systems of tens of molecules. However, the damped shifted forces technique (DSF)<sup>138</sup> can be used to approximate the electrostatic interactions without the reciprocal force term.

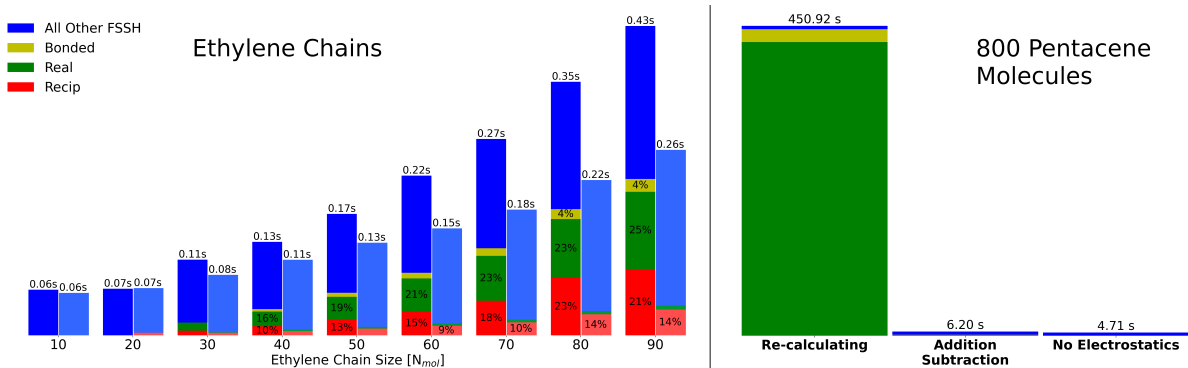


Figure 5.4: Time taken to run surface hopping and electrostatics for various lengths of one dimensional ethylene chain (left) and eight hundred molecule pentacene plane (right). Darker colors show data from the recalculation method for the electrostatics and less saturated colors to the right show data from the addition subtraction scheme. Green bars show the time taken to calculate real space interactions, red is reciprocal, yellow is the bonded corrections and blue shows all other parts of the surface hopping code. In the right pane reciprocal interactions are omitted as they took too long to run.

## 5.2 Timing the electrostatics implementation

In figure 5.4 the time taken for a single step of a surface hopping simulation for various lengths of a one dimensional ethylene chain can be seen (left panel). We see as the chain size increases it becomes more important that electrostatic interactions are efficiently handled. In fact for just a ninety molecule ethylene chain calculating the electrostatics takes longer than all other parts of surface hopping. On the right of the same figure, timings for a eight hundred molecule pentacene plane are shown. In these simulations, the reciprocal calculations took far too long and had to be turned off to measure the time taken for the other components. In this panel we see the significant speed-up for larger system sizes when using the addition-subtraction scheme. However, even with the addition-subtraction scheme the full reciprocal space calculations still take far too long. This is because the calculation of the forces are still repeated  $N_{mol}$  times as they cannot be optimised in the same way. A small speedup is seen due to the addition-subtraction scheme being used with the reciprocal space energies. However, we see that the addition-subtraction scheme offers a major speedup for all other components. It is, of course, also vital that the results outputted are correct. I have tested both the recalculation method and the addition-subtraction method against standard CP2K calculations to ensure the

implementation is correct. In the following section I will present results only for the addition-subtraction scheme although the re-calculation method was tested in the same way.

### 5.2.1 Testing the electrostatics implementation

To test the calculation of site-energies and forces within CP2K a ten molecule ethylene chain was used. In order to produce reference data the new implementation could be checked against, classical MD in CP2K was used to calculate the site-energies and forces for ten different system. In each one of these simulations a different molecule was chosen to have charged geometry and the rest were chosen to have neutral geometry in the input files. A single step of MD was then carried out and forces and energies were outputted. These forces and energies were subsequently compared to the forces and energies outputted by the both the recalculation and addition-subtraction method. The results for the tests of the addition-subtraction method are shown in figure 5.5. We see in figure

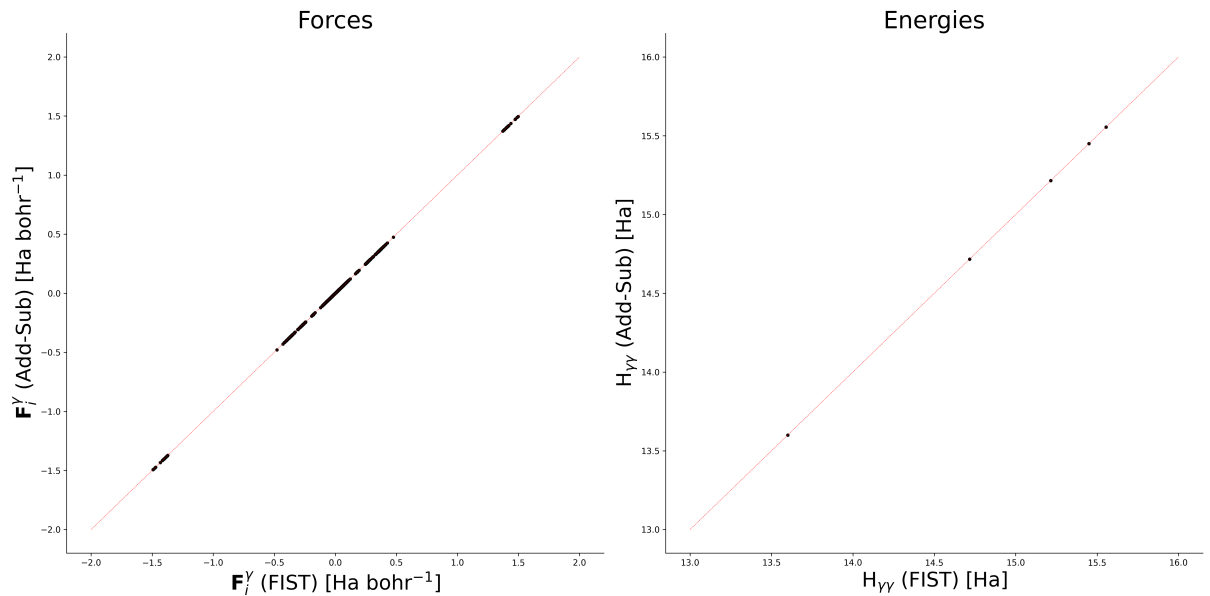


Figure 5.5: A comparison of forces and energies calculated with multiple classical MD simulations (x-axis) and the addition-subtraction method with Ewald electrostatics. The left pane shows the magnitude of the outputted forces and the right the outputted potential energies. Black dots show values from each atom and timestep. The red dashed line shows  $y = x$  and serves as a guide for the eye.

5.5 that the values of energy and forces as calculated with CP2K's standard MD package (FIST) and my implementation of the addition-subtraction method are exactly the same.

In fact the maximum absolute difference between results was  $5 \times 10^{-13}$  i.e. numerical noise. This confirms the implementation of the addition-subtraction scheme. It should be noted that the values for the forces and energies are rather large. This is due to the ethylene system used not being equilibrated. The system was created by placing ten ethylene molecules in a line with a two Angstrom spacing. As this test wasn't a test of the physics of the system but the implementation of the equations it does not matter that the system was quite unphysical.

To further benchmark the addition-subtraction scheme the same input parameters were fed into the code using the recalculation method and the addition-subtraction method. FOB-SH was then run for two hundred timesteps with various system sizes. These ranged from an ethylene dimer to one hundred molecule ethylene system. A small ten molecule pentacene system was also simulated. In order to check for correct output the tool ‘diff’ was used. This checks for differences in files and reports any discrepancies. Using this tool only numerical noise was picked up (errors with a magnitude less than  $10^{-12}$ ). This serves as a further validation of the equations for the addition-subtraction scheme and its implementation within CP2K. However, as it is currently implemented it doesn't provide a sufficient speed up for realistic applications (hundreds or thousands of molecules), due to high reciprocal space force costs. To optimise the electrostatic calculations further the DSF<sup>138</sup> method was investigated, as explained in the following section.

### 5.2.2 DSF

The damped shifted force (DSF) method relies on the observation by Wolf et al<sup>136</sup> that electrostatic interactions are essentially short-ranged (in condensed phase systems). However, in order to converge the real space sum within a cutoff, image charges must be used to ensure charge neutrality within the cutoff sphere. Initially, Wolf et al ensured charge neutrality by placing image charges on the surface off the cutoff sphere. However, this lead to discontinuities in the force at the cutoff radius and poor energy conservation. To fix this Fennel et al (building on the work of Zahn et al) proposed the damped shifted forces technique. The potential and force equations are given below in equations (5.7) and (5.8). In these equations I have replaced the notation for the magnitude of the displacement

vector,  $|\mathbf{r}_{ij} + \mathbf{n}|$ , with  $r_{ij}$  for clarity.

$$V_{DSF}(r) = q_i q_j \left[ \frac{\operatorname{erfc}(\alpha r_{ij})}{r_{ij}} - \frac{\operatorname{erfc}(\alpha R_c)}{R_c} + \left( \frac{\operatorname{erfc}(\alpha R_c)}{R_c^2} + \frac{2\alpha e^{-\alpha^2 R_c^2}}{\sqrt{\pi} R_c} \right) (r_{ij} - R_c) \right], (r_{ij} < R_c) \quad (5.7)$$

$$\mathbf{F}_{DSF}(r) = q_i q_j \left[ \left( \frac{\operatorname{erfc}(\alpha r_{ij})}{r_{ij}^2} + \frac{2\alpha e^{-\alpha^2 r_{ij}^2}}{\sqrt{\pi} r_{ij}} \right) - \left( \frac{\operatorname{erfc}(\alpha R_c)}{R_c^2} + \frac{2\alpha e^{-\alpha^2 R_c^2}}{\sqrt{\pi} R_c} \right) \right] \hat{\mathbf{r}}_{ij}, (r_{ij} < R_c) \quad (5.8)$$

In equation (5.7) above the first term is the same as in the standard Ewald equation and is equivalent to the original coulomb potential, damped by the complementary error function. The second term is to ensure that the potential goes to zero at the cutoff radius (i.e.  $r_{ij} = R_c$ ). The third term, in parentheses, ensures that the derivative of the potential (the force) continuously becomes zero at the cutoff radius. Fortunately, the implementation only involves altering the standard Ewald sum by omitting the reciprocal space, self terms and the bonding correction and amending the real space term. Importantly, this method is fully compatible with the addition-subtraction scheme and can provide a significant speedup to the calculation of the electrostatic interactions. The addition-subtraction scheme equation is the same as for the real space part of the Ewald equations and is given in equation (5.4) where  $R^{dir}$  is given by the term in brackets in equation (5.7). The DSF method replaces the full Ewald sum.

## 5.3 Testing DSF

### 5.3.1 Classical MD

In order to validate the DSF implementation various tests were carried out. Firstly, each electrostatic interaction was calculated by hand for a toy carbon monoxide dimer, without periodicity. Charges of +1/-1 were chosen for the oxygen and carbon atoms respectively and each molecule was placed four angstroms apart in the y dimension. In this system there are only three unique interactions to calculate: C-C, C-O and O-O. The calculated value within the code was compared with the hand-calculated value as well as total energies and forces printed after each step. When the code had passed this test a

comparison to Ewald electrostatics was made.

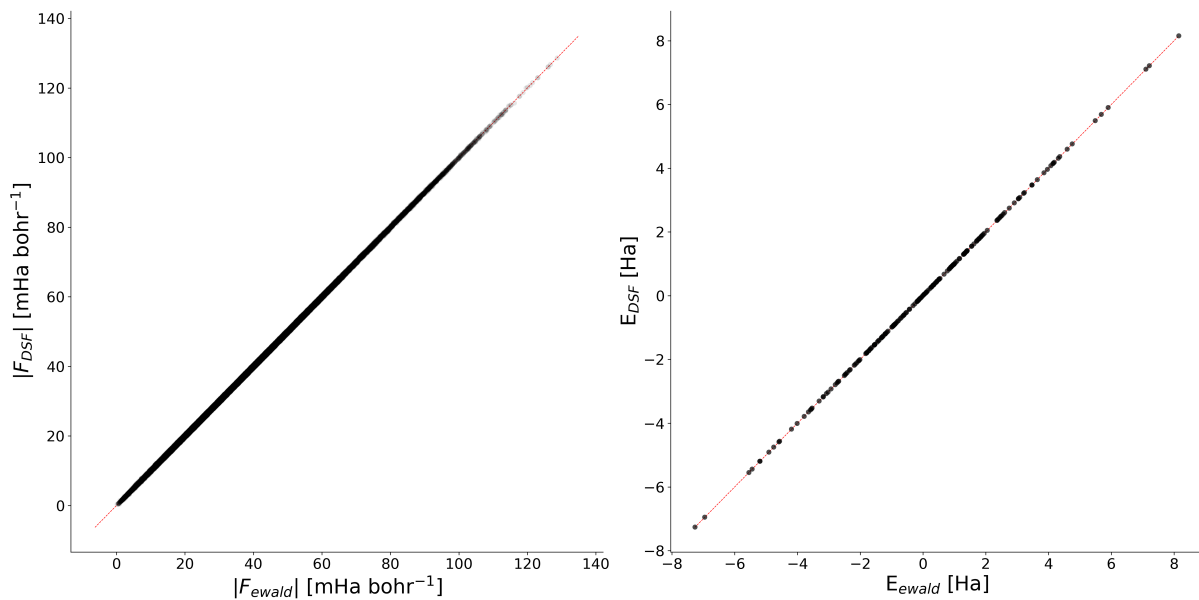


Figure 5.6: Comparison of Ewald and DSF forces and energies. The x-axis shows results from Ewald simulations and the y-axis shows results from DSF simulations. The left pane shows the force magnitude with black dots representing values from all atoms at all timesteps. The right pane shows potential energies from each timestep. The red line shows the line  $y=x$  and is a guide for the eye.

In order to carry out a comparison to Ewald electrostatics, a small pentacene crystal was constructed, containing one hundred and twenty eight molecules. The standard triclinic pentacene unit cell was taken from the Cambridge Structural Database<sup>139</sup> and the same forcefield parameters were used as in section 4. All molecules were in their neutral state (without an excess charge carrier). A 1ps classical molecular dynamics simulation was then performed with full Ewald electrostatics and positions and velocities were printed every 5fs. Two hundred separate simulations using DSF electrostatics were then performed using the printed geometries from the Ewald simulations. In these simulations an alpha of 0.0 and cutoff radius of twelve Angstrom was used. These were chosen as in Fennel, 06<sup>138</sup> as these values gave good results when compared to Ewald electrostatics. It is important to note that in this work the effect of the cutoff radius and the damping coefficient,  $\alpha$ , have not been investigated. The outputted energies and forces were subsequently compared and the RMSE was found for the difference between the Ewald and

DSF simulations. Care was taken to shift both the Ewald and DSF energies by their mean value to correct for a different energy offset in their values. In order to put this RMSD in context, a further simulation was carried out without any electrostatic interactions on the outputted Ewald geometries. The energies and forces of this simulation were then subtracted from the Ewald energies and forces to isolate just the electrostatic interactions. The root mean squared fluctuations (RMSF) of just the electrostatic energies and forces were then calculated in order to quantify the error that DSF introduces. The root mean squared fluctuations of the Ewald electrostatic energies were calculated to be: 120.0 mHa and the root mean squared error in the DSF potential compared to the Ewald potential was calculated to be: 9.49 mHa. The root mean squared fluctuations of the Ewald electrostatic forces were calculated to be: 1.44 mHa bohr<sup>-1</sup> and the root mean squared error of DSF forces compared to Ewald forces were calculated to be: 0.13 mHa bohr<sup>-1</sup>. These results show my implementation of DSF within CP2K to introduce an error of approximately eight to ten percent within the energies and forces. Further, we see in figure 5.6 the magnitude of each Ewald and DSF force and each energy compared directly. When the coefficient of determination,  $R^2$ , is calculated for these data sets we get: 1.000 for the energies and forces, very similar values to the ones reported in Fennel, 06.

As a final check of the equations the damping coefficient was set to a very large value (ten thousand) and each DSF interaction between pairs of atoms was printed. This was to confirm that, in the limit of an infinite  $\alpha$  coefficient, DSF electrostatic contributions to the energies and forces tended to zero.

### 5.3.2 Surface Hopping

Although, in surface hopping, the DSF equations are exactly the same the way that they are applied is quite different (as explained in 5.1). In order to test the DSF implementation in the surface hopping code the same two tests were run as in the classical code. The first was to compare each force and site-energy calculated using DSF with the addition-subtraction method to forces and site-energies calculated with  $N_{mol}$  different topology files. The second was to compare the surface hopping DSF implementation with the already tested surface-hopping Ewald implementation.

### 5.3.2.1 Multiple Topology Files

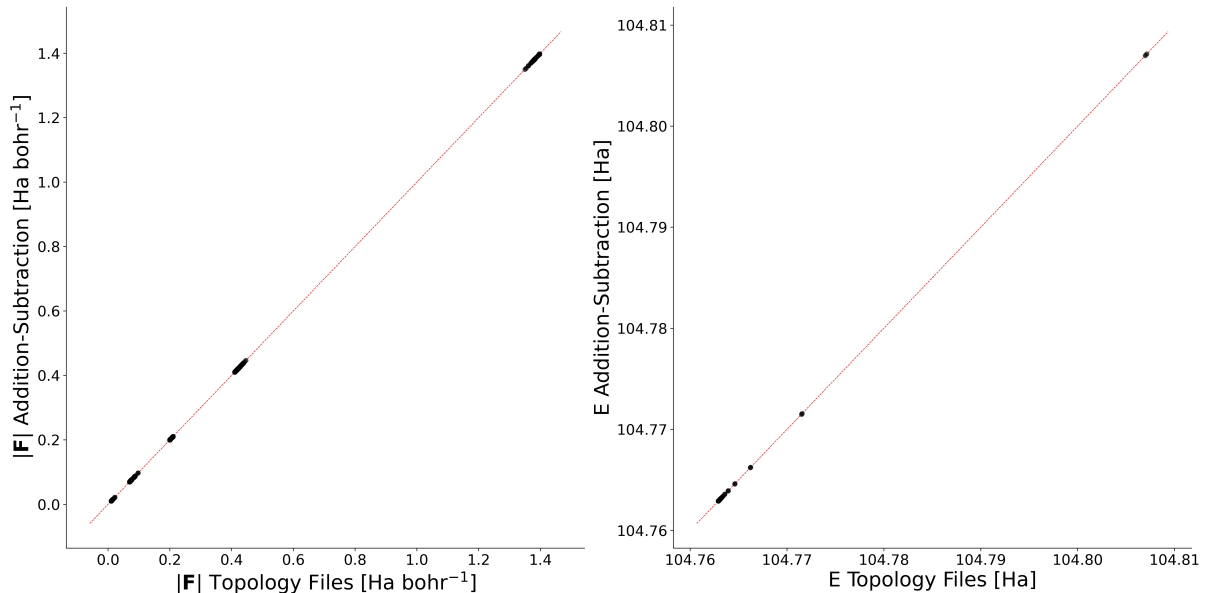


Figure 5.7: Comparison of DSF forces and energies using multiple topology files (x axis) and classical MD and using the addition-subtraction scheme within SH (y axis). The left pane shows the force magnitude with black dots representing values from all atoms at all timesteps. The right pane shows potential energies from each timestep. The red line shows the line  $y=x$  and serves as a guide for the eye.

As in section 5.2.1, the site-energies and forces for each permutation of the charged molecule were calculated by running N CP2K simulations. In each simulation, the inputted topology had a different molecule in the charged state and all the others in the neutral state. A one hundred molecule ethylene system was used and one hundred different simulations were run to get each site-energy and force (using DSF electrostatics). The forces and energies were outputted and used to compare to the forces and energies outputted from the surface hopping simulation using the addition subtraction scheme with DSF electrostatics. The results can be seen in figure 5.7. The maximum absolute difference in the outputted values was less than  $10^{-13}$  confirming the implementation of DSF with the addition-subtraction scheme in surface hopping.

### 5.3.2.2 Comparison to Ewald

The comparison to Ewald electrostatics was carried out as in 5.3.1. That is, a surface hopping simulation was carried out with a small pentacene crystal and Ewald electrostatics. Positions and velocities were printed out periodically and DSF electrostatics

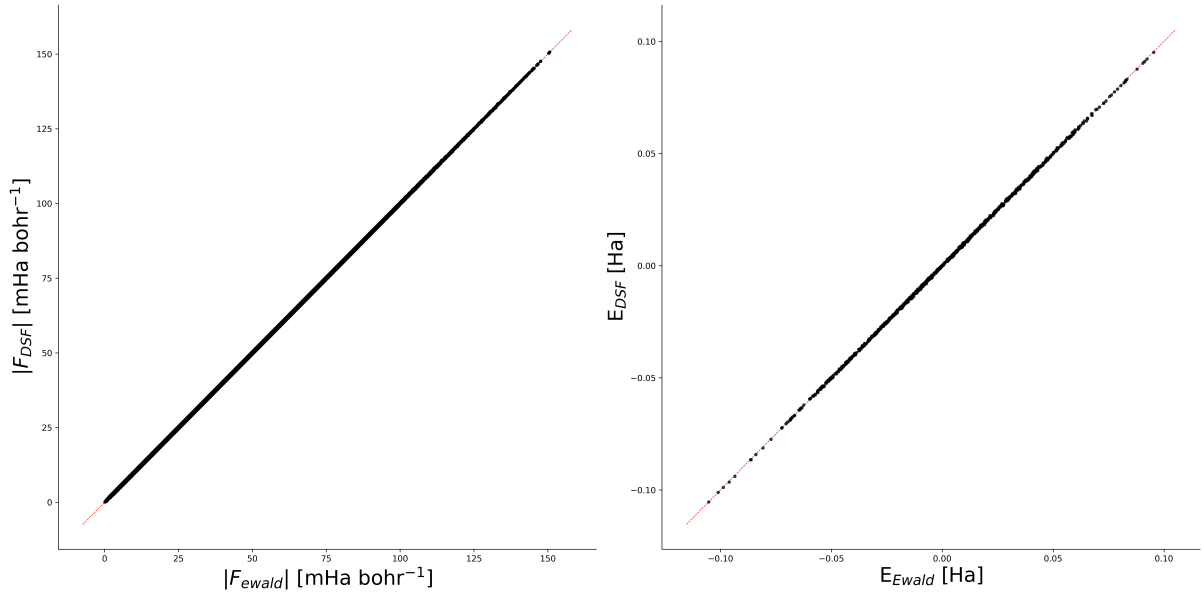


Figure 5.8: A comparison of energies and forces as calculated by full Ewald and DSF electrostatics.

was then run using each of the position and velocity files as initial geometries. A cutoff radius of fifteen Angstrom and damping coefficient of  $0.0\text{bohr}^{-1}$  was used. Forces and energies were then compared and the root mean squared deviation between Ewald and DSF was calculated. The system was a fifty four molecule pentacene crystal that had been equilibrated with classical MD using SPME as the electrostatic calculator, until the temperature and total energy had converged. The results are shown in figure 5.8.

The results, reflect very well the findings from figure 5.6. This is to be expected as the same equations are being used. We see in both the forces and the energies that there is very little deviation of values with respect to full Ewald simulations at every timestep. In fact, the  $R^2$  value is 1.000 for both datasets. As before the RMSF of the electrostatic energies and forces were calculated. These are 5.61 mHa and 0.60 mHa  $\text{bohr}^{-1}$ . The RMSE in the DSF electrostatics (compared to Ewald) was: 0.31 mHa and 0.08 mHa  $\text{bohr}^{-1}$  for the total potential energy and forces respectively. This validates my implementation of DSF within surface hopping against my implementation of Ewald electrostatics. Further the Ewald implementation has been validated against classical MD and has been shown to reproduce the energies and forces exactly. Satisfied that the

DSF implementation is working, in the following section, I will briefly show the speed up achieved by using DSF instead of Ewald electrostatics before final concluding remarks.

## 5.4 Timing DSF

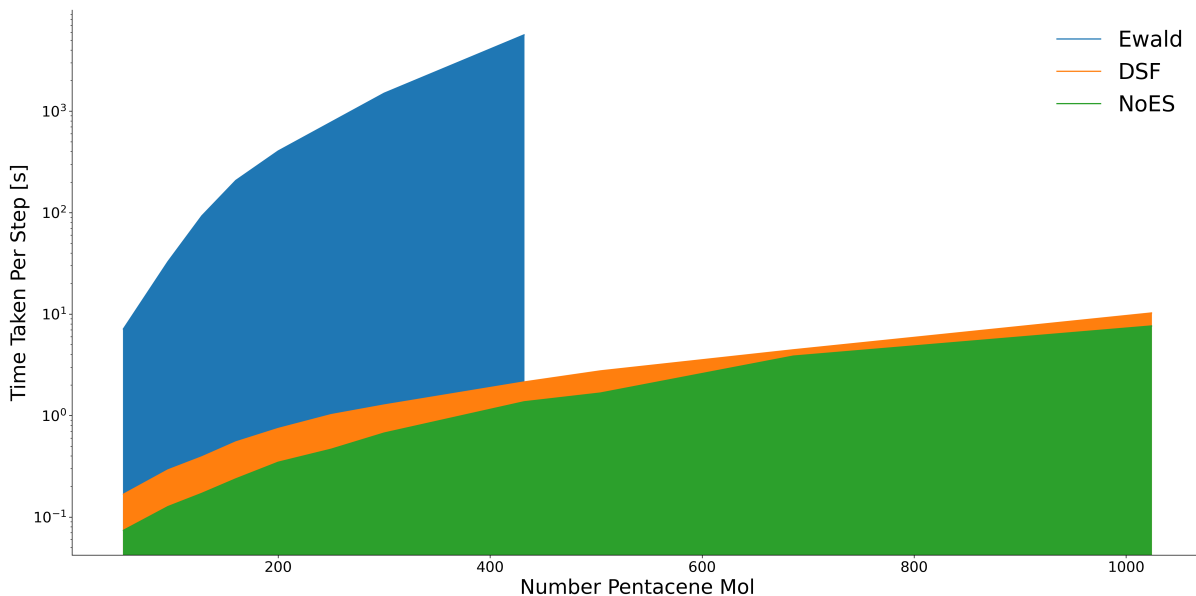


Figure 5.9: Timing data on the DSF implementation compared to Ewald electrostatics and FOB-SH without any electrostatics. The blue curve shows Ewald timing data, the orange is DSF and green is without any electrostatics.

The DSF technique has been shown to give values for electrostatic energies and forces that very closely resemble Ewald electrostatics. However, if it does not provide a speedup to the code it has no use. In order to quantify the difference in time taken to calculate electrostatic interactions, I have ran a variety of simulations using Ewald electrostatics and DSF electrostatics in surface hopping and shown the results in figure 5.9. In this figure we can clearly see that the DSF electrostatics results in a significant speedup of the Ewald code. At approximately fifty molecules calculating Ewald electrostatics (even with the addition-subtraction scheme) takes ten seconds per step. This would take approximately 2.3 days to simulate 1 ps, assuming a standard timestep of 0.05fs. This is because the reciprocal forces (forces calculated in reciprocal space in the Ewald sum) cannot be optimised with the addition-subtraction scheme. In contrast, if using DSF a single step would take around 0.08s and simulating 1ps would take less than thirty minutes. The filled orange shape shows the overhead that just the electrostatic calculations

introduce compared to without electrostatics. The filled blue shape shows (slightly less than) the overhead that Ewald electrostatics introduces. We see in larger systems, such as the four hundred and thirty two molecule system calculating the electrostatic interactions alone takes more than one hour per step, the rest of the surface hopping code only requires around one second. This figure shows that using DSF electrostatics (with the addition-subtraction scheme) will allow simulation of around one thousand molecules in a reasonable time-frame.

## 5.5 Conclusions

In this chapter I have presented an extension to the surface hopping code, namely the implementation of electrostatic interactions. I have tested and timed my implementation of the standard Ewald summation technique and the damped shifted forces (DSF) method. I have discussed the limitations in the standard Ewald technique, i.e. far too costly for large systems and discussed how these can be mitigated with the DSF method. Due to the way the Hamiltonian is constructed in FOB-SH, each diagonal element (site-energy) is calculated by calculating all forces and energies. There are  $N_{mol}$  site-energies leading to a scaling in CPU time of  $O(N_{mol}N_{atom}^2)$ . However, the use of an addition-subtraction scheme has been shown to successfully reduce this by an order of magnitude ( $N_{mol}$ ), allowing the simulation of large systems requiring the proper account of electrostatic interactions (such as polar systems or highly disordered ones). However, this addition-subtraction scheme cannot be applied to the reciprocal space forces in the Ewald summation. For this reason, DSF has been implemented to provide a reasonable estimate of full Ewald forces and energies. In the systems tested in this chapter the error produced by DSF was around eight to ten percent compared with Ewald electrostatics. Although with appropriate tuning of input parameters this may be reduced even further. An investigation of the parameters has not been carried out in this work due to time constraints, though should be a relatively straightforward task. Importantly, the use of the DSF technique in calculating electrostatic interactions has been shown to add very little overhead to the bare surface hopping code. Using a one thousand and twenty four molecule pentacene system the time taken per step increases from 7.5 seconds to 10.5 seconds without and

with DSF electrostatics respectively.

The results in this chapter report a very promising start to the generalisation of the FOB-SH code to systems requiring electrostatic interactions. However, more work should be done to further test both the effect of parameters  $\alpha$  and  $R_{cut}$ , and to compare outputted physical properties such as electronic populations and system structure to a reference system. This could mean simulating small three dimensional structures with both Ewald electrostatics and DSF and comparing structures and mobilities. Further, it would be interesting to apply the DSF enabled FOB-SH code to the amorphous and crystalline structures from the previous chapter and to observe their effect on charge trapping -especially in interfacial regions.

## Chapter 6

# General Conclusions and Outlook

Although nonadiabatic chemistry dictates many of life's vital processes, such as photosynthesis, electron transfer, and light detection<sup>140</sup>, the complexity of the underlying physics has meant simulating such systems is relatively novel. Electron transfer has been of particular interest in this work, specifically the transport of electrons or electron-holes within organic semiconductors. In this field, a useful quantity of merit is the charge carrier mobility. That is, how quickly charge moves within a system as a response to an electric field. In organic semiconductors, the most common tool for simulating charge carrier mobilities is the Marcus's master rate equation (typically used coupled with a Monte-Carlo method). Although this is used in many studies<sup>141-148</sup>, the validity of the application of the Marcus rate to organic semiconducting systems is often disputed, due to an often large quantum delocalisation of the electron wavefunction. However, the quantum delocalisation isn't sufficient to warrant band theory calculations either. To fill this gap, nonadiabatic molecular dynamics techniques such as surface hopping, Ehrenfest and CTMQC have been developed. This work has been concerned with the further development of these techniques and their application to simulations of charge transfer.

In the first two chapters my implementation of the new CTMQC technique was discussed. However, there is still some way to go before its widespread adoption as an alternative to surface hopping. CTMQC's main advantage is that it has been derived from first principles and claims to rigorously handle the overcoherence problem that has hampered surface hopping. While it is true that CTMQC performs very well on simple one dimen-

sional Tully model systems, even reproducing exact quantum dynamics correctly (given correct parameterisation), it is let down by two key problems. First, is its instability when applied to even moderately complex molecular systems. Second, is the necessity to parameterise the quantum momentum to achieve accurate decoherence. In order to solve these problems a new way to construct the nuclear density may be required, leading to a new equation for calculating the quantum momentum. Perhaps further studies on two or three dimensional generalisations of the Tully models or single molecular systems may also help shed light on the algorithm. Finally, in order to be a true rival of the surface hopping technique, effort must be spent on finding efficiencies in its implementation. I have presented the CTMQC equations within the FOB-SH framework, where diabatic expansion coefficients are propagated rather than their adiabatic counterparts. However, two key quantities: the quantum momentum and the adiabatic momentum terms, still require the calculation of adiabatic quantities such as the spatial derivative of the adiabatic energies which leads to a major increase in computational time. Perhaps a re-derivation in the diabatic basis would lead to increased performance and maybe even more stable propagation.

Another nonadiabatic molecular dynamics (NAMD) technique studied in this work is fewest switches surface hopping, namely fragment orbital-based surface hopping (FOB-SH). This is a tried and tested method developed by multiple past and present members of the group and is able to simulate large systems, often within experimental accuracy. In this work I've applied FOB-SH to an disordered pentacene systems, created by a melt-quench technique with various quench times. This study is one of the first (to the author's knowledge) to simulate structures with such a wide spectrum of disorder. This presented a unique opportunity to showcase FOB-SH's ability and to compare hole-mobilities spanning several orders of magnitude to experiment. At both ends of the spectrum, experimental mobilities agreed well with the simulated results. However, the amorphous values were on the high end of a wide spread of experimental results. This is thought to be due to the lack of electrostatic interactions within FOB-SH. While this isn't thought to have a significant effect on hole mobilities within highly ordered crystals it will within much more disordered amorphous systems and at crystal interfaces. For

this reason, I have implemented and tested two electrostatics methods within FOB-SH. The first, full Ewald, is a representation of the coulomb sum, with long range interactions calculated in reciprocal space and short range interactions calculated in real space. The second, DSF, is an approximation to Ewald electrostatics derived by simply omitting the long range interactions and ensuring net charge-neutrality within a cutoff sphere with the use of virtual charges. I found that, although the Ewald sum is exact, it is far too expensive to use in realistic simulations and DSF must be used instead. Though not thoroughly tested, initial results are very promising and pave the way for a new class of materials to be studied.

## Appendix A

### Tully Model Paramters

#### A.1 Model 1 -Single Avoided Crossing

	Quantity	Value	Unit
Hamiltonian Paramters:			
$H_{11}(\mathbf{R}) = A \tanh(B\mathbf{R})$	Initial Position	-20	a.u.
$H_{12}(\mathbf{R}) = Ce^{-D\mathbf{R}^2}$	Initial Velocities	15.0, 25.0	a.u.
$H_{21}(\mathbf{R}) = H_{12}(\mathbf{R})$	Initial Adiab Pop	ground state	-
$H_{22}(\mathbf{R}) = -H_{11}(\mathbf{R})$	Simulation Time	6000, 4000	a.u.
Where $A = 0.03$ , $B = 0.4$ , $C = 0.005$ and $D = 0.3$	$\sigma_v^{(I)}$	0.5	a.u.
	M ( $\sigma$ constant)	40	-
	$\Delta t_{\text{nuclear}}$	0.1	fs
	$\Delta t_{\text{electronic}}$	0.01	fs
	$\frac{\delta \mathbf{R}_{lk,v}^{(I)}}{\delta t}$ threshold	0.15	a.u.
	$N_{rep}$	200	-

## A.2 Model 2 -Dual Avoided Crossing

	Quantity	Value	Unit
Hamiltonian Paramters:			
$H_{11}(\mathbf{R}) = 0$	Initial Position	-8	a.u.
$H_{12}(\mathbf{R}) = Ce^{-D\mathbf{R}^2}$	Initial Velocities	16.0, 30.0	a.u.
$H_{21}(\mathbf{R}) = H_{12}(\mathbf{R})$	Initial Adiab Pop	ground state	-
$H_{22}(\mathbf{R}) = -Ae^{-B\mathbf{R}^2} + E$	Simulation Time	2500, 1500	a.u.
Where A = 0.1, B = 0.28, C = 0.015, D = 0.06 and E = 0.05	$\sigma_v^{(I)}$	0.5	a.u.
	M ( $\sigma$ constant)	40	-
	$\Delta t_{\text{nuclear}}$	0.1	fs
	$\Delta t_{\text{electronic}}$	0.01	fs
	$\frac{\delta \mathbf{R}_{ik,v}^{(I)}}{\delta t}$ threshold	0.15	a.u.
	$N_{rep}$	200	-

## A.3 Model 3 -Extended Coupling

	Quantity	Value	Unit
Hamiltonian Paramters:			
$H_{11}(\mathbf{R}) = A$	Initial Position	-15	a.u.
$H_{12}(\mathbf{R}) = \begin{cases} Be^{C\mathbf{R}}, & R \leq 0 \\ B(2 - e^{-C\mathbf{R}}), & R > 0 \end{cases}$	Initial Velocities	10, 30	a.u.
$H_{21}(\mathbf{R}) = H_{12}(\mathbf{R})$	Initial Adiab Pop	ground state	-
$H_{22}(\mathbf{R}) = -H_{11}(\mathbf{R})$	Simulation Time	5000, 1500	a.u.
Where A = $6 \times 10^{-4}$ , B = 0.1 and C = 0.9	$\sigma_v^{(I)}$	0.5	a.u.
	M ( $\sigma$ constant)	40	-
	$\Delta t_{\text{nuclear}}$	0.1	fs
	$\Delta t_{\text{electronic}}$	0.01	fs
	$\frac{\delta \mathbf{R}_{ik,v}^{(I)}}{\delta t}$ threshold	0.15	a.u.
	$N_{rep}$	200	-

## A.4 Model 4 -Dual Arch

Hamiltonian Paramters:

$$H_{11}(\mathbf{R}) = A$$

$$H_{12}(\mathbf{R}) = \begin{cases} B \left[ -e^{C(\mathbf{R}-D)} + e^{C(\mathbf{R}+D)} \right] & R \leq -D \\ B \left[ e^{-C(\mathbf{R}-D)} - e^{-C(\mathbf{R}+D)} \right] & R \geq D \\ B \left[ 2 - e^{C(\mathbf{R}-D)} - e^{-C(\mathbf{R}+D)} \right] & -D < R < D \end{cases}$$

$$H_{21}(\mathbf{R}) = H_{12}(\mathbf{R})$$

$$H_{22}(\mathbf{R}) = -H_{11}(\mathbf{R})$$

Where  $A = 6 \times 10^{-4}$ ,  $B = 0.1$ ,  $C = 0.9$  and

$$D = 4$$

Quantity	Value	Unit
Initial Position	-20	a.u.
Initial Velocities	10, 40	a.u.
Initial Adiab Pop	ground state	-
Simulation Time	6000, 2000	a.u.
$\sigma_v^{(I)}$	0.5	a.u.
M ( $\sigma$ constant)	40	-
$\Delta t_{\text{nuclear}}$	0.1	fs
$\Delta t_{\text{electonic}}$	0.01	fs
$\frac{\delta \mathbf{R}_{lk,v}^{(I)}}{\delta t}$ threshold	0.15	a.u.
$N_{rep}$	200	-

## Appendix B

# Wigner Distribution Derivation

The nuclear wavepacket (at time 0) is given by:

$$\chi(R) = \frac{1}{(\pi\mu^2)^{\frac{1}{4}}} e^{-\frac{(R-R_0)^2}{2\mu^2} + ik_0(R-R_0)} \quad (\text{B.1})$$

The Wigner quasiprobability function for momentum and position ( $p, R$ ) is given by:

$$W(p, R) = \frac{1}{\pi\hbar} \int_{-\infty}^{\infty} \chi^*(R+y)\chi(R-y)e^{\frac{2ipy}{\hbar}} dy \quad (\text{B.2})$$

However, both Ehrenfest and CTMQC require atomic positions as input so we must extract the position and velocity probability densities from this. We get these from the marginal integrals of the Wigner distribution i.e.

$$|f(R)|^2 = \int_{-\infty}^{\infty} W(R, p) dp \quad (\text{B.3})$$

$$|f(p)|^2 = \int_{-\infty}^{\infty} W(R, p) dR \quad (\text{B.4})$$

In order to calculate these marginal integrals we must first crunch through the maths of equation (B.2). Substituting eq (B.1) into (B.2):

$$W(p, R) = \frac{1}{\pi\hbar} \int_{-\infty}^{\infty} \frac{1}{\mu\sqrt{\pi}} e^{-\frac{(R+y-R_0)^2}{2\mu^2} - 2ik_0y - \frac{(R-y-R_0)^2}{2\mu^2}} e^{\frac{2ipy}{\hbar}} dy \quad (\text{B.5})$$

Simplifying the 2 quadratic equations (equation (B.5)) we get:

$$W(p, R) = \frac{1}{\pi \hbar} \int_{-\infty}^{\infty} \frac{1}{\mu \sqrt{\pi}} e^{-\mu^{-2}(y^2 - 2ik_0 y \mu^2 + (R-R_0)^2)} e^{\frac{2ipy}{\hbar}} dy \quad (\text{B.6})$$

We can now take the expressions not dependant on  $y$  outside of the integral and combine the exponents.

$$W(p, R) = \frac{1}{\pi \sqrt{\pi} \mu \hbar} e^{-\frac{(R-R_0)^2}{\mu^2}} \int_{-\infty}^{\infty} e^{-\frac{y^2 + 2iy\mu^2(\frac{p}{\hbar} - k_0)}{\mu^2}} dy \quad (\text{B.7})$$

Integrating we get:

$$\int e^{-\frac{y^2 + 2iy\mu^2(\frac{p}{\hbar} - k_0)}{\mu^2}} dy = \frac{\sqrt{\pi} \mu}{2} e^{-\frac{\mu^2}{\hbar^2}(p - \hbar k_0)^2} \operatorname{erf} \left[ \frac{y}{\mu} + i \left( \frac{p\mu}{\hbar} - \mu k_0 \right) \right] \quad (\text{B.8})$$

Applying limits we get:

$$\int_{-\infty}^{\infty} e^{-\frac{y^2 + 2iy\mu^2(\frac{p}{\hbar} - k_0)}{\mu^2}} dy = \sqrt{\pi} \mu e^{-\frac{\mu^2}{\hbar^2}(p - \hbar k_0)^2} \quad (\text{B.9})$$

Substituting this back into the Wigner distribution (equation (B.2)) we finally get:

$$W(p, R) = \frac{1}{\pi \hbar} e^{-\frac{(R-R_0)^2}{\mu^2}} e^{-\frac{(p - \hbar k_0)^2}{\hbar^2/\mu^2}} \quad (\text{B.10})$$

Taking the marginal integrals we get the position and velocity probability distributions:

$$|f(R)|^2 = \frac{2}{\mu \sqrt{\pi}} e^{-\frac{(R-R_0)^2}{\mu^2}} \quad (\text{B.11})$$

$$|f(p)|^2 = \frac{2}{\frac{\hbar}{\mu} \sqrt{\pi}} e^{-\frac{\mu^2}{\hbar^2}(p - \hbar k_0)^2} \quad (\text{B.12})$$

The above distributions are randomly sampled to get initial atomic velocities and positions for each simulation.

## Appendix C

# $\mathbf{R}_{lk,v}$ Alternatives

### C.1 $\mathbf{R}_{lk,v}$ Extrapolation

### C.2 Alternative Quantum Momentum Intercept

In Agostini, 16<sup>2</sup> another quantum momentum intercept term is discussed. This term is not used because, as previously discussed in section 1.4, it leads to unphysical transfer of population between adiabatic states when the nonadiabatic coupling elements are 0. However, it can be used in these Tully Models as an effective fix to the discontinuities caused by the  $\mathbf{R}_{lk,v}$  term.

The other quantum momentum intercept,  $\mathbf{R}_{0,v}^{(I)}$ , comes directly from the construction of the nuclear density using a linear combination of a product of gaussians (see equation (1.17) in the introduction). It is defined as in equation (C.1) below:

$$\mathbf{R}_{0,v}^{(I)} = \sum_{J}^{N_{tr}} \left[ \frac{\hbar \prod_{v'} g_{\sigma_{v'}^{(J)}(t)} \left( \mathbf{R}_{v'}^{(I)}(t) - \mathbf{R}_{v'}^{(J)}(t) \right)}{2 \sigma_v^{(J)}(t)^2 \sum_{K}^{N_{tr}} \prod_{v'} g_{\sigma_{v'}^{(K)}(t)} \left( \mathbf{R}_{v'}^{(I)}(t) - \mathbf{R}_{v'}^{(K)}(t) \right)} \mathbf{R}_v^{(I)} \right] \quad (\text{C.1})$$

However, as switching to this intercept directly may cause discontinuities in itself a smoothing parameter is applied to ease the switch. This is given in equation (C.2) below:

$$[1 - A(t)] R_{good}(t) + A(t) R_{bad}(t) = R_{effective}(t) \quad (\text{C.2})$$

$R_{good}$  refers to the intercept that should be switched to (e.g. for the detection of a spike in the  $R_{lk,v}^{(I)}$  we switch to the intercept in in equation (C.1)).  $R_{lk,v}^{(I)}$  refers to the intercept that is being switched from (e.g. when it is detected that the divergence of  $R_{lk,v}^{(I)}$  has finished then we switch from the alternative intercept back to  $R_{lk,v}^{(I)}$ ).  $A(t)$  is a smoothing parameter and is given in equation (C.3) below:

$$A(t) = \frac{D_v^{(I)}}{2} \left[ \tanh\left(t - \frac{t_{final} + t_{init}}{0.6Ndt}\right) + 1 \right] \quad (\text{C.3})$$

Where  $D_v^{(I)}$  is the distance between the 2 intercepts (e.g.  $D_v^{(I)} = R_{lk,v}^{(I)} - R_{0,v}^{(I)}$ ),  $N$  is the number of steps to take before settling solely on one intercept,  $t_{init}$  is the time of detection of the divergence,  $t_{final}$  is the time at which the code settles on 1 intercept and  $dt$  is the timestep taken.

A cartoon of this process is given in figure C.1

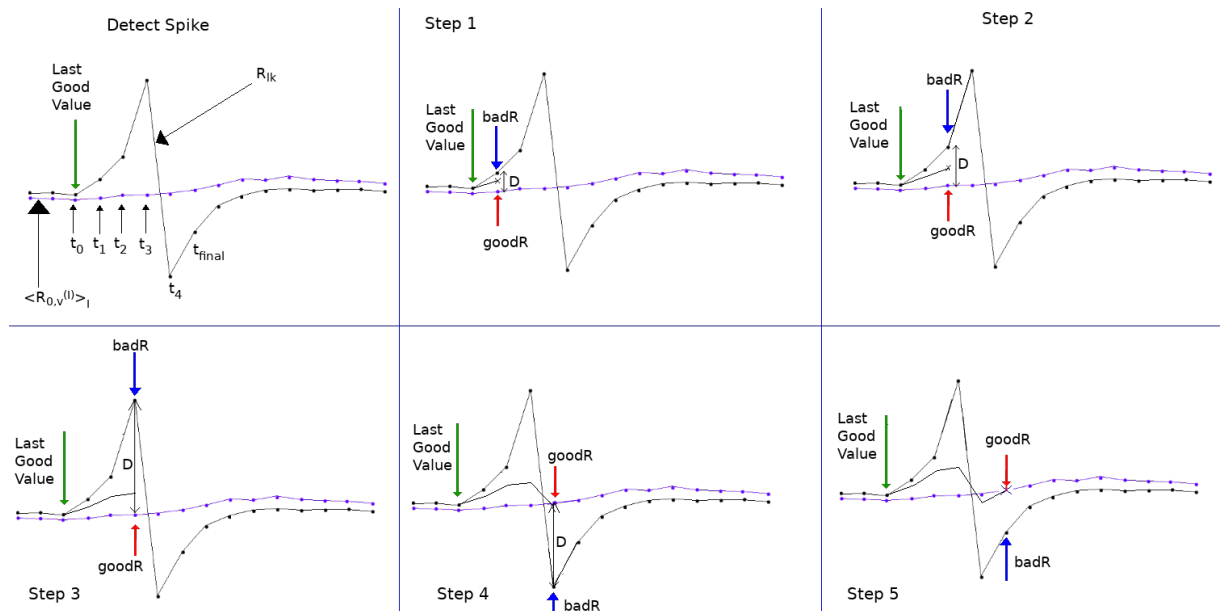


Figure C.1: A crude demonstration of the principle behind the smoothing procedure in switching between intercepts. The black line shows an intercept begin to diverge and the alternative intercept is shown in purple. As the step is incremented the amount of the alternative intercept that makes up the effective intercept is increased until only 1 intercept is used.

## Appendix D

# Rabi Oscillation

The time dependant Schrödinger equation is given below:

$$\hbar \frac{\delta}{\delta t} \Phi(\mathbf{R}(t), t) = \hat{H}(\mathbf{R}(t), t) \Phi(\mathbf{R}(t), t) \quad (\text{D.1})$$

If we hold the nuclear coordinates in place (e.g. remove time-dependence from nuclear coordinates) we get an ordinary differential equation as shown below:

$$\hbar \frac{d}{dt} \Phi(\mathbf{R}, t) = \hat{H}(\mathbf{R}, t) \Phi(\mathbf{R}, t) \quad (\text{D.2})$$

This has the following general solution. This can be solved with a Taylor series expansion.

$$\Phi(\mathbf{R}, t) = e^{\hbar \hat{H} t} \Phi(\mathbf{R}, 0)$$

Figure

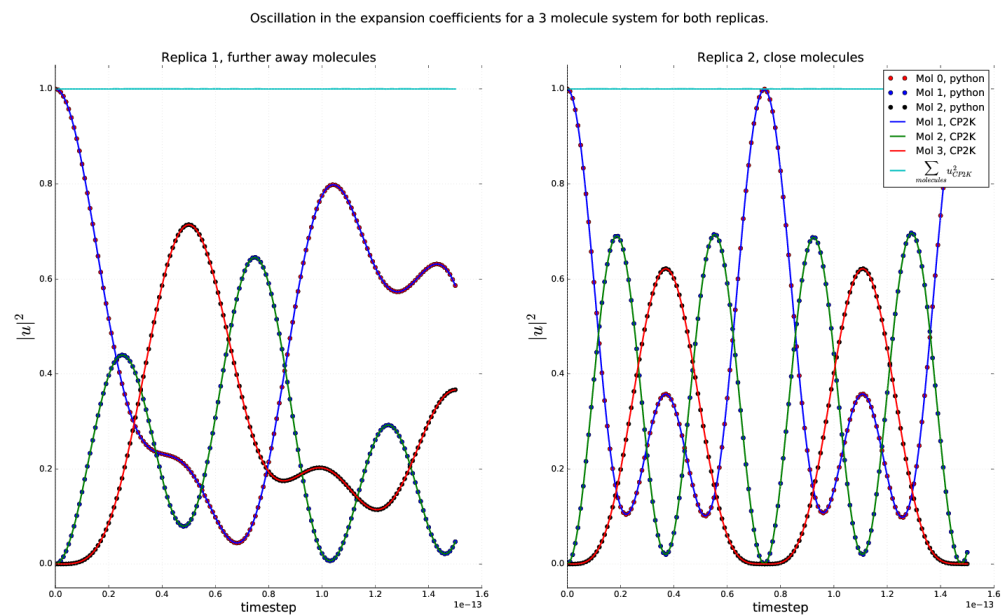


Figure D.1: Rabi oscillation occurring within a Ethylene trimer system. Dotted lines were calculated using equation (D.2), solid lines were calculated using the RK4 propagator within the CTMQC section of the CP2K code. The norm is shown on the top as a cyan line and the x axis shows the timestep in seconds.

## Appendix E

# Norm Conservation in CTMQC and Ehrenfest

A statement of the conservation of the norm, for a single trajectory, is given below in equation (E.1)

$$\frac{d}{dt} \sum_l |C_l(t)|^2 = \sum_l C_l^*(t) \frac{dC_l(t)}{dt} + \frac{dC_l^*(t)}{dt} C_l(t) = 2\mathbb{R} \left[ \sum_l C_l(t)^* \frac{dC_l(t)}{dt} \right] \quad (\text{E.1})$$

Substituting the equation for the evolution of the adiabatic coefficients (and removing the purely imaginary term) into (E.1) we get equation (E.3)

$$\frac{d}{dt} \sum_l |C_l(t)|^2 = 2 \sum_l \mathbb{R} \left[ \frac{-i}{\hbar} \cancel{\epsilon_{B\theta}^l} C_l(t)^* \cancel{C_l(t)} - \sum_k \left[ C_l(t)^* C_k(t) d_{lk}^{ad} - (A_l - B_l) C_l(t)^* C_l(t) \right] \right] \quad (\text{E.2})$$

$$= -2 \sum_l \mathbb{R} \left[ \sum_k \left[ C_l(t)^* C_k(t) d_{lk}^{ad} - (A_l - B_l) C_l(t)^* C_l(t) \right] \right] \quad (\text{E.3})$$

Where:

$$A_l = \sum_{v=1}^{N_n} \sum_k \frac{\mathcal{Q}_{lk,v}(t)}{\hbar M_v} \cdot \mathbf{f}_{k,v}(t) |C_k(t)|^2 \quad (\text{E.4})$$

$$B_l = \sum_{v=1}^{N_n} \sum_k \frac{\mathcal{Q}_{lk,v}(t)}{\hbar M_v} \cdot \mathbf{f}_{l,v}(t) |C_k(t)|^2 \quad (\text{E.5})$$

The NACE term evaluates to 0 due to the anti-symmetry of the NACE giving us equation (E.7).

So far, we have proved that the norm should be conserved here for all terms apart from the quantum momentum terms i.e. Ehrenfest.

$$\frac{d}{dt} \sum_l |C_l^{QM}(t)|^2 = 2 \sum_l \Re[(A_l - B_l) C_l(t)^* C_l(t)] \quad (\text{E.6})$$

$$= 2 \left[ \sum_l A_l |C_l(t)|^2 - \sum_l B_l |C_l(t)|^2 \right] \quad (\text{E.7})$$

However,  $\sum_l A_l |C_l|^2 \equiv \sum_l B_l |C_l|^2$ , therefore there is no change in the population and the norm should be conserved.

## Appendix F

# Dynamic $\sigma$ Calculation

The algorithm for dynamically updating the  $\sigma$  parameter outlined in Gossel, 18<sup>3</sup> is provided below.

1. Set an initial width parameter ( $\sigma_v^{(I)}(t - dt)$ ) and a constant we will name  $D$ .
2. Calculate a cutoff distance via:  $r_{cut}(t) = D\sigma_v^{(I)}(t - dt)$ .
3. For each atom index,  $v$ , and replica,  $I$ , gather replicas within a cutoff distance of the current replica. Set the number of replicas within the cutoff distance to  $N$ .
4. Calculate the distance between atoms on different replicas.
5. Find the standard deviation of these distances and set the width of the gaussian, centered on atom  $v$  and replica  $I$ , to this standard deviation.
6. If the standard deviation is smaller than  $\frac{D}{N} \min_I [\sigma_v^{(I)}(t - dt)]$  then set  $\sigma_v^{(I)}(t) = \frac{D}{N} \min_I [\sigma_v^{(I)}(t - dt)]$ .

## Appendix G

# Basis Transformation

We can expand the Schrödinger equation in terms of a diabatic basis,  $\phi$  rather than an adiabatic one,  $\psi$ . These 2 expansions are given in equations (G.1) and (G.2).

$$|\Psi\rangle = \sum_n C_n |\psi_n\rangle \quad (\text{G.1})$$

$$|\Psi\rangle = \sum_l u_l |\phi_l\rangle \quad (\text{G.2})$$

It follows from this we can define a transformation matrix,  $U_{ln}$  to transform between the adiabatic and diabatic bases. This is shown in equation (G.3) where the  $\overset{\leftrightarrow}{I}$  symbol represents the identity matrix. This identity only holds in the orthogonal diabatic basis  $\phi$  and wouldn't hold for non-orthogonal bases.

$$|\psi_n\rangle = \overset{\leftrightarrow}{I} |\psi_n\rangle = \sum_l |\phi_l\rangle \langle \phi_l| \psi_n\rangle = \sum_l |\phi_l\rangle U_{ln} \quad (\text{G.3})$$

A similar relation between expansion coefficients exists

$$\sum_n C_n |\psi_n\rangle = \sum_l u_l |\phi_l\rangle \quad (\text{G.4})$$

$$\sum_n C_n \langle \psi_m | \psi_n \rangle = \sum_l u_l \langle \psi_m | \phi_l \rangle \quad (\text{G.5})$$

$$C_m = \sum_l u_l U_{lm}^* \quad (\text{G.6})$$

Finally an important property of the transformation matrix is given in equation (G.7).

$$\sum_m U_{im} U_{lm}^* = \sum_m \langle \phi_i | \psi_m \rangle \langle \psi_m | \phi_l \rangle = \langle \phi_i | \phi_l \rangle = \delta_{il} \quad (\text{G.7})$$

Equations (G.3), (G.6) and (G.7) will be used below to transform the propagation equations from the adiabatic basis to the diabatic one.

## G.1 Forces

The equation for the propagation of the forces in the adiabatic basis is:

$$\begin{aligned} \mathbf{F}_v^{(I)} = & - \sum_n |C_n^{(I)}|^2 \nabla_v E_n^{(I)} - \sum_{n,m} C_m^{*(I)} C_n^{(I)} \left( E_n^{(I)} - E_m^{(I)} \right) \mathbf{d}_{v,mn}^{ad,(I)} \\ & - \sum_{m,n} |C_m^{(I)}|^2 \left( \sum_{v'}^{N_n} \frac{2}{\hbar M_{v'}} \mathcal{Q}_{v',mn}^{(I)} \cdot \mathbf{f}_{m,v'}^{(I)} \right) [\mathbf{f}_{n,v}^{(I)} - \mathbf{f}_{m,v}^{(I)}] |C_n^{(I)}|^2 \end{aligned} \quad (\text{G.8})$$

The quantum momentum part of the equation cannot be easily transformed so this will focus on the Ehrenfest part:

$$\mathbf{F}_{eh,v}^{(I)} = - \sum_n |C_n^{(I)}|^2 \nabla_v E_n^{(I)} - \sum_{n,m} C_m^{*(I)} C_n^{(I)} \left( E_n^{(I)} - E_m^{(I)} \right) \mathbf{d}_{v,mn}^{ad,(I)} \quad (\text{G.9})$$

Using equation (10) in Carof, 17<sup>91</sup> and the Hellman-Feynman theorem we can rewrite equation (G.9) as equation (G.10):

$$\mathbf{F}_{eh,v}^{(I)} = \sum_{m,n} C_m^{*(I)} C_n^{(I)} \langle \psi_m | \nabla_v H | \psi_n \rangle \quad (\text{G.10})$$

We can substitute the coefficients and basis functions for those in equations (G.3) and (G.6). This carried out in equation (G.15). However, I have removed the trajectory and

atom index from the terms to make the notation clearer.

$$F_{eh,v} = \sum_{m,n} C_m^* C_n \langle \psi_m | \nabla H | \psi_n \rangle \quad (\text{G.11})$$

$$= \sum_{m,n} \sum_i u_i^* U_{im} \sum_j u_j U_{jn}^* \sum_l U_{lm}^* \sum_k U_{kn} \langle \phi_l | \nabla H | \phi_k \rangle \quad (\text{G.12})$$

$$= \sum_{m,n} \sum_{i,j,k,l} u_i^* u_j U_{im} U_{lm}^* U_{jn}^* U_{kn} \langle \phi_l | \nabla H | \phi_k \rangle \quad (\text{G.13})$$

$$= \sum_{i,j,k,l} u_i^* u_j \delta_{il} \delta_{jk} \langle \phi_l | \nabla H | \phi_k \rangle \quad (\text{G.14})$$

$$= \sum_{i,j} u_i^* u_j \langle \phi_i | \nabla H | \phi_j \rangle \quad (\text{G.15})$$

However, in the code the expectation value of the gradient of the Hamiltonian ( $\langle \phi_i | \nabla H | \phi_j \rangle$ ) isn't very easily calculable. However, the gradient of the Hamiltonian matrix elements ( $\nabla \langle \phi_i | H | \phi_j \rangle$ ) is easily calculable via the overlap term,  $\nabla H = C \nabla S_{ij}$ . Therefore, using chain rule we can re-write equation (G.15) as:

$$F_{eh,v} = \sum_{i,j} u_i^* u_j \langle \phi_i | \nabla H | \phi_j \rangle \quad (\text{G.16})$$

$$= \sum_{i,j} u_i^* u_j (\nabla \langle \phi_i | H | \phi_j \rangle - \langle \nabla \phi_i | H | \phi_j \rangle - \langle \phi_i | H | \nabla \phi_j \rangle) \quad (\text{G.17})$$

$$= \sum_{i,j} u_i^* u_j \left( \nabla \langle \phi_i | H | \phi_j \rangle - \sum_l \langle \nabla \phi_i | \phi_l \rangle \langle \phi_l | H | \phi_j \rangle - \sum_l \langle \phi_i | H | \phi_l \rangle \langle \phi_l | \nabla \phi_j \rangle \right) \quad (\text{G.18})$$

$$= \sum_{i,j} u_i^* u_j \left( \nabla \langle \phi_i | H | \phi_j \rangle + \sum_l \mathbf{d}_{il} \langle \phi_l | H | \phi_j \rangle - \sum_l \mathbf{d}_{lj} \langle \phi_i | H | \phi_l \rangle \right) \quad (\text{G.19})$$

Giving the final equation for the transformed forces as:

$$\mathbf{F}_{eh,v}^{(I)} = \sum_{i,j} \mathbf{u}_i^{*(I)} \mathbf{u}_j^{(I)} \left( \nabla_v H_{ij}^{(I)} + \sum_l \mathbf{d}_{lk,v}^{(I)} H_{lj}^{(I)} - \sum_l \mathbf{d}_{lj,v}^{(I)} H_{il} \right) \quad (\text{G.20})$$

## Appendix H

# Adiabatic State Initialisation

By diagonalising the Hamiltonian we get the adiabatic energies (eigenvalues) for each state and transformation matrix (eigenvectors) to calculate diabatic states  $\mathbb{U}$ . We can calculate diabatic coefficients corresponding to each adiabatic state via equation (H.1) below.

$$\mathbb{U}\mathbf{C}_n = \mathbf{u}_n \quad (\text{H.1})$$

Where  $\mathbb{U}$  is the transformation matrix of size  $(N_{\text{mol}}, N_{\text{mol}})$ ,  $\mathbf{C}$  is a complex vector of size  $N_{\text{mol}}$  containing coefficients for adiabatic state  $n$  and  $\mathbf{u}$  is a complex vector of size  $N_{\text{mol}}$  containing coefficients for diabatic state  $n$ .

Seeing as we would like to find the diabatic population corresponding to each adiabatic state we localise coefficients on each pure adiabatic state and carry out the transformation e.g:  $C_i = (1+0i, 0+0i, 0+0i, \dots)$  when we want to find the diabatic coefficient corresponding to state 1 and  $C_i = (0+0i, 1+0i, 0+0i, \dots)$  when we want to find the diabatic coefficient corresponding to state 2 etc.. Therefore, the column,  $n$ , of the transformation matrix,  $\mathbb{U}$ , gives the diabatic coefficients corresponding to adiabatic state,  $n$ , as shown below in equation (H.2)

$$U_{in} = u_i \quad (\text{H.2})$$

Where  $n$  is the adiabatic state index and  $i$  is the diabatic (molecular) state index.

Once we have the diabatic state corresponding to each adiabatic state, and the en-

ergy of that adiabatic state, we can find which state best fulfills the requirements of being close to the center of the system and being within 3KT of the ground state. In order to do this, we can loop over each adiabatic state in increasing order of energy. The center of the system is calculated and the population weighted average center of mass,  $\mathbf{R}_n$  of the diabatic coefficients corresponding to adiabatic state n is calculated as in equation (H.3).

$$\mathbf{R}_n = \sum_i |u_i|^2 \mathbf{R}_{COM,i} \quad (\text{H.3})$$

The Euclidean distance between the center of the system and  $\mathbf{R}_{COM,i}$  is calculated and if this distance is below some threshold value then we initialise the surface hopping trajectory on that adiabatic state. If we do not find any states within 3KT of the ground state and within an acceptable radius of the center we start again this time increasing the maximum allowed distance from the center. If this maximum allowed distance is increased such that we reach another threshold distance the energy threshold is increased this time until a state is found that is close enough to the center. In this way we find an adiabatic state, which when transformed, gives a diabatic population close to center of the system and near the ground state energy.

## Appendix I

# Center of Mass Restraints

The surface hopping code at the time did not support electrostatic interactions. So, in order to maintain the structure from the molecular dynamics simulations, center of mass restraints were used on each molecule.

The restraint set up for 1 molecule is shown in figure I.1. Here each of the 4 coloured zig-zag shapes show which atoms are restrained. These atoms were restrained about their center of mass. This configuration of restraints was used in order to stop rotations about the long axis for each molecule as this would allow molecules to form a face-to-face stacking giving rise to unphysically high couplings. The restraint strength was chosen to be the same as in another group members study to allow for a fair comparison of results. A short MD equilibration was performed to determine whether the restraint spring constant was sufficient to hold the molecules in place well enough to prevent the very high couplings appearing in the global coupling distribution. To further validate the choice of restraint/general set up a surface hopping simulation was carried out on a layer of bulk crystal and the mobilities were compared to known values.

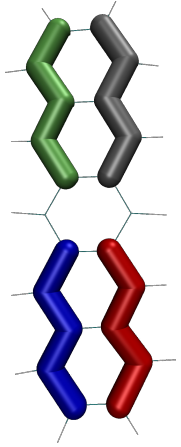


Figure I.1: The restraint set up for 1 molecule. Each coloured zig-zag shows the atoms that are restrained.

## Appendix J

# Active Systems

### J.1 0ns and 1ns Systems

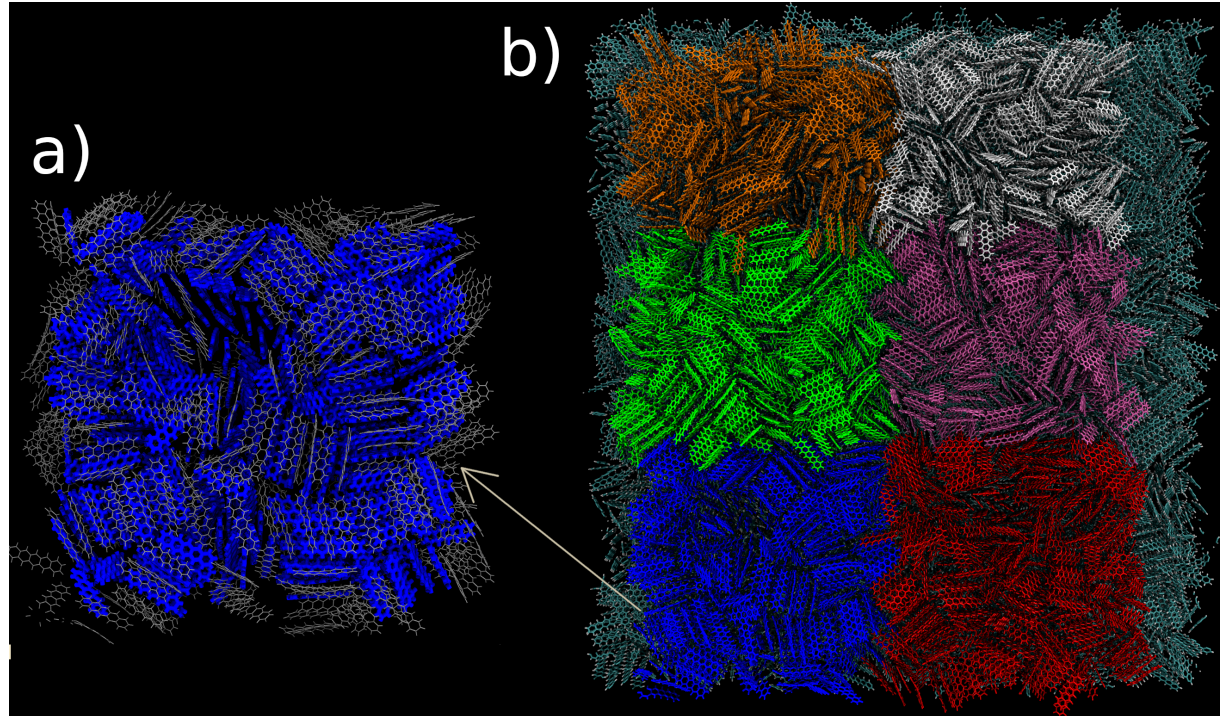


Figure J.1: Panel a) shows a system chosen to run surface hopping on, molecules in gray are fixed in place blue molecules show the active region. Panel b) shows every substructure chosen in the 0ns quenched structure.

The selection of the region for each surface hopping simulation was important in order to get a fair representation of the mobilities achievable within each structure. In the 0ns and 1ns quenched structures 6 slices were selected from the final snapshot of the structure. These were chosen to be independent clusters evenly spaced to sample

the mobility of the structure at various points. The selections are shown in figure J.1 for the 0ns quenched structure. The same process was used in the 1ns quenched structure.

In order to preserve the structure and maintain energy conservation a shell of inactive molecules was selected from the superstructure to surround the active region. The atoms within this remained fixed to their position at t=0.

## J.2 100ns System

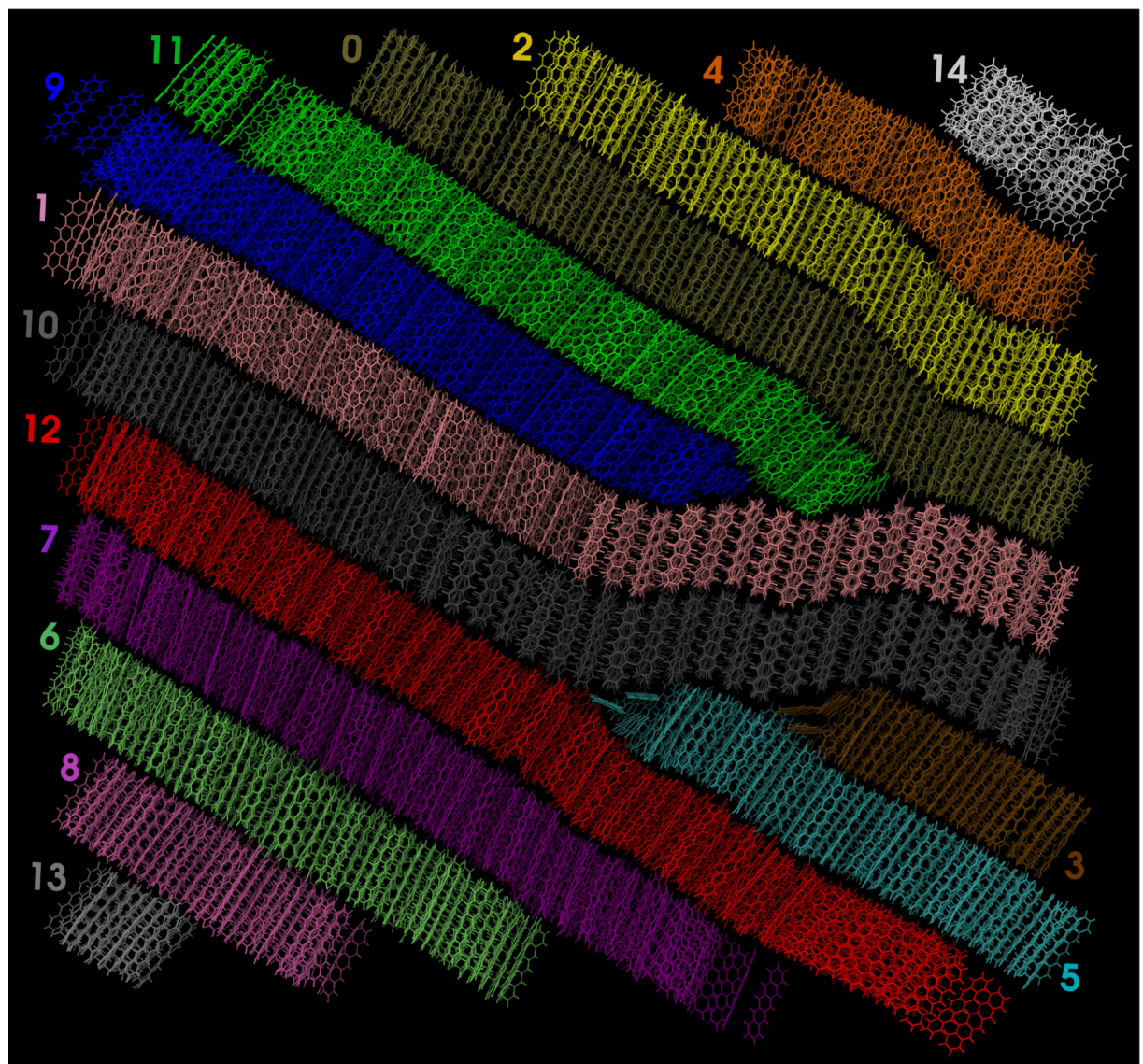


Figure J.2: The 100ns quenched structure clustered by layer. Each different colour represents a different cluster, labelled with the numbers around the edge of the structure.

The 100ns system is a much more ordered system and forms very well defined layers. This makes picking out structures on which to run surface hopping different to the 0/1ns quenched structures. The method I used was to first extend the superstructure in the z axis by  $\pm 45\text{\AA}$  by repeating the periodic image and discarding molecules more than  $\pm 45\text{\AA}$  from the simulation box boundaries. This was to ensure the resulting system was sufficiently large to converge mobilities. This added approximately 1 extra periodic image in the +ve and -ve z direction. A density based clustering algorithm (similar to DBSCAN<sup>119</sup>) was used to isolate the layers in the full structure by clustering centers of mass. These are shown in figure J.2. In this figure clusters 6, 7 and 11 were chosen to calculate the mobility via surface hopping.

### J.3 10ns System

The choice of region within the 10ns quenched structure was different from the 0/1ns and the 100ns quenched structure. Here we have some large crystal fragments forming but still very few well defined layers. In this system the mobility is expected to be much more dependant on the initial position of the charge carrier within the structure than in the 0ns and 100ns quenched structure where the structure was more uniformly disordered or ordered respectively. In order to sample a reasonable range of mobilities in this structure 4 clusters were selected shown in fig J.3. 3 of these (red, blue and purple) were selected using a similar clustering procedure as in the 100ns quenched structure. The center-right green cluster was selected as it looked like it was a fairly disordered region where multiple crystal fragments

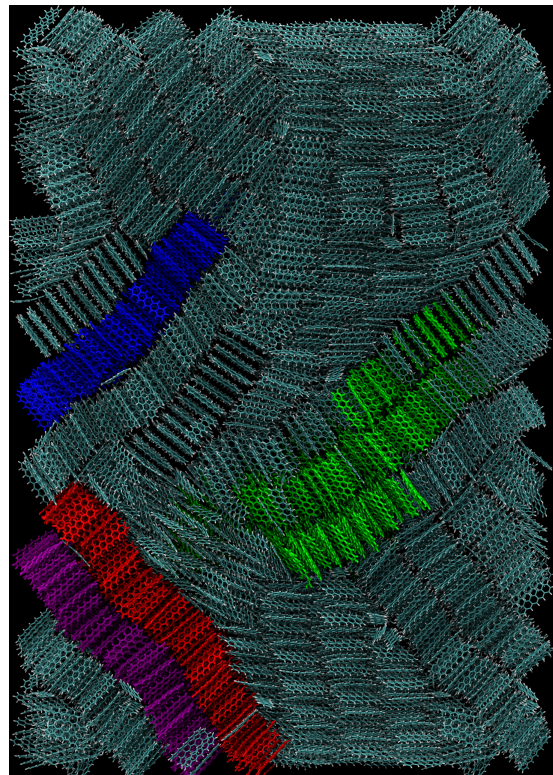


Figure J.3: The clusters chosen to run surface hopping simulations on. The coloured clusters each represent a different structure on which surface hopping was ran.

meet, which would give a lower bound on the mobility within the 10ns structure.

## Appendix K

# Additional Pentacene Mobility Information

Figure K.1: Experimental and computed charge mobilities for amorphous, polycrystalline and single-crystalline pentacene.

Author	device/comp.	structure	gate dielectric	mobility	comments
1, Hesse80 2,	Photocurrent	amorphous		0.001-0.01 0.4	long time mobility (1 $\mu$ s) short time mobility (20 ns)
3, Bae13	TFT	amorphous	polymer	0.04-0.14	dependent on deposition rate
4, Choo02	TFT	amorphous	SiN <sub>x</sub> /p-Si	0.3	
5		amorphous-crystalline		0.1	
6, this work	comp.	amorphous		0.2	bulk, 0% crystallinity
7, Knipp04 8	TFT	polycrystalline	SiN <sub>3</sub>	0.2-0.55	grain size 3-7 $\mu$ m
9, Fritz05 10	TFT	polycrystalline	thermal SiO <sub>2</sub> +OTS	0.5-1.4	grain size 1-2 $\mu$ m
11		polycrystalline	SiO <sub>2</sub> rough	0.02	
12, Duffy08	TFT	polycrystalline	SiO <sub>2</sub> smooth	0.31	
13, Klauk02 14	TFT	polycrystalline	SiO <sub>2</sub> +polymer	0.62	
15		polycrystalline	SiO <sub>2</sub> +BCB	0.4-0.7	large crystals
16, this work	comp.	nanocrystalline	SiO <sub>2</sub>	0.2	bulk, 30% crystallinity
17, this work	comp.	nanocrystalline	SiO <sub>2</sub> +OTS	0.9	bulk, 60% crystallinity
18, this work	comp.	nanocrystalline	Si+polymer	1.8	bulk, 80% crystallinity
19, Zhang16 20, this work	OFET	2D single crystal	boronitride	1.6 4.2	monolayer (1L) monolayer (1L)
21, Zhang16 22, this work	OFET	2D single crystal	boronitride	3	bilayer (2L)
23, Lee06 24,	OFET	single crystal	SiO <sub>2</sub>	7.3 2.3 0.66	bilayer (2L) largest, polymorph unknown smallest, polymorph unknown
25, Takeyama12	OFET	single crystal	Al <sub>2</sub> O <sub>3</sub> +ionic liquid	5	polymorph I, crystal size 200 $\mu$ m
26, Arabi16	OFET	single crystal	SiO <sub>2</sub>	5.6	crystal size 50 $\mu$ m
27, this work	comp.	single crystal		10.5	bulk, polymorph I

## Appendix L

# Addition-Subtraction Forces

### L.1 Real Space

The real space forces in the addition subtraction scheme are given in equation (L.1).

$$\mathbf{F}_i^\gamma = \begin{cases} \mathbf{F}_i^N(\mathbf{R}) + \sum_{j \in \gamma} (q_i^C q_j^C - q_i^N q_j^N) \mathbf{f}_{ij}(\mathbf{R}) + \sum_{j \notin \gamma} (q_i^C q_j^N - q_i^N q_j^N) \mathbf{f}_{ij}(\mathbf{R}); & i \in \gamma \\ \mathbf{F}_i^N(\mathbf{R}) - \sum_{j \in \gamma} (q_i^C q_j^N - q_i^N q_j^N) \mathbf{f}_{ij}(\mathbf{R}); & i \notin \gamma \end{cases} \quad (\text{L.1})$$

Where:

- $\mathbf{f}_{ij}(\mathbf{R}) = \frac{\hat{\mathbf{R}}_{ij}}{|\mathbf{R}_{ij}|} \left( \frac{\operatorname{erfc}(\alpha |\mathbf{R}_{ij}|)}{|rij|} + \frac{2\alpha}{\sqrt{\pi}} e^{-\alpha^2 |\mathbf{R}_{ij}|^2} \right)$ : the force between atoms i and j.
- $\mathbf{F}_i^N(\mathbf{R}) = q_i^N \sum_j^{N_{at}} q_j^N \mathbf{f}_{ij}(\mathbf{R})$ : the total neutral force.
- $q_j$  is the charge on atom j
- $\gamma$  is the index of the charged molecule.

Once again, we first calculate the total force between all neutral molecules. The charge-charge interactions are substituted in for the neutral-neutral interactions for atoms on the charged molecule. The charge-neutral interactions are then substituted in for the neutral-neutral interactions for the charged molecule and its environment. The bonded interaction corrections are the same as these.

## Appendix M

# Colophon

This document was set in the Times Roman typeface using L<sup>A</sup>T<sub>E</sub>X (specifically LuaTeX) and BibTeX+ make, composed with Vim.

# Bibliography

- [1] Federica Agostini, Ali Abedi, Yasumitsu Suzuki, Seung Kyu Min, Neepa T. Maitra, and E. K. U. Gross. The exact forces on classical nuclei in non-adiabatic charge transfer. *The Journal of Chemical Physics*, 142(8):084303, February 2015.
- [2] Federica Agostini, Seung Kyu Min, Ali Abedi, and E. K. U. Gross. Quantum-Classical Nonadiabatic Dynamics: Coupled- vs Independent-Trajectory Methods. *Journal of Chemical Theory and Computation*, 12(5):2127–2143, May 2016.
- [3] Graeme H. Gossel, Federica Agostini, and Neepa T. Maitra. Coupled-Trajectory Mixed Quantum-Classical Algorithm: A Deconstruction. *Journal of Chemical Theory and Computation*, August 2018.
- [4] William Humphrey, Andrew Dalke, and Klaus Schulten. VMD – Visual Molecular Dynamics. *Journal of Molecular Graphics*, 14:33–38, 1996.
- [5] John Stone. *An Efficient Library for Parallel Ray Tracing and Animation*. Master’s thesis, Computer Science Department, University of Missouri-Rolla, April 1998.
- [6] R. B. Campbell, J. M. Robertson, and J. Trotter. The crystal and molecular structure of pentacene. *Acta Crystallographica*, 14(7):705–711, Jul 1961.
- [7] R. Hesse and H. Bässler. Short-time carrier transport in amorphous pentacene. *physica status solidi (b)*, 101(2):481–487, 1980.
- [8] Jin-Hyuk Bae, Sin-Doo Lee, and Chang-Jae Yu. Deposition rate dependent mobility of an organic transistor with an anisotropic polymeric insulator. *Solid-State Electronics*, 79:98–103, 2013.

- [9] M. H. Choo, Jae Hoon Kim, and Seongil Im. Hole transport in amorphous-crystalline-mixed and amorphous pentacene thin-film transistors. *Applied Physics Letters*, 81(24):4640–4642, 2002.
- [10] D. Knipp and R.A. Street. Pentacene thin film transistors on large area compatible gate dielectrics. *Journal of Non-Crystalline Solids*, 338-340:595–598, 2004. Proceedings of the 20th International Conference on Amorphous and Microcrystalline Semiconductors.
- [11] Sandra E. Fritz, Tommie Wilson Kelley, and C. Daniel Frisbie. Effect of dielectric roughness on performance of pentacene tfts and restoration of performance with a polymeric smoothing layer. *The Journal of Physical Chemistry B*, 109(21):10574–10577, Jun 2005.
- [12] Claudia M. Duffy, Jens W. Andreasen, Dag W. Breiby, Martin M. Nielsen, Masahiko Ando, Takashi Minakata, and Henning Sirringhaus. High-mobility aligned pentacene films grown by zone-casting. *Chemistry of Materials*, 20(23):7252–7259, Dec 2008.
- [13] Hagen Klauk, Marcus Halik, Ute Zschieschang, Günter Schmid, Wolfgang Radlik, and Werner Weber. High-mobility polymer gate dielectric pentacene thin film transistors. *Journal of Applied Physics*, 92(9):5259–5263, 2002.
- [14] Yuhang Zhang, Jingsi Qiao, Si Gao, Fengrui Hu, Daowei He, Bing Wu, Ziyi Yang, Bingchen Xu, Yun Li, Yi Shi, Wei Ji, Peng Wang, Xiaoyong Wang, Min Xiao, Hangxun Xu, Jian-Bin Xu, and Xinran Wang. Probing carrier transport and structure-property relationship of highly ordered organic semiconductors at the two-dimensional limit. *Phys. Rev. Lett.*, 116:016602, Jan 2016.
- [15] J. Y. Lee, S. Roth, and Y. W. Park. Anisotropic field effect mobility in single crystal pentacene. *Applied Physics Letters*, 88(25):252106, 2006.
- [16] Yoko Takeyama, Shimpei Ono, and Yuji Matsumoto. Organic single crystal transistor characteristics of single-crystal phase pentacene grown by ionic liquid-assisted vacuum deposition. *Applied Physics Letters*, 101(8):083303, 2012.

- [17] S. Atika Arabi, Ji Dong, Misbah Mirza, Peng Yu, Liang Wang, Jun He, and Chao Jiang. Nanoseed assisted pvt growth of ultrathin 2d pentacene molecular crystal directly onto sio2 substrate. *Crystal Growth & Design*, 16(5):2624–2630, May 2016.
- [18] C. K. Chiang, C. R. Fincher, Y. W. Park, A. J. Heeger, H. Shirakawa, E. J. Louis, S. C. Gau, and Alan G. MacDiarmid. Electrical Conductivity in Doped Polyacetylene. *Physical Review Letters*, 39(17):1098–1101, October 1977.
- [19] Hideki Shirakawa, Edwin J. Louis, Alan G. MacDiarmid, Chwan K. Chiang, and Alan J. Heeger. Synthesis of electrically conducting organic polymers: halogen derivatives of polyacetylene,  $(CH)_x$ . *J. Chem. Soc., Chem. Commun.*, 0(16):578–580, Jan 1977.
- [20] Bernard Kippelen and Jean-Luc Brédas. Organic photovoltaics. *Energy Environ. Sci.*, 2(3):251–261, 2009.
- [21] M. J. Małachowski and J. Żmija. Organic field-effect transistors. *Opto-Electron. Rev.*, 18(2):121–136, Jun 2010.
- [22] N. Thejo Kalyani and S. J. Dhoble. Organic light emitting diodes: Energy saving lighting technology—A review. *Renewable Sustainable Energy Rev.*, 16(5):2696–2723, Jun 2012.
- [23] Sebastian Reineke, Frank Lindner, Gregor Schwartz, Nico Seidler, Karsten Walzer, Björn Lüssem, and Karl Leo. White organic light-emitting diodes with fluorescent tube efficiency. *Nature*, 459(7244):234, May 2009.
- [24] Kazuki Kato, Toshihiko Iwasaki, and Takatoshi Tsujimura. Over 130 lm/w all-phosphorescent white oleds for next-generation lighting. *Journal of Photopolymer Science and Technology*, 28:335–340, 10 2015.
- [25] Veaceslav Coropceanu, Jérôme Cornil, Demetrio A. da Silva Filho, Yoann Olivier, Robert Silbey, and Jean-Luc Brédas. Charge Transport in Organic Semiconductors. *Chemical Reviews*, 107(4):926–952, April 2007.

- [26] Samuele Giannini, Antoine Carof, Matthew Ellis, Hui Yang, Orestis George Ziogos, Soumya Ghosh, and Jochen Blumberger. Quantum localization and delocalization of charge carriers in organic semiconducting crystals. *Nature Communications*, 10(1):3843, Aug 2019.
- [27] Alessandro Troisi. Charge transport in high mobility molecular semiconductors: classical models and new theories. *Chem. Soc. Rev.*, 40:2347–2358, 2011.
- [28] Simone Fratini, Didier Mayou, and Sergio Ciuchi. The transient localization scenario for charge transport in crystalline organic materials. *Advanced Functional Materials*, 26(14):2292–2315, 2016.
- [29] I. Yavuz. Dichotomy between the band and hopping transport in organic crystals: insights from experiments. *Physical Chemistry Chemical Physics*, 19(38):25819–25828, 2017.
- [30] Tahereh Nemataram, Sergio Ciuchi, Xiaoyu Xie, Simone Fratini, and Alessandro Troisi. Practical computation of the charge mobility in molecular semiconductors using transient localization theory. *The Journal of Physical Chemistry C*, 123(12):6989–6997, Mar 2019.
- [31] S. Ciuchi, S. Fratini, and D. Mayou. Transient localization in crystalline organic semiconductors. *Phys. Rev. B*, 83:081202, Feb 2011.
- [32] Haobin Wang and Michael Thoss. A multilayer multiconfigurational time-dependent hartree study of vibrationally coupled electron transport using the scattering state representation. *The journal of physical chemistry. A*, 117, 03 2013.
- [33] Chr. Cattarius, G. A. Worth, H.-D. Meyer, and L. S. Cederbaum. All mode dynamics at the conical intersection of an octa-atomic molecule: Multi-configuration time-dependent Hartree (MCTDH) investigation on the butatriene cation. *The Journal of Chemical Physics*, 115(5):2088–2100, August 2001.
- [34] John C. Tully. Molecular dynamics with electronic transitions. *The Journal of Chemical Physics*, 93(2):1061–1071, 1990.

- [35] P. Ehrenfest. Bemerkung über die angenäherte Gültigkeit der klassischen Mechanik innerhalb der Quantenmechanik. *Zeitschrift für Physik*, 45(7):455–457, Jul 1927.
- [36] D. F. Coker and L. Xiao. Methods for molecular dynamics with nonadiabatic transitions. *J. Chem. Phys.*, 102(1):496–510, Jan 1995.
- [37] Guangjun Nan, Xiaodi Yang, Linjun Wang, Zhigang Shuai, and Yi Zhao. Nuclear tunneling effects of charge transport in rubrene, tetracene, and pentacene. *Phys. Rev. B*, 79:115203, Mar 2009.
- [38] Sharon Hammes-Schiffer. Theoretical Perspectives on Proton-Coupled Electron Transfer Reactions. *Acc. Chem. Res.*, 34(4):273–281, Apr 2001.
- [39] Sharon Hammes-Schiffer and John C. Tully. Proton transfer in solution: Molecular dynamics with quantum transitions. *J. Chem. Phys.*, 101(6):4657–4667, Sep 1994.
- [40] My Hang V. Huynh and Thomas J. Meyer. Proton-coupled electron transfer. *Chemical Reviews*, 107(11):5004–5064, Nov 2007.
- [41] John C. Tully. Nonadiabatic Dynamics. pages 34–71.
- [42] Simone Pisana, Michele Lazzeri, Cinzia Casiraghi, Kostya S. Novoselov, A. K. Geim, Andrea C. Ferrari, and Francesco Mauri. Breakdown of the adiabatic Born–Oppenheimer approximation in graphene. *Nat. Mater.*, 6(3):198, Feb 2007.
- [43] M. Born and R. Oppenheimer. Zur Quantentheorie der Moleküle. *Ann. Phys.*, 389(20):457–484, Jan 1927.
- [44] F Hund. *Z. Physik*, 40:742, 1927.
- [45] J Neumann and E Wigner. *Phys. Z.*, 30:467, 1929.
- [46] E Kemble and C Zener. *Phys. Rev.*, 33:536, 1929.
- [47] Clarence Zener and Ralph Howard Fowler. Non-adiabatic crossing of energy levels. *Proceedings of the Royal Society of London. Series A, Containing Papers of a Mathematical and Physical Character*, 137(833):696–702, 1932.

- [48] Xiaosong Li, John C. Tully, H. Bernhard Schlegel, and Michael J. Frisch. Ab initio Ehrenfest dynamics. *J. Chem. Phys.*, 123(8):084106, Aug 2005.
- [49] Kenichiro Saita and Dmitrii V. Shalashilin. On-the-fly ab initio molecular dynamics with multiconfigurational Ehrenfest method. *J. Chem. Phys.*, 137(22):22A506, Dec 2012.
- [50] Daniela Kohen, Frank H. Stillinger, and John C. Tully. Model studies of nonadiabatic dynamics. *J. Chem. Phys.*, 109(12):4713–4725, Sep 1998.
- [51] John C. Tully. Perspective: Nonadiabatic dynamics theory. *The Journal of Chemical Physics*, 137(22):22A301, December 2012.
- [52] Priya V. Parandekar and John C. Tully. Detailed Balance in Ehrenfest Mixed Quantum-Classical Dynamics. *Journal of Chemical Theory and Computation*, 2(2):229–235, March 2006.
- [53] Samuele Giannini, Antoine Carof, and Jochen Blumberger. Crossover from hopping to band-like charge transport in an organic semiconductor model: Atomistic nonadiabatic molecular dynamics simulation. *The Journal of Physical Chemistry Letters*, 9(11):3116–3123, Jun 2018.
- [54] Antoine Carof, Samuele Giannini, and Jochen Blumberger. Detailed balance, internal consistency, and energy conservation in fragment orbital-based surface hopping. *The Journal of Chemical Physics*, 147(21):214113, 2017.
- [55] Linjun Wang, Alexey Akimov, and Oleg V. Prezhdo. Recent progress in surface hopping: 2011–2015. *The Journal of Physical Chemistry Letters*, 7(11):2100–2112, Jun 2016.
- [56] Linjun Wang and Oleg V. Prezhdo. A simple solution to the trivial crossing problem in surface hopping. *The Journal of Physical Chemistry Letters*, 5(4):713–719, Feb 2014.

- [57] J. Spencer, F. Gajdos, and J. Blumberger. Fob-sh: Fragment orbital-based surface hopping for charge carrier transport in organic and biological molecules and materials. *The Journal of Chemical Physics*, 145(6):064102, 2016.
- [58] Fruzsina Gajdos, Siim Valner, Felix Hoffmann, Jacob Spencer, Marian Breuer, Adam Kubas, Michel Dupuis, and Jochen Blumberger. Ultrafast Estimation of Electronic Couplings for Electron Transfer between -Conjugated Organic Molecules. *Journal of Chemical Theory and Computation*, 10(10):4653–4660, October 2014.
- [59] Soumya Ghosh, Samuele Giannini, Kevin Lively, and Jochen Blumberger. Nonadiabatic dynamics with quantum nuclei: simulating charge transfer with ring polymer surface hopping. *Faraday Discuss.*, 221:501–525, 2020.
- [60] Antoine Carof, Samuele Giannini, and Jochen Blumberger. How to calculate charge mobility in molecular materials from surface hopping non-adiabatic molecular dynamics – beyond the hopping/band paradigm. *Phys. Chem. Chem. Phys.*, 21:26368–26386, 2019.
- [61] Orestis George Ziogos, Samuele Giannini, Matthew Ellis, and Jochen Blumberger. Identifying high-mobility tetracene derivatives using a non-adiabatic molecular dynamics approach. *J. Mater. Chem. C*, 8:1054–1064, 2020.
- [62] Samuele Giannini, Orestis George Ziogos, Antoine Carof, Matthew Ellis, and Jochen Blumberger. Flickering polarons extending over ten nanometres mediate charge transport in high-mobility organic crystals. *Advanced Theory and Simulations*, 3(9):2000093, 2020.
- [63] Jacob Spencer, Laura Scalfi, Antoine Carof, and Jochen Blumberger. Confronting surface hopping molecular dynamics with marcus theory for a molecular donor–acceptor system. *Faraday Discuss.*, 195:215–236, 2016.
- [64] Terah Nemataram and Alessandro Troisi. Modeling charge transport in high-mobility molecular semiconductors: Balancing electronic structure and quantum dynamics methods with the help of experiments. *The Journal of Chemical Physics*, 152(19):190902, 2020.

- [65] Antoine Carof, Samuele Giannini, and Jochen Blumberger. Detailed balance, internal consistency, and energy conservation in fragment orbital-based surface hopping. *The Journal of Chemical Physics*, 147(21):214113, 2017.
- [66] J. Spencer, F. Gajdos, and J. Blumberger. Fob-sh: Fragment orbital-based surface hopping for charge carrier transport in organic and biological molecules and materials. *The Journal of Chemical Physics*, 145(6):064102, 2016.
- [67] Samuele Giannini, Orestis George Ziogos, Antoine Carof, Matthew Ellis, and Jochen Blumberger. Flickering polarons extending over ten nanometres mediate charge transport in high-mobility organic crystals. *Advanced Theory and Simulations*, 3(9):2000093, 2020.
- [68] Ali Abedi, Neepa T. Maitra, and E. K. U. Gross. Exact Factorization of the Time-Dependent Electron-Nuclear Wave Function. *Physical Review Letters*, 105(12), September 2010.
- [69] Federica Agostini, Seung Kyu Min, and E. K. U. Gross. Semiclassical analysis of the electron-nuclear coupling in electronic non-adiabatic processes. *Annalen der Physik*, 527(9-10):546–555, October 2015.
- [70] Federica Agostini, Ali Abedi, Yasumitsu Suzuki, and E.K.U. Gross. Mixed quantum-classical dynamics on the exact time-dependent potential energy surface: a fresh look at non-adiabatic processes. *Molecular Physics*, 111(22-23):3625–3640, December 2013.
- [71] Ali Abedi, Federica Agostini, Yasumitsu Suzuki, and E. K. U. Gross. Dynamical Steps that Bridge Piecewise Adiabatic Shapes in the Exact Time-Dependent Potential Energy Surface. *Physical Review Letters*, 110(26), June 2013.
- [72] Seung Kyu Min, Ali Abedi, Kwang S. Kim, and E. K. U. Gross. Is the Molecular Berry Phase an Artifact of the Born-Oppenheimer Approximation? *Phys. Rev. Lett.*, 113(26):263004, Dec 2014.

- [73] Todd J. Martínez\*. Insights for Light-Driven Molecular Devices from Ab Initio Multiple Spawning Excited-State Dynamics of Organic and Biological Chromophores. *American Chemical Society*, Oct 2005.
- [74] Farnaz A. Shakib and Pengfei Huo. Ring Polymer Surface Hopping: Incorporating Nuclear Quantum Effects into Nonadiabatic Molecular Dynamics Simulations. *J. Phys. Chem. Lett.*, 8(13):3073–3080, Jul 2017.
- [75] Basile F. E. Curchod, Ivano Tavernelli, and Ursula Rothlisberger. Trajectory-based solution of the nonadiabatic quantum dynamics equations: an on-the-fly approach for molecular dynamics simulations. *PCCP*, 13(8):3231–3236, Feb 2011.
- [76] Ivano Tavernelli. Ab initio–driven trajectory-based nuclear quantum dynamics in phase space. *Phys. Rev. A*, 87(4):042501, Apr 2013.
- [77] Arne Scherrer, Federica Agostini, Daniel Sebastiani, E. K. U. Gross, and Rodolphe Vuilleumier. Nuclear velocity perturbation theory for vibrational circular dichroism: An approach based on the exact factorization of the electron-nuclear wave function. *J. Chem. Phys.*, 143(7):074106, Aug 2015.
- [78] Seung Kyu Min, Federica Agostini, Ivano Tavernelli, and E. K. U. Gross. Ab Initio Nonadiabatic Dynamics with Coupled Trajectories: A Rigorous Approach to Quantum (De)Coherence. *The Journal of Physical Chemistry Letters*, 8(13):3048–3055, July 2017.
- [79] John C. Tully. Molecular dynamics with electronic transitions. *The Journal of Chemical Physics*, 93(2):1061–1071, July 1990.
- [80] Thomas D. Kühne, Marcella Iannuzzi, Mauro Del Ben, Vladimir V. Rybkin, Patrick Seewald, Frederick Stein, Teodoro Laino, Rustam Z. Khalilullin, Ole Schütt, Florian Schiffmann, Dorothea Golze, Jan Wilhelm, Sergey Chulkov, Mohammad Hossein Bani-Hashemian, Valéry Weber, Urban Borštník, Mathieu Taillefumier, Alice Shoshana Jakobovits, Alfio Lazzaro, Hans Pabst, Tiziano Müller, Robert Schade, Manuel Guidon, Samuel Andermatt, Nico Holmberg, Gregory K. Schenster, Anna Hehn, Augustin Bussy, Fabian Belleflamme, Gloria Tabacchi, Andreas

- Glöß, Michael Lass, Iain Bethune, Christopher J. Mundy, Christian Plessl, Matt Watkins, Joost VandeVondele, Matthias Krack, and Jürg Hutter. Cp2k: An electronic structure and molecular dynamics software package - quickstep: Efficient and accurate electronic structure calculations. *The Journal of Chemical Physics*, 152(19):194103, 2020.
- [81] J. Spencer, F. Gajdos, and J. Blumberger. FOB-SH: Fragment orbital-based surface hopping for charge carrier transport in organic and biological molecules and materials. *The Journal of Chemical Physics*, 145(6):064102, August 2016.
- [82] Steven L. Fiedler and Jussi Eloranta. Nonadiabatic dynamics by mean-field and surface-hopping approaches: energy conservation considerations. *Molecular Physics*, 108(11):1471–1479, 2010.
- [83] Joseph E. Subotnik. Augmented ehrenfest dynamics yields a rate for surface hopping. *The Journal of Chemical Physics*, 132(13):134112, 2010.
- [84] K.E. Atkinson. *An Introduction to Numerical Analysis*. Wiley, 1989.
- [85] R.B. Leighton Richard P. Feynman. *The Feynman Lectures on Physics, Vol 3*. Addison-Wesley, 1998.
- [86] James Kirkpatrick. An approximate method for calculating transfer integrals based on the zindo hamiltonian. *International Journal of Quantum Chemistry*, 108(1):51–56, 2008.
- [87] Harald Oberhofer and Jochen Blumberger. Revisiting electronic couplings and incoherent hopping models for electron transport in crystalline c60 at ambient temperatures. *Phys. Chem. Chem. Phys.*, 14:13846–13852, 2012.
- [88] Alessandro Troisi and Giorgio Orlandi. Hole migration in dna: a theoretical analysis of the role of structural fluctuations. *The Journal of Physical Chemistry B*, 106(8):2093–2101, Feb 2002.

- [89] Adam Kubas, Felix Hoffmann, Alexander Heck, Harald Oberhofer, Marcus Elstner, and Jochen Blumberger. Electronic couplings for molecular charge transfer: Benchmarking cdft, fodft, and fodftb against high-level ab initio calculations. *The Journal of Chemical Physics*, 140(10):104105, 2014.
- [90] Adam Kubas, Fruzsina Gajdos, Alexander Heck, Harald Oberhofer, Marcus Elstner, and Jochen Blumberger. Electronic couplings for molecular charge transfer: benchmarking cdft, fodft and fodftb against high-level ab initio calculations. ii. *Phys. Chem. Chem. Phys.*, 17:14342–14354, 2015.
- [91] Antoine Carof, Samuele Giannini, and Jochen Blumberger. Detailed balance, internal consistency, and energy conservation in fragment orbital-based surface hopping. *The Journal of Chemical Physics*, 147(21):214113, December 2017.
- [92] Fruzsina Gajdos, Siim Valner, Felix Hoffmann, Jacob Spencer, Marian Breuer, Adam Kubas, Michel Dupuis, and Jochen Blumberger. Ultrafast estimation of electronic couplings for electron transfer between  $\pi$ -conjugated organic molecules. *Journal of Chemical Theory and Computation*, 10(10):4653–4660, Oct 2014.
- [93] T.P. Nguyen. Defect analysis in organic semiconductors. *Materials Science in Semiconductor Processing*, 9(1):198 – 203, 2006. 11th International Conference on Defects - Recognition Imaging and Physics in Semiconductors (DRIP-XI) Sept. 13-19 in Beijing.
- [94] Biswajit Ray, Aditya G. Baradwaj, Bryan W. Boudouris, and Muhammad A. Alam. Defect characterization in organic semiconductors by forward bias capacitance-voltage (fb-cv) analysis. *The Journal of Physical Chemistry C*, 118(31):17461–17466, Aug 2014.
- [95] W. S. Hu, Y. T. Tao, Y. J. Hsu, D. H. Wei, and Y. S. Wu. Molecular orientation of evaporated pentacene films on gold: alignment effect of self-assembled monolayer. *Langmuir*, 21(6):2260–2266, Mar 2005.
- [96] Tatsuo Hasegawa and Jun Takeya. Organic field-effect transistors using single crystals. *Science and Technology of Advanced Materials*, 10(2):024314, 2009.

- [97] John E. Anthony, James S. Brooks, David L. Eaton, and Sean R. Parkin. Functionalized pentacene: improved electronic properties from control of solid-state order. *Journal of the American Chemical Society*, 123(38):9482–9483, Sep 2001.
- [98] John E. Anthony, David L. Eaton, and Sean R. Parkin. A road map to stable, soluble, easily crystallized pentacene derivatives. *Organic Letters*, 4(1):15–18, Jan 2002.
- [99] A. D’Angelo, B. Edgar, A. P. Hurt, and M. D. Antonijević. Physico-chemical characterisation of three-component co-amorphous systems generated by a melt-quench method. *Journal of Thermal Analysis and Calorimetry*, 134(1):381–390, Oct 2018.
- [100] Wanderlã L. Scopel, Antônio J. R. da Silva, and A. Fazzio. Amorphous  $\text{hfo}_2$  and  $\text{hf}_{1-x}\text{si}_x\text{O}$  via a melt-and-quench scheme using ab initio molecular dynamics. *Phys. Rev. B*, 77:172101, May 2008.
- [101] Seth S. Berbano, Inseok Seo, Christian M. Bischoff, Katherine E. Schuller, and Steve W. Martin. Formation and structure of  $\text{na}_2\text{s}+\text{p}_2\text{s}_5$  amorphous materials prepared by melt-quenching and mechanical milling. *Journal of Non-Crystalline Solids*, 358(1):93 – 98, 2012.
- [102] Pranav Karmwar, Kirsten Graeser, Keith C. Gordon, Clare J. Strachan, and Thomas Rades. Investigation of properties and recrystallisation behaviour of amorphous indomethacin samples prepared by different methods. *International Journal of Pharmaceutics*, 417(1):94 – 100, 2011. Advanced characterization techniques.
- [103] Min-Jin Ko, Joel Plawsky, and Meyer Birnboim. Fabrication of  $\text{cds}/\text{ag}$  hybrid quantum dot composites using a melt/quench method. *Journal of Non-Crystalline Solids*, 203:211 – 216, 1996. Optical and Electrical Propertias of Glasses.
- [104] Steve Plimpton. Fast parallel algorithms for short-range molecular dynamics. *Journal of Computational Physics*, 117(1):1 – 19, 1995.
- [105] Steve Plimpton. Lammps software. <http://lammps.sandia.gov>, 1995. [Online; accessed 21-Jan-2021].

- [106] Steve Plimpton, Roy Pollock, and Mark Stevens. Particle-mesh ewald and rrespa for parallel molecular dynamics simulations. In In Proceedings of the Eighth SIAM Conference on Parallel Processing for Scientific Computing, 1997.
- [107] Christopher I. Bayly, Piotr Cieplak, Wendy Cornell, and Peter A. Kollman. A well-behaved electrostatic potential based method using charge restraints for deriving atomic charges: the resp model. The Journal of Physical Chemistry, 97(40):10269–10280, Oct 1993.
- [108] M. J. Frisch, G. W. Trucks, H. B. Schlegel, G. E. Scuseria, M. A. Robb, J. R. Cheeseman, G. Scalmani, V. Barone, G. A. Petersson, H. Nakatsuji, X. Li, M. Caricato, A. V. Marenich, J. Bloino, B. G. Janesko, R. Gomperts, B. Mennucci, H. P. Hratchian, J. V. Ortiz, A. F. Izmaylov, J. L. Sonnenberg, D. Williams-Young, F. Ding, F. Lipparini, F. Egidi, J. Goings, B. Peng, A. Petrone, T. Henderson, D. Ranasinghe, V. G. Zakrzewski, J. Gao, N. Rega, G. Zheng, W. Liang, M. Hada, M. Ehara, K. Toyota, R. Fukuda, J. Hasegawa, M. Ishida, T. Nakajima, Y. Honda, O. Kitao, H. Nakai, T. Vreven, K. Throssell, J. A. Montgomery, Jr., J. E. Peralta, F. Ogliaro, M. J. Bearpark, J. J. Heyd, E. N. Brothers, K. N. Kudin, V. N. Staroverov, T. A. Keith, R. Kobayashi, J. Normand, K. Raghavachari, A. P. Rendell, J. C. Burant, S. S. Iyengar, J. Tomasi, M. Cossi, J. M. Millam, M. Klene, C. Adamo, R. Cammi, J. W. Ochterski, R. L. Martin, K. Morokuma, O. Farkas, J. B. Foresman, and D. J. Fox. Gaussian~16 Revision C.01, 2016. Gaussian Inc. Wallingford CT.
- [109] Axel D Becke. Becke’s three parameter hybrid method using the lyp correlation functional. J. Chem. Phys, 98(492):5648–5652, 1993.
- [110] C Lee, W Yang, and RG Parr. Density-functional exchange-energy approximation with correct asymptotic behaviour. Phys. Rev. B, 37(2):785–789, 1988.
- [111] Junmei Wang, Romain M. Wolf, James W. Caldwell, Peter A. Kollman, and David A. Case. Development and testing of a general amber force field. Journal of Computational Chemistry, 25(9):1157–1174, 2004.

- [112] Makoto Yoneya, Masahiro Kawasaki, and Masahiko Ando. Molecular dynamics simulations of pentacene thin films: The effect of surface on polymorph selection. *J. Mater. Chem.*, 20:10397–10402, 2010.
- [113] Makoto Yoneya, Masahiro Kawasaki, and Masahiko Ando. Are pentacene monolayer and thin-film polymorphs really substrate-induced? a molecular dynamics simulation study. *The Journal of Physical Chemistry C*, 116(1):791–795, Jan 2012.
- [114] Makoto Yoneya. Simulation of crystallization of pentacene and its derivatives from solution. *The Journal of Physical Chemistry C*, Jan 2021.
- [115] Ryan A. Miller, Amanda Larson, and Karsten Pohl. Novel surface diffusion characteristics for a robust pentacene derivative on au(111) surfaces. *Chemical Physics Letters*, 678:28 – 34, 2017.
- [116] Dong Wang, Ling Tang, Mengqiu Long, and Zhigang Shuai. Anisotropic thermal transport in organic molecular crystals from nonequilibrium molecular dynamics simulations. *The Journal of Physical Chemistry C*, 115(13):5940–5946, Apr 2011.
- [117] Florian Steiner, Carl Poelking, Dorota Niedzialek, Denis Andrienko, and Jenny Nelson. Influence of orientation mismatch on charge transport across grain boundaries in tri-isopropylsilyl ethynyl (tips) pentacene thin films. *Phys. Chem. Chem. Phys.*, 19:10854–10862, 2017.
- [118] Ida Bagus Hendra Prastiawan, Jingxiang Xu, Yusuke Ootani, Yuji Higuchi, Nobuki Ozawa, Shingo Maruyama, Yuji Matsumoto, and Momoji Kubo. Molecular interactions between pentacene and imidazolium ionic liquids: A molecular dynamics study. *Chemistry Letters*, 47(9):1154–1157, 2018.
- [119] Martin Ester, Hans-Peter Kriegel, Jörg Sander, and Xiaowei Xu. A density-based algorithm for discovering clusters in large spatial databases with noise. pages 226–231. AAAI Press, 1996.
- [120] EPA DSSTox. Epa dsstox. <https://comptox.epa.gov/dashboard/DTXSID7059648>, 2021. [Online; accessed 25-Jan-2021].

- [121] Stefan Schiefer, Martin Huth, Alexander Dobrinevski, and Bert Nickel. Determination of the crystal structure of substrate-induced pentacene polymorphs in fiber structured thin films. *Journal of the American Chemical Society*, 129(34):10316–10317, Aug 2007.
- [122] M. Klues and G. Witte. Crystalline packing in pentacene-like organic semiconductors. *CrystEngComm*, 20:63–74, 2018.
- [123] Sean M. Ryno, Chad Risko, and Jean-Luc Brédas. Impact of molecular packing on electronic polarization in organic crystals: The case of pentacene vs tips-pentacene. *Journal of the American Chemical Society*, 136(17):6421–6427, Apr 2014.
- [124] Daniel Käfer, Mira El Helou, Christian Gemel, and Gregor Witte. Packing of planar organic molecules: Interplay of van der waals and electrostatic interaction. *Crystal Growth & Design*, 8(8):3053–3057, Aug 2008.
- [125] Thorsten Vehoff, Yeon Sook Chung, Karen Johnston, Alessandro Troisi, Do Y. Yoon, and Denis Andrienko. Charge transport in self-assembled semiconducting organic layers: Role of dynamic and static disorder. *The Journal of Physical Chemistry C*, 114(23):10592–10597, Jun 2010.
- [126] Wei-Qiao Deng and William A. Goddard. Predictions of hole mobilities in oligoacene organic semiconductors from quantum mechanical calculations. *The Journal of Physical Chemistry B*, 108(25):8614–8621, Jun 2004.
- [127] Joe J. Kwiatkowski, Jarvist M. Frost, and Jenny Nelson. The effect of morphology on electron field-effect mobility in disordered c<sub>60</sub> thin films. *Nano Letters*, 9(3):1085–1090, Mar 2009.
- [128] Stavros Athanasopoulos, James Kirkpatrick, Diego Martínez, Jarvist M. Frost, Clare M. Foden, Alison B. Walker, and Jenny Nelson. Predictive study of charge transport in disordered semiconducting polymers. *Nano Letters*, 7(6):1785–1788, Jun 2007.

- [129] Thorsten Vehoff, Björn Baumeier, Alessandro Troisi, and Denis Andrienko. Charge transport in organic crystals: Role of disorder and topological connectivity. *Journal of the American Chemical Society*, 132(33):11702–11708, Aug 2010.
- [130] Pascal Kordt and Denis Andrienko. Modeling of spatially correlated energetic disorder in organic semiconductors. *Journal of Chemical Theory and Computation*, 12(1):36–40, Jan 2016.
- [131] Yuan Zhang, Ling-Kun Meng, Jin Hu, Rui-Ke Zou, Chao Tang, Gong Li, Yan Ding, Hai-Tong Cai, Zhi-Yao Yang, and Wei Huang. Theoretical exploration of carrier dynamics in amorphous pyrene–fluorene derivative organic semiconductors. *ACS Omega*, 4(9):14124–14132, Aug 2019.
- [132] Orestis George Ziogos, Samuele Giannini, Matthew Ellis, and Jochen Blumberger. Identifying high-mobility tetracene derivatives using a non-adiabatic molecular dynamics approach. *J. Mater. Chem. C*, 8:1054–1064, 2020.
- [133] Nicolas G. Martinelli, Matteo Savini, Luca Muccioli, Yoann Olivier, Frédéric Castet, Claudio Zannoni, David Beljonne, and Jérôme Cornil. Modeling polymer dielectric/pentacene interfaces: On the role of electrostatic energy disorder on charge carrier mobility. *Advanced Functional Materials*, 19(20):3254–3261, 2009.
- [134] P. P. Ewald. Die berechnung optischer und elektrostatischer gitterpotentiale. *Annalen der Physik*, 369(3):253–287, 1921.
- [135] Abdulnour Y. Toukmaji and John A. Board. Ewald summation techniques in perspective: a survey. *Computer Physics Communications*, 95(2):73–92, 1996.
- [136] D. Wolf, P. Keblinski, S. R. Phillpot, and J. Eggebrecht. Exact method for the simulation of coulombic systems by spherically truncated, pairwise  $r-1$  summation. *The Journal of Chemical Physics*, 110(17):8254–8282, 1999.
- [137] Dirk Zahn, Bernd Schilling, and Stefan M. Kast. Enhancement of the wolf damped coulomb potential: static, dynamic, and dielectric properties of liquid water from

- molecular simulation. *The Journal of Physical Chemistry B*, 106(41):10725–10732, Oct 2002.
- [138] Christopher J. Fennell and J. Daniel Gezelter. Is the ewald summation still necessary? pairwise alternatives to the accepted standard for long-range electrostatics. *The Journal of Chemical Physics*, 124(23):234104, 2006.
- [139] Colin R. Groom, Ian J. Bruno, Matthew P. Lightfoot, and Suzanna C. Ward. The Cambridge Structural Database. *Acta Crystallographica Section B*, 72(2):171–179, Apr 2016.
- [140] Pavlo O. Dral, Mario Barbatti, and Walter Thiel. Nonadiabatic excited-state dynamics with machine learning. *The Journal of Physical Chemistry Letters*, 9(19):5660–5663, Oct 2018.
- [141] Zhigang Shuai, Hua Geng, Wei Xu, Yi Liao, and Jean-Marie André. From charge transport parameters to charge mobility in organic semiconductors through multiscale simulation. *Chem. Soc. Rev.*, 43:2662–2679, 2014.
- [142] Weiwei Xie, Daniel Holub, Tomáš Kubař, and Marcus Elstner. Performance of mixed quantum-classical approaches on modeling the crossover from hopping to bandlike charge transport in organic semiconductors. *Journal of Chemical Theory and Computation*, 16(4):2071–2084, Apr 2020.
- [143] Sebastian T. Hoffmann, Stavros Athanasopoulos, David Beljonne, Heinz Bässler, and Anna Köhler. How do triplets and charges move in disordered organic semiconductors? a monte carlo study comprising the equilibrium and nonequilibrium regime. *The Journal of Physical Chemistry C*, 116(31):16371–16383, Aug 2012.
- [144] Hua Geng, Qian Peng, Linjun Wang, Haijiao Li, Yi Liao, Zhiying Ma, and Zhigang Shuai. Toward quantitative prediction of charge mobility in organic semiconductors: Tunneling enabled hopping model. *Advanced Materials*, 24(26):3568–3572, 2012.
- [145] Nianduan Lu, Ling Li, Writam Banerjee, Pengxiao Sun, Nan Gao, and Ming Liu. Charge carrier hopping transport based on marcus theory and variable-range hop-

- ping theory in organic semiconductors. *Journal of Applied Physics*, 118(4):045701, 2015.
- [146] I. I. Fishchuk, A. Kadašchuk, S. T. Hoffmann, S. Athanasopoulos, J. Genoe, H. Bässler, and A. Köhler. Unified description for hopping transport in organic semiconductors including both energetic disorder and polaronic contributions. *Phys. Rev. B*, 88:125202, Sep 2013.
- [147] Zhigang Shuai, Weitang Li, Jiajun Ren, Yuqian Jiang, and Hua Geng. Applying marcus theory to describe the carrier transports in organic semiconductors: Limitations and beyond. *The Journal of Chemical Physics*, 153(8):080902, 2020.
- [148] Guangjun Nan, Linjun Wang, Xiaodi Yang, Zhigang Shuai, and Yi Zhao. Charge transfer rates in organic semiconductors beyond first-order perturbation: From weak to strong coupling regimes. *The Journal of Chemical Physics*, 130(2):024704, 2009.